A Computational Study of Compressor Inlet Boundary Conditions with Total Temperature Distortions

by

Kevin M. Eisemann

Thesis submitted to the Faculty of the
Virginia Polytechnic Institute and State University
in partial fulfillment of the requirements for the degree of

Master of Science
In
Mechanical Engineering

_____

Walter F. O'Brien
Committee Chairman

_____ _____

Douglas C. Rabe
Committee Member

Clinton L. Dancey
Committee Member

June 16, 2005
Blacksburg, VA

Keywords: Inlet Distortion, Total Temperature, Boundary Conditions, Thermal Source, Flow Injection, Jets, Gas Turbine Engines

A Computational Study of Compressor Inlet Boundary Conditions with Total Temperature Distortions

by

Kevin M. Eisemann
Committee Chairman: Walter F. O'Brien
Department of Mechanical Engineering

(Abstract)

A three-dimensional CFD program was used to predict the flow field that would enter a downstream fan or compressor rotor under the influence of an upstream thermal distortion. Two distortion generation techniques were implemented in the model; (1) a thermal source and (2) a heated flow injection method. Results from the investigation indicate that both total pressure and velocity boundary conditions at the compressor face are made non-uniform by the upstream thermal distortion, while static pressure remains nearly constant. Total pressure at the compressor face was found to vary on the order of 10%, while velocity varies from 50-65%. Therefore, in modeling such flows, neither of these latter two boundary conditions can be assumed constant under these conditions.

The computational model results for the two distortion generation techniques were compared to one another and evaluations of the physical practicality of the thermal distortion generation methods are presented. Both thermal distortion methods create total temperature distortion magnitudes at the compressor face that may affect rotor blade vibration. Both analyses show that holding static pressure constant is an appropriate boundary condition for flow modeling at the compressor inlet. The analyses indicate that in addition to the introduction of a thermal distortion, there is a potential to generate distortion in total pressure, Mach number, and velocity. Depending on the method of thermally distorting the inlet flow, the flow entering the compressor face may be significantly non-uniform.

The compressor face boundary condition results are compared to the assumptions of a previous analysis (Kenyon et al., 2004) in which a 25 R total temperature distortion was applied to a computational fluid dynamics (CFD) model of a fan geometry to obtain unsteady blade pressure loading. Results from the present CFD analyses predict similar total temperature distortion magnitudes corresponding to the total temperature variation used in the Kenyon analyses. However, the results indicate that the total pressure and circumferential velocity boundary conditions assumed uniform in the Kenyon analyses could vary by the order of 2% in total pressure and approximately 8% in velocity distortion. This supports the previously stated finding that assuming a uniform total pressure profile at the compressor inlet may be an appropriate approximation with the presence of a weak thermal distortion, while assuming a constant circumferential velocity boundary condition is likely not sufficiently accurate for any thermal distortion.

In this work, the referenced Kenyon investigation and others related to the investigation of distortion-induced aeromechanical effects in this compressor rotor have assumed no aerodynamic coupling between the duct flow and the rotor. A full computational model incorporating the interaction between the duct flow and the fan rotor would serve to alleviate the need for assuming boundary conditions at the compressor inlet.

Public Release Notice

This document has been deemed acceptable for public release by the United States Air Force. The associated case file number is AFRL/WS06-2688.

Acknowledgements

I would like to thank a number of individuals for assisting me during my graduate school tenure at Virginia Tech. First of all, I would like to thank my advisor and committee members. Dr. Walter O'Brien, thank you for allowing me to work under your tutelage. Your knowledge and dedicated interest in gas turbine engines inspire my growing kinship within the field. Dr. Douglas Rabe, thank you for allowing me to participate in the SCEP cooperative education program at Wright-Patterson AFB. I appreciate all the time and effort you put forth to assist me in my research. Dr. Clinton Dancey, thank you for generously joining my committee and reviewing my thesis. I would also like to thank Dr. Peter King and Dr. James Kenyon for assisting on earlier topics in my graduate research. To all of my professors and colleagues who have contributed to this work, thank you very much for all the knowledge and guidance you provided me.

Thank you, Cathy Hill, for your assistance in answering a barrage of questions from a confused graduate student. Your timeliness and knowledge was critical to my defending on time. Financial support from Battelle and the United States Air Force Research Laboratory is much appreciated. To Matt Madore and FLUENT: thank you for your generosity and wonderful CFD code.

To my Turbolab colleagues: Hoon, Matt, Darius, Mac, Cyril, Mano, Joe, Melissa, Gautham, Mike, Rob, Katie, and Rob Garcia. I had a wonderful time working in the lab with you. I wish you all the best in your education and future jobs. The fellowship will always be strong.

To my family: Mom, Dad, Brian, and my extended family. Thank you all so much for the love and support over the years that has molded me into the person I am today. I love you all.

To my friends: Suellen, Shelly, Curt, Omar, Louie, Nate and my other amigos and amigas. You made my experience at Virginia Tech such a memorable one. You are all dear to my heart and will be friends for a lifetime.

I would finally like to thank the Virginia Tech and Blacksburg, VA community. During my six years at Virginia Tech, I had a wonderful time. Thank you for making my stay at Virginia Tech such a memorable experience.

GO HOKIES!

Table of Contents

Abstract ... **ii**

Public Release Notice ... **iv**

Acknowledgements ... **v**

Table of Contents ... **vii**

List of Figures ... **ix**

List of Tables ... **x**

Nomenclature ... **xi**

1 Introduction ... **1**

1.1 General Nature of Inlet Distortions ... 1
1.2 Total Pressure and Total Temperature Distortions ... 2
1.3 Motivation for Research ... 6
1.4 Research Goals ... 7
1.5 Overview of Thesis ... 8

2 Literature Review ... **9**

2.1 Total Pressure Distortion ... 9
2.1.1 Performance and Operability ... 9
2.1.2 Aeromechanical Effects ... 10
2.2 Total Pressure Distortion due to Duct Curvature ... 16
2.3 Total Temperature Distortion ... 19
2.3.1 Performance and Operability ... 19
2.3.2 Aeromechanical Effects ... 25
2.4 Literature Review Summary ... 27

3 Analytical Method ... **29**

3.1 Preliminary Evaluation of Thermal Distortion Modeling ... 29
3.2 Modeling and Numerical Methods ... 31
3.2.1 Model Geometry Creation and Meshing ... 31
3.2.2 CFD Background ... 33
3.2.3 Application of Boundary Conditions ... 37
3.2.4 Meshing and CFD Summary ... 38
3.3 3-D CFD Thermal Source Distortion Investigation ... 39
3.4 3-D CFD Flow Injection Distortion Investigation ... 44
3.4.1 Flow Injector Design and Modeling ... 45
3.4.2 Straight Duct Investigation ... 45
3.4.3 Serpentine Duct Investigation ... 48

4 Results and Discussion 52
4.1 3-D CFD Thermal Source Distortion Investigation Results 52
4.2 3-D CFD Flow Injection Distortion Investigation Results 60
4.2.1 Straight Duct with Flow Injection 60
4.2.2 Serpentine Duct 67
4.3 AIP Distortion Comparison 80
4.4 Isentropic calculations 82
5 Conclusions 84
6 Recommendations 88
References 91
Appendix A: Tabulated Distortion Index Data 96
Appendix B: Additional Equations 97
Appendix C: FLUENT UDF 99
Vita 100

List of Figures

Figure 1-1: Design-related flow distortion 2
Figure 1-2: Total temperature distortion examples [ARD50015, 1991] 3
Figure 1-3: Compressor performance map adaptation [ARP1420, 1978] 4
Figure 2-1: Schematic of the CRF/ADLARF Test Rig 13
Figure 2-2: Example Campbell Diagram 14
Figure 2-3: 90^o bend vortex generation [adapted from Bullock, 1989] 17
Figure 2-4: Circumferential flow field measurements from a 180^o total temperature distortion [Braithwaite et al., 1979] 21
Figure 2-5: Compressor performance map of thermal distortion effects [SAE, 1991] 22
Figure 2-6: Uniform Total Temperature (a) and Constant Circumferential Axial Velocity (b) Boundary Condition used in Kenyon et al. (2004) 25
Figure 2-7: Comparison of Pressure Coefficient for (a) Po and (b) To Blade Loading [Kenyon, 2004] 26
Figure 3-1: Volume elements used to mesh geometries 31
Figure 3-2: Mean and Fluctuating Components for a Steady Analysis [adapted from Blazek, 2001] 34
Figure 3-3: 3/rev, 25 R total temperature distortion profile [Kenyon et al., 2004] 39
Figure 3-4: Meshed Cylindrical Duct Volume 41
Figure 3-5: Straight Duct w/ Flow injection 46
Figure 3-6: Initial (a) and Final (b) Serpentine Duct Geometry 48
Figure 3-7: Serpentine duct mesh 50
Figure 4-1: Exit total temperature (K) profile from the Thermal Source CFD analysis 52
Figure 4-2: Axial (a), 3-D-contour plot (b), exit contour plot (c) and thermal distortion inlet/exit contour plot (d) for static pressure (Pa, gauge) 54
Figure 4-3: Axial (a), 3-D-contour plot (b), exit contour plot (c) and thermal distortion inlet/exit contour plot (d) for Total Pressure (Pa, gauge) 55
Figure 4-4: Axial (a), 3-D-contour plot (b), exit contour plot (c) and thermal distortion inlet/exit contour plot (d) for Total Temperature (K) 56
Figure 4-5: Axial (a), 3-D-contour plot (b), exit contour plot (c) and thermal distortion inlet/exit contour plot (d) for Mach number 57
Figure 4-6: Axial (a), 3-D-contour plot (b), exit contour plot (c) and thermal distortion inlet/exit contour plot (d) for axial (z) velocity (m/s) 58
Figure 4-7: Total temperature (K) contours (straight duct, cold injection) 61
Figure 4-8: Total pressure (Pa) contours (straight duct, cold injection) 61
Figure 4-9: Static pressure (Pa) contours (straight duct, cold injection) 62
Figure 4-10: Mach number contours (straight duct, cold injection) 62
Figure 4-11: Velocity magnitude (m/s) contours (straight duct, cold injection) 63
Figure 4-12: Total temperature (K) contours (straight duct, hot injection) 64
Figure 4-13: Total pressure (Pa) contours (straight duct, hot injection) 64
Figure 4-14: Static pressure (Pa) contours (straight duct, hot injection) 65
Figure 4-15: Mach number contours (straight duct, hot injection) 65
Figure 4-16: Velocity magnitude (m/s) contours (straight duct, hot injection) 66

Figure 4-17: Total (Pa) and Static Pressure (Pa) Contour Plots for the (a) Short S-Duct and (b) Extended S-Duct 68
Figure 4-18: Total temperature (K) contours (serpentine duct, no injection) 70
Figure 4-19: Total Pressure (Pa) contours (serpentine duct, no injection) 71
Figure 4-20: Static Pressure (Pa) contours (serpentine duct, no injection) 71
Figure 4-21: Mach number contours (serpentine duct, no injection) 72
Figure 4-22: Velocity Magnitude (m/s) contours (serpentine duct, no injection) 72
Figure 4-23: Total temperature (K) contours (serpentine duct, cold injection) 73
Figure 4-24: Total pressure (Pa) contours (serpentine duct, cold injection) 73
Figure 4-25: Static pressure (Pa) contours (serpentine duct, cold injection) 74
Figure 4-26: Mach number contours (serpentine duct, cold injection) 75
Figure 4-27: Velocity magnitude (m/s) contours (serpentine duct, cold injection) 75
Figure 4-28: Total temperature (K) contours (serpentine duct, hot injection) 76
Figure 4-29: Total pressure (Pa) contours (serpentine duct, hot injection) 77
Figure 4-30: Static pressure (Pa) contours (serpentine duct, hot injection) 77
Figure 4-31: Mach number contours (serpentine duct, hot injection) 78
Figure 4-32: Velocity magnitude (m/s) contours (serpentine duct, hot injection) 79
Figure 4-33: Distortion Comparison at AIP 80

List of Tables

Table 3-1: Suitable FLUENT Boundary Conditions for Compressible Flow 38
Table 3-2: Boundary Conditions for Thermal Source CFD Analysis 42
Table 3-3: Flow Injector Parameters 45
Table 3-4: Straight Duct with Injection Boundary Conditions 48
Table 3-5: Serpentine Duct with Injection Boundary Conditions 51
Table 4-1: Isentropic calculations of Mach number and Velocity 83
Table A-1: CFD Distortion Results at the AIP 96

Nomenclature

Acronyms

1-D	One-Dimensional
3-D	Three-Dimensional
ADLARF	Augmented Damping Low-Aspect Ratio Fan
ARD	Aerospace Resource Document
AFC	Active Flow Control
CFD	Computational Fluid Dynamics
CRF	Compressor Research Facility (located at WPAFB)
HCF	High Cycle Fatigue
UCAV	Unmanned Air Combat Vehicle
V/STOL	Vertical/Short Take-off and Landing
WPAFB	Wright-Patterson Air Force Base

Variables

c_p	Constant pressure specific heat
Y_M	Dilation dissipation
$C_{1\varepsilon}$	Dimensionless constant
$C_{2\varepsilon}$	Dimensionless constant
$C_{3\varepsilon}$	Dimensionless constant
C_μ	Dimensionless constant
E	Energy
h	Enthalpy
R	Gas constant
g_i	Gravitational acceleration
S_h	Volumetric heat source (user defined)
M	Mach number
$\dot{m}$	Mass flow rate

p	Pressure
x_i	Spatial coordinate
P_o	Stagnation (or total) pressure
T_o	Stagnation (or total) temperature
T	Temperature
k	Thermal conductivity
k_{eff}	Thermal conductivity (effective)
t	Time
S_ε	Turbulence dissipation source
G_b	Turbulence generation due to buoyancy
K	Turbulent kinetic energy
G_K	Turbulent kinetic energy production
S_k	Turbulent kinetic energy source
M_t	Turbulent Mach number
Pr_t	Turbulent Prandtl number
q'''	Volumetric heat source

Mathematical Symbols

∂	Partial derivative

Greek Symbols

Δ	Change
β	Coefficient of thermal expansion
ρ	Density
ϕ_i	Flow variable (actual)
ϕ_i'	Flow variable (fluctuating)
$\bar{\phi}_i$	Flow variable (time-averaged)

δ_{ij}	Kronecker delta (3x3 identity matrix)
γ	Specific heat ratio
ε	Turbulence dissipation
σ_{ε}	Turbulent dissipation Prandtl number
σ_{K}	Turbulent kinetic energy Prandtl number
u_i	Velocity Component
μ	Viscosity (dynamic)
μ_t	Viscosity (turbulent)
μ_{eff}	Viscosity (effective)
τ_{ij}	Viscous stress tensor
$(\tau_{ij})_{eff}$	Viscous stress tensor (effective)

1 Introduction

1.1 General Nature of Inlet Distortions

The presence of non-uniform flow (or inlet distortion) is common for fan and compressor operation in gas turbine engines. To adequately define this topic, inlet distortion can be thought of as any spatial or temporal variation of flow variables entering the inlet duct and reaching the fan or compressor. The primary flow variables of interest are pressure, temperature, and velocity. Variation in flow properties can be assumed to change the operation and response of the engine and its components, for better, or predominantly, for worse.

Inlet distortion is a major area of concern for the design of military aircraft and aircraft engines. The ever-increasing performance needs, technological design, and severe operating conditions which aircraft engines experience in military applications result in an increased probability of inlet distortion interaction. New technologies, such as curved inlets, higher speed aircraft, and advanced design of rotor and stator blades add a larger scope of variables that the designer must consider. The designer must evaluate the performance and operability of the engine where efficiency, compressor pressure ratio, and flow stability may be affected by inlet distortion, as well as the aeromechanics or flow-induced blade vibration which may be associated with the distortion/rotor interaction. The introduction of distortions to the inlet of an engine can occur through numerous circumstances. This document will focus on two of the identified distortion types: (1) total pressure distortion and (2) total temperature distortion.

1.2 Total Pressure and Total Temperature Distortions

Total pressure distortions are caused by flow obstruction, separation, and a variety of other factors. Examples of flight or design-related situations where non-uniform total pressure can enter the engine are high Mach number maneuvering of aircraft, wake ingestion (Danforth, 1975), and physical flow blockages upstream of the fan or compressor such as struts. An example of design-related total pressure flow distortion is shown in Figure 1-1.

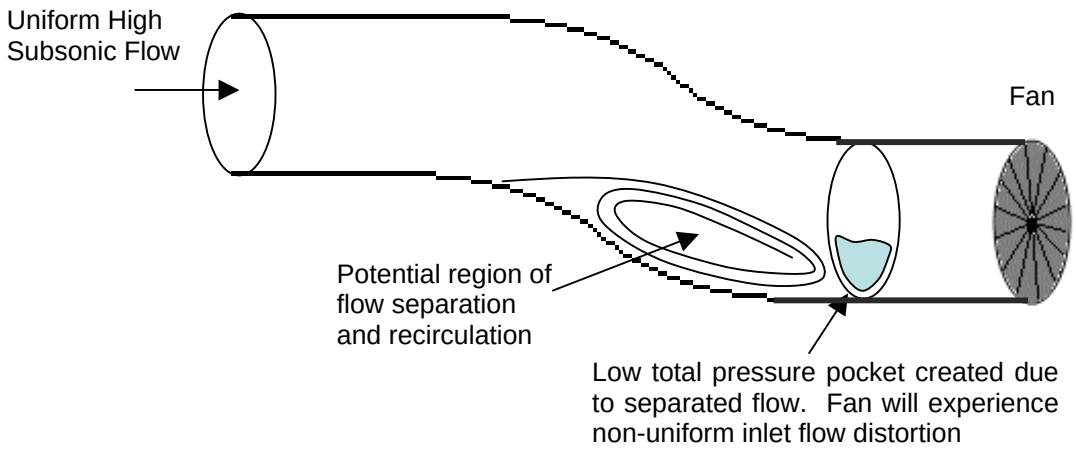

Figure 1-1: Design-related flow distortion

Some aircraft commonly experience design-related flow distortion. The F117 stealth fighter incorporates an advanced inlet design upstream of the gas turbine engine. This "s-duct" inlet prevents direct line of sight to the engine, reducing the chances of radar reflection from the rotor blades. This design, though providing a survivability benefit, causes a performance degradation of the aircraft engine, in that, a total strong pressure distortion is introduced from the aggressive turning of the flow (Hamed, 1997).

Total temperature distortions are a common occurrence in aircraft engine operation as well. Examples of this type of distortion can be seen in Figure 1-2, which displays a variety of thermal distortion situations (ARD50015, 1991). Military fighters

and helicopters are main applications of concern for temperature distortion influence. Hot gas ingestion from ordnance firing and thrust reversal, and reingestion from V/STOL applications and helicopter engine exhaust when in close ground proximity, are situations which can produce inlet temperature distortions. Also, catapult launches on aircraft carriers introduce steam ingestion to the inlet.

Flow injection in engines for active flow control can be another source of thermal distortion introduction. Flow injection at the tip upstream "tip-critical" sensitive rotors has been shown to increase the stability of the rotor (Suder et al., 2000). In an operational engine, this injected flow would be obtained by bleeding high pressure and consequently high temperature air from the compressor.

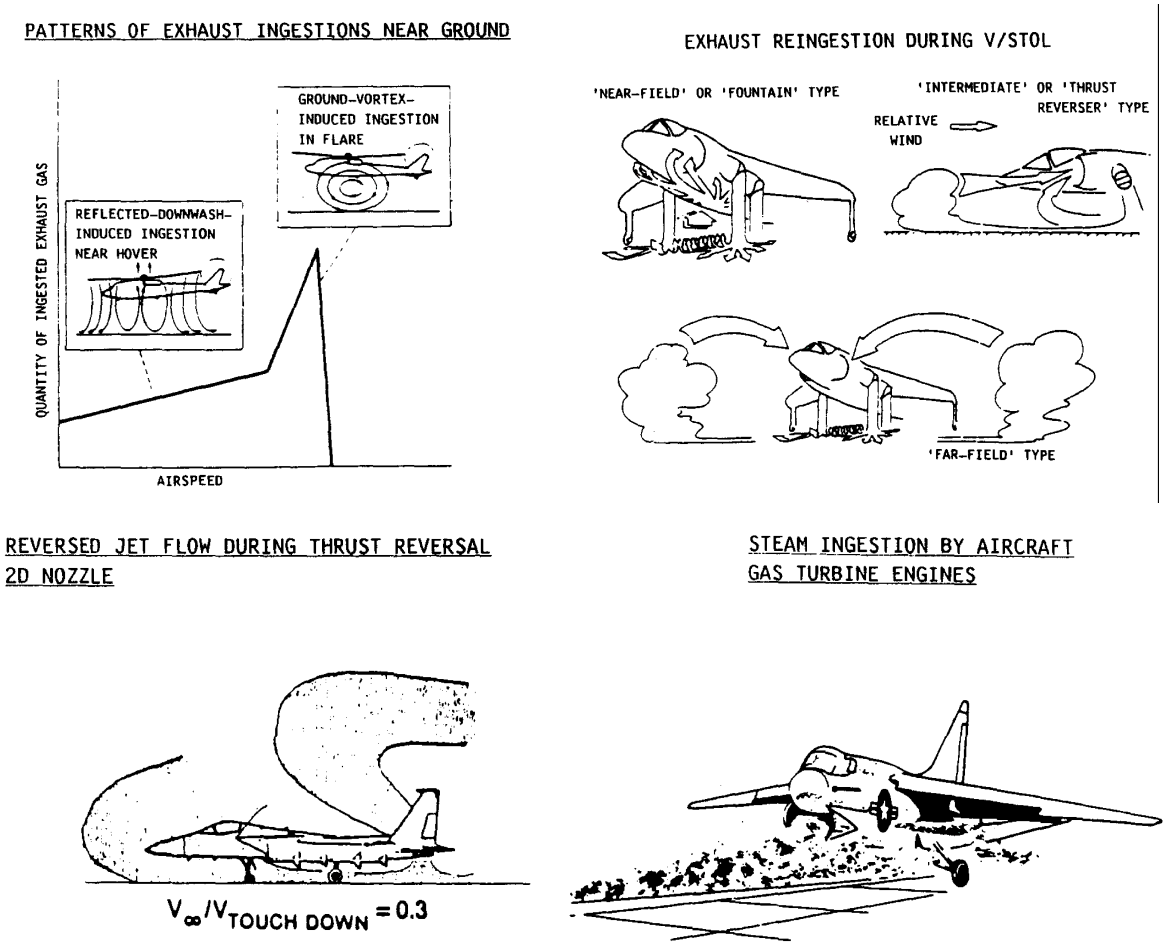

Figure 1-2: Total temperature distortion examples [ARD50015, 1991]

(Reprinted with permission from SAE ARD50015 © 1991 SAE International)

One can see from this short, yet diverse list of types of distortion, that aircraft engines commonly see distortion-related non-ideal operating conditions. The effects of these distortions can be of serious operational concern. From a thermodynamic performance standpoint, distortion, in general, has a negative effect on engine performance. Figure 1-3 shows a generic compressor performance map (pressure ratio vs. correct airflow) of a gas turbine engine. This plot displays the possible stable and unstable operating conditions for the compressor. By introducing a distortion to the inlet of the compressor, the aerodynamic stability limit drops, resulting in reduced margin between the operating line and the distorted stability limit. With lower stability margin, there is a higher potential for the development of flow instabilities such as rotating stall and surge. Rotating stall is a flow instability in which a flow blockage is created in the blade passages due to separated flow on the blade. This separation (or "stall") causes an adverse pressure gradient and tends to push the flow entering that section of the blade row into neighboring blade passages. This causes high angles of attack of the flow and subsequently develops a new stalled flow region in the adjacent blade passage. These stalled regions can involve several blade passages. Rotating stalls rotate at a relative speed with respect to the rotor blades in the opposite direction of the rotor rotation. Surge is a flow instability where planar waves oscillate the pressure and mass flow. Surge has the potential to cyclically reverse the flow in the engine, which reduces engine performance, and also can harm compressor blades due to severe pressure oscillations.

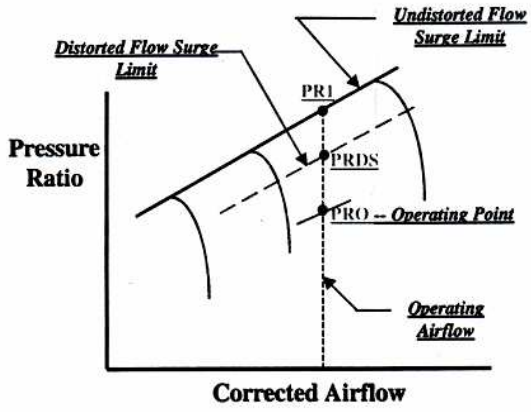

Figure 1-3: Compressor performance map adaptation [ARP1420, 1978]

(Reprinted with permission from SAE ARP1420 © 2002 SAE International)

On a longer time scale, the effects of inlet distortion can have an impact on engine component life. Specifically, the life of fan and compressor blades may be deteriorated if severe vibrations are induced by inlet distortion. Distortion patterns can induce high cyclic blade loading which can decrease the life of the blade. The accumulation of stress cycles can lead to structural degradation of the blades through High Cycle Fatigue (HCF) where a relatively high number of vibratory stress-cycles results in failure. Depending on the stress levels, HCF can occur in $10^6 - 10^7$ cycles. HCF can be induced by a variety of factors including steady-state inlet flow distortion, variations of inlet distortion such as gust excitation and oscillatory flows, blade instability (or flutter), rotor-stator mismatching, and numerous other mechanisms (Danforth, 1975).

The need to qualitatively understand how inlet distortions affect rotor blades and to quantitatively determine the applied forcing function on these blades is vital. Both experimental and computational means to evaluate the effects of inlet distortions have been investigated by academia, government, and industry, but new blade designs, engines, and operating characteristics necessitate a continuing need for accurate blade stress and life evaluation techniques under the influence of distortion. The knowledge of the effects of inlet distortions helps engine designers create products which are more reliable, have greater performance, have lower maintenance costs and provide a safer environment for the user.

1.3 Motivation for Research

Historically, inlet total pressure distortions have received the most attention as the primary driver for degraded engine performance and blade vibration. Total temperature distortions, however, have not been investigated as much, in part because of the lack of strict regulations and testing guidelines to follow (ARD50015, 1991). From the present literature search, there seems to be little information on the generation and effects of real-world thermal distortion in engine inlets.

There is a clear need to understand the effects of inlet thermal distortions on the engine's overall performance, component functionality, and lifespan. In testing rotors under the influence of a distortion, it is critical to develop means to experimentally and computationally model problems in the laboratory, which represent real world occurrences from these inlet flow perturbations. By utilizing computational models to simulate temperature distortion introduction to the inlet of an engine, the engine designer can have a better understanding of the resulting flow profiles entering the fan or compressor. Knowledge of these flow profiles can provide boundary condition information such that engine performance, functionality, and life can be better estimated.

1.4 Research Goals

This research aims to provide the gas turbine designer and engineer with a computational model of the effects of thermal distortions generated by two means on a flow field entering the compression system of an engine. The goal of this project is to determine compressor inlet boundary conditions at the aerodynamic interface plane (AIP) due to the upstream introduction of a thermal distortion. The AIP is a term coined from experimental distortion testing. It is a measurement rake (or plane) which captures flow variable information at a specified location immediately upstream of the compression system.

To attain the stated goal, preliminary steps were taken to direct the focus of the research. A literature review of inlet distortion research was conducted to identify existing thermal modeling methods, assess their applications, and review the results of the analyses. Computational analysis was implemented to model thermal distortions and to track the flow variables through the designed inlet ducts. A comparison of thermal distortion models, a discussion, and an evaluation of the results from the distortion analyses is presented. Conclusions are drawn from the selected analyses to provide the gas turbine engineer and inlet designer with additional knowledge of the effects of thermal distortion on a flow field, and resulting boundary conditions entering the compression system (AIP).

1.5 Overview of Thesis

The research presented in this thesis is an investigation into the determination of boundary conditions generated at the inlet to the compression system due to thermal distortion. Following the above brief introduction to distortions, a literature review of previous research is presented in Chapter 2. Topics including the performance and vibratory effects of distortions, inlet geometry, and computational and experimental research in the area of distortion are discussed. A summary at the end of the chapter identifies the research leading up to the work presented in this report. Chapter 3 presents the computational methods used to model the selected thermal distortions. Two high-fidelity CFD models were employed to capture the effects of the temperature distortion on the flow field. Chapter 4 reports the detailed results of these analyses. Flow profile data are presented for the two methods and discussion on each topic highlights some important findings in each case. Conclusions of the investigation are presented in Chapter 5. The analytical methods and results are evaluated in this section. Finally, a set of recommendations for the usage of this information is provided. The remainder of the document includes references cited, Appendices, and a Vita from the author.

2 Literature Review

To provide a better understanding of the previous research and effort put forth to investigate inlet distortions, a literature search was conducted. Material related to the experimental and computational analyses of the generation and effects of inlet distortions was obtained. The literature review yielded information regarding spatially-varying and time-varying total pressure and total temperature distortion investigations. The effects of these distortions on the engine are categorized in three main areas: performance, operability, and vibratory response. Performance effects can be thought of as the compressor change in operating performance due to the inlet distortion. Operability refers to the change in the operating point of the compressor as modified by the distortion. Possible resulting unstable phenomena, as highlighted in the previous chapter, can include stall, rotating stall, and surge of the engine. The vibratory response section refers to the vibratory effects on the compression system due to an inlet distortion.

2.1 Total Pressure Distortion

Total pressure distortions have been the primary distortion type investigated in engine testing. These distortions are commonly generated in testing by installing screens of varying porosity, struts, or other flow blockages upstream of a compression system. Jet flows have also been used to distort total pressure. Total pressure distortion due to flow blockage has the potential to degrade performance, reduce operability, and induce vibratory effects on rotor blades.

2.1.1 Performance and Operability

Inlet distortions have been shown to have a negative impact on compression system performance. Kimzey (1977) investigated the effect of increasing total pressure distortion in a 60^{o} sector upstream of a compressor. Increasing distortion levels tended to decrease the performance of the compressor by reducing the stability margin.

The Society of Automotive Engineers (SAE) developed a report entitled “Inlet Total-Pressure–Distortion Considerations for Gas Turbine Engines” in May of 1983. This document (AIR1419) produced a format for reporting total pressure distortion data, which was needed by government and industry for a consistent means of communication. Methods of generating total pressure distortion are documented along with necessary instrumentation needed to capture vital data during distortion testing.

As a result, substantial comparable experimental data has been obtained from total pressure distortion tests. Evaluation and assessment of stability, surge margin, and performance of a gas turbine engine has been standardized. Distortion screens have been generally used to create total pressure distortion and affect the performance of the compressor. The results of the analyses showed substantial degradation in engine performance and a lower stability limit of the engine due to the total pressure distortion.

2.1.2 Aeromechanical Effects

Danforth (1974) lists numerous mechanisms that need to be investigated to qualitatively (and ideally quantitatively) analyze blade vibrations. The drivers of these mechanisms are derived from non-uniform total pressure and velocity entering the inlet. Some of the identified mechanisms include blade instability (flutter), inlet gust excitation, upstream turbulence, and oscillatory inflows. Operating at blade resonance and having the blade experience one of the listed aerodynamic interactions has the potential to cause major vibratory response of the blade. The reference establishes a clear need to understand the effects of the drivers that cause detrimental performance and structural degradation of the blades. In addition, the author asks for a more viable distortion index to identify areas where vibration will be a serious concern. This index would ideally provide an early warning system for avoidance of blade failure.

An experimental analysis of the effects of inlet distortion on rotor blade unsteady aerodynamic response was performed by Manwaring and Fleeter (1990). Two means of distortion were used in two independent studies to serve as forcing functions to the rotor:

two 2/rev distortion screens 90 degrees apart, and wakes from two upstream airfoils. The compressor evaluated was an axial, 3 stage compressor with inlet guide vanes upstream of the first stage rotor. Steady and unsteady pressure measurements were captured by static pressure taps and high response pressure transducers on the 1st stage rotor at midspan on the pressure and suction side surfaces.

The 2/rev screen produced unsteady loading on the blades with a large 2nd engine order excitation and low amplitude higher harmonic content. The excitation by the wake resulted in no clear dominant 2/rev, and the majority of the measured harmonics were excited at frequencies greater than or equal to the magnitude to the 2nd engine order harmonic. Both distortions were representative of gas turbine engine inlet environments and showed the potential to cause severe blade vibrations. The research findings of this work support the importance of investigating total distortions generated by realistic drivers (or forcing functions), such as upstream distortion screens or struts, in engine inlets.

An investigation of unsteady blade loading on a 2-stage transonic low aspect ratio compressor was reported by Rabe, et al. (1995). The blade loading was generated by various distortion screens located upstream of the fan/compressor. Inlet total pressure distortions of 2, 3 and 8 per-rev were investigated at 4 known blade resonances. The total pressure distortion of the flow was measured upstream of fan by a series of total pressure probes installed at a planar measurement station. Blade surface pressures were measured at 85% span with high frequency pressure transducers at seven blade chord locations on the pressure side and suction side of two adjacent blades. Near the blade resonances, high amplitudes of blade response were measured. Transient force and moment calculations were obtained at the resonant test conditions. This experiment and analysis showed that unsteady pressures generated from inlet distortions can be successfully measured on rotor blades. One important finding from this analysis is that with increasing rotor speed, a larger variation in blade surface static pressure was found.

Hamed and Numbers (1997) reviewed inlet distortions and their potential to cause non-ideal inlet flow conditions to gas turbine engines. They observed that advancement in inlet design and the need to accommodate other technologies in various parts of the aircraft result in tradeoffs being made which might culminate in compressor performance loss. Non-uniform inflow can lead to performance and structural degradation (HCF). Sources of non-uniform inflow include swirl, turbulence, supersonic operation, and a variety of other factors. A summary of previous experimental and computational investigations of inlet distortion caused by the aforementioned factors on inlets and fan and compressor performance was highlighted in this paper. A review of the testing methodology was presented, and some questions were raised as to the legitimacy and accuracy of the techniques. The authors question whether the distortion generation techniques accurately represent real-world conditions. New test techniques for future testing are presented as possibilities to gain high fidelity results that are realistic to the operation of aircraft. The authors suggest that the inclusion of air jets, inlet swirl generators, turbulence generators, or a combination of distortion generation techniques could serve as realistic drivers for inlet distortion. According to the authors, creating distortion generators that accurately model inlet distortions may be a critical step in properly analyzing engine performance, operability, and blade vibrations.

Manwaring et al. (1997) presented an experimental and computational study of the effects of total pressure distortion on an advanced Augmented Damping Low-Aspect-Ratio Fan (ADLARF). Distortion screens of 3/rev and 8/rev were used in the experimental test stand to excite 3 blade resonant frequencies at various rotor speeds. Figure 2-1 shows a schematic cross-section of the 2-stage rotor and duct used in the experiment, where D is diameter.

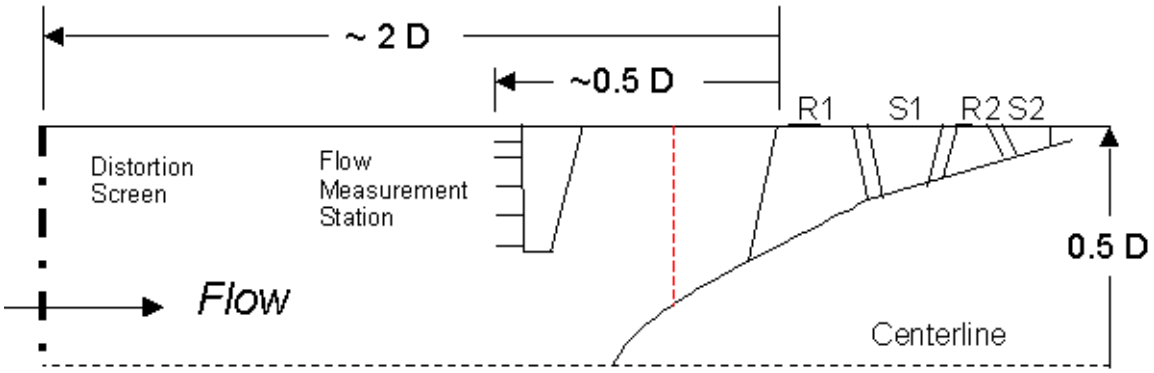

Figure 2-1: Schematic of the CRF/ADLARF Test Rig

In the experimental analysis, flow passed through distortion screens (circumferential, sinusoidal-varying porosity mesh) to create the total pressure distortion. The total pressure profile entering the rotor was obtained at a measurement station upstream of the rotor. Strain gauges were attached to the first stage rotor to obtain unsteady stress measurements. Static pressures on the blade surface (seven locations at 85% on the suction side and the pressure side of two adjacent blades) were obtained as well.

For the computational analysis, a finite element modal analysis was implemented to examine the blade frequencies and mode shapes. The knowledge of the individual mode frequency characteristics in a specified rotor speed range will provide an indication of what engine order (per rev) drivers may generate HCF-related blade vibrations. Manwaring et al (1997) found four specific modes of blade vibration that will drive a blade resonance in the speed range due to specific per-rev distortions. This information is visualized in a Campbell diagram in the paper.

A Campbell diagram (example shown in Figure 2-2) is a design tool used by structural analysts to evaluate operating frequencies where blade resonances occur that may result in excessive and damaging vibrations. The natural frequencies of the blade are plotted for the range of percent rotor speeds. The blade natural frequencies are commonly determined through finite element analysis (FEA). Engine-order or “per-rev” lines are also plotted on the Campbell diagram. Applied to distortions, these lines can be

thought of as the number of circumferential flow distortions that a rotor blade will encounter in one revolution. The intersection of the distortion or “per-rev” lines and blade mode lines is a resonant point. These operating conditions are regions where blade vibration has the potential to reach significant stress levels that contribute to HCF. Analytical Campbell diagrams provide an indication of drivers and modes that may couple to create high vibratory response, but alone do not provide an indication of true vibratory stress levels.

Along with the FEA, an unsteady quasi 3-D linearized Euler solver was used to obtain unsteady blade surface pressures. From these calculated blade loadings and the predicted mode shapes, the unsteady blade stresses were estimated.

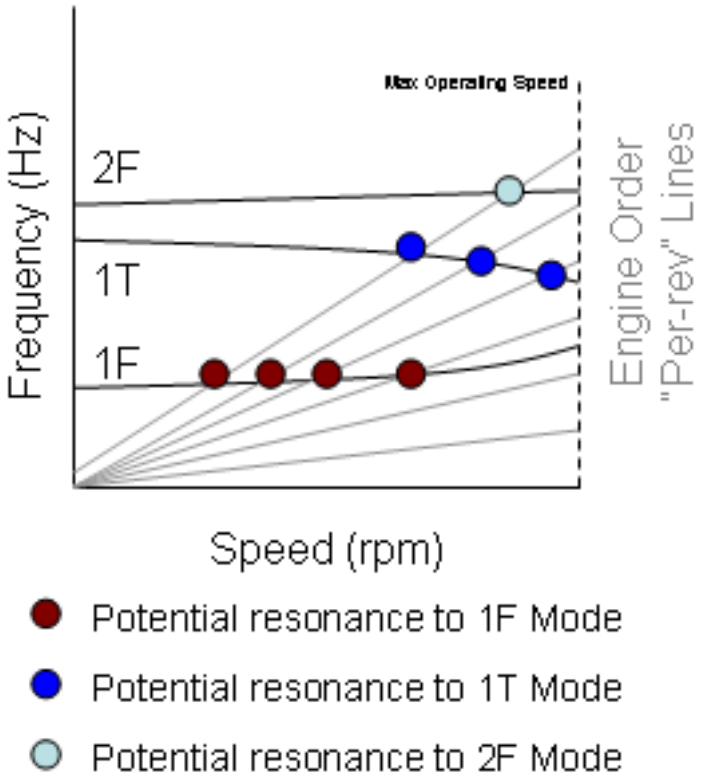

Figure 2-2: Example Campbell Diagram

Results from the 3/rev and 8/rev total pressure distortion experimental analyses showed high vibratory response occurred near the resonant crossings of the blade mode

lines and distortion lines. However, the computational results of blade loading at resonant conditions did not quantitatively compare well with the experimental results. This result infers that improvements to the computational flow code are needed to produce more accurate results to compare to measurements in future tests.

Kenyon et al. (1999) investigated the mistuning (blade-to-blade) resonant frequency variations and their relationship to aerodynamic loading. A 3/rev inlet total pressure distortion was applied as the aerodynamic input (forcing function) to a fan. The fan was operated from 8100-9100 rpm, where a known 1st bending mode would respond. Strain gauges were mounted on the blade to acquire stress measurements. Results from the analysis imply that individual blade response is strongly influenced by the mistuning of the blades and unsteady blade loading. A Finite Element Analysis (FEA) was employed as well to determine if the mistuning effects would result in high coupling of unsteady aerodynamics and blade mistuning. Experimental and computational results were comparable, inferring that aerodynamic coupling was strongly associated with the blade response. Therefore, aerodynamic coupling and blade mistuning are among of the variables which must be considered to computationally estimate blade stresses.

Wallace et al. (2003) computationally investigated the effects of a 3/rev inlet total pressure distortion on the same transonic fan used in Manwaring et al. (1997). The goal of the Wallace research was to couple unsteady blade loading from CFD with a FEA model to estimate blade loading. A CFD analysis on the 1st stage rotor was implemented to obtain the unsteady flow properties through the rotor blade passages. The inlet to the CFD model, or the AIP, was approximately 15 cm upstream of the first stage rotor (designated by the red dashed line in Figure 2-1). The inlet boundary condition to the CFD model was a 3/rev total pressure profile that was an analytical model approximation of the measured total pressure profile at the distortion measurement station. The total pressure measured in the flow varied nearly sinusoidally from 12.8 psia to 13.7 psia in a 3/rev pattern (approximately a 1 psia difference). The unsteady blade surface pressures were obtained from the CFD analysis. Wallace, et al. applied the unsteady blade loading

to a FEA model of a rotor blade to generate an approximate blade force due to a 3/rev total pressure distortion.

The computational results were compared to rig blade stress results to validate the computed blade forces. Unsteady blade loading was compared to test data and results were quite promising, where predicted stress levels were within 2.52% of measured stress data. A sensitivity study was investigated as well to understand the correlation between blade modal forces and distortion magnitude, for specified distortion intensities.

2.2 Total Pressure Distortion due to Duct Curvature

An article entitled "The Future of Stealth" (AW&ST, 2005) discusses the cost issue associated with stealth technologies on UCAVs (Unmanned Combat Air Vehicles). Stealth technology adds extra expenses to the aircraft in exchange for a survivability benefit, which is important for the aircraft's operation in a hostile environment. Stealth technologies, such as coatings and s-duct inlets, provide important aspects of defense to the vehicle.

Curved ducts are becoming more commonplace in today's military aircraft. The s-duct design adds a survivability benefit to the aircraft, yet may degrade the engine operation in the areas of performance, operability, and vibratory response. The need for curved inlets will support a growing effort to develop means to attenuate the distortions produced by these inlet geometries. It is advantageous in military applications to keep these inlets short with enough offset to completely hide the engine fan face, consequently increasing the associated flow distortion. Flow passing through a curved passage has a potential to separate, causing a total pressure distortion. For high speed flows, total pressure distortions due to curvature are quite severe. Lower speed flows do not suffer the same degree of total pressure loss as for the higher speed cases. All flows in curved ducts are affected by vortices that are created by turning the flow. Figure 2-3 shows an illustration of vortex generation in a 90^{o} bend.

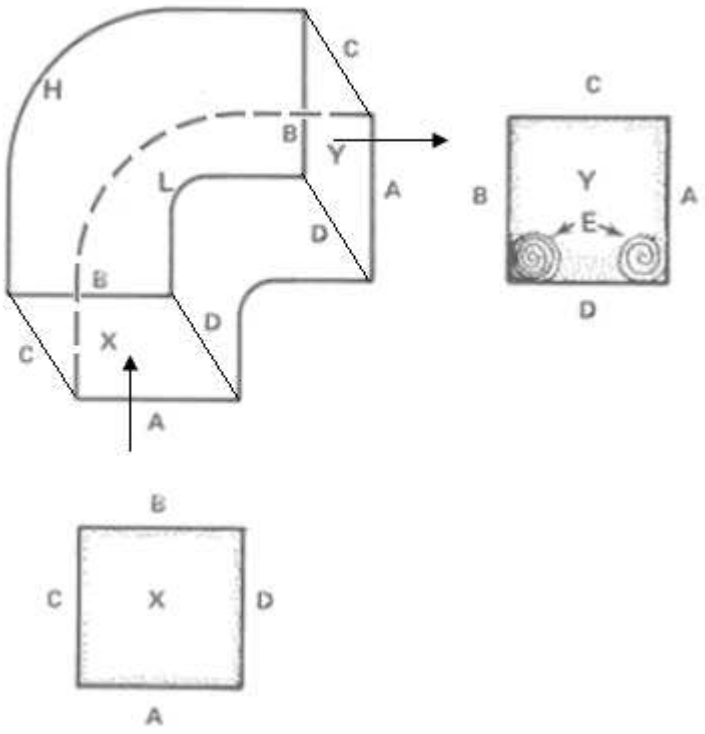

Figure 2-3: 90^{o} bend vortex generation [adapted from Bullock, 1989]

(Reprinted by permission of the American Institute of Aeronautics and Astronautics, Inc.)

Flow enters plane X and exits through plane Y. The letters A, B, C, and D refer to the walls of the duct. Two counter-rotating vortices are created in the short radius bend (L). The velocity profile exiting the bend will clearly be distorted by this secondary flow phenomenon, which is induced by a low pressure region due to separation on the short radius side of the duct.

Stanitz et al. (1953) investigated duct flow in a 90^{o} bend and showed that vortices are generated on the suction side (L) of the duct in the bend. These vortices have an undesirable effect in that energy is lost in this region of the flow through viscous dissipation.

One could imagine that if two of these 90^{o} ducts were placed adjacent to one another in opposite turning direction, vortices would form at the top and bottom of the duct. This occurs naturally in aircraft with serpentine (s-duct) inlets such as the F117 stealth fighter aircraft and the Boeing 727 commercial aircraft.

Another example of a curved inlet is found on the Boeing 727 aircraft. This aircraft has an aft engine mounted in the tail of the aircraft. The inlet to the engine is a serpentine design that has two approximately 45^{o} turns in the duct. Though not as severe as a 90-degree bend, similar adverse effects are present in operation, namely vortex generation and total pressure loss. Methods to reduce the magnitude of these effects are to lengthen the inlet, reduce turning, or to implement active flow control (AFC).

A visualization of these naturally occurring losses is depicted in Figure 1-1. Distortion patterns are developed due to the turning, which causes a total pressure distortion and a turbulent region of non-uniform velocity.

A recent advancement in inlet distortion control uses high pressure and temperature air from the compressor to reduce total pressure distortions entering the fan inlet. Active flow control uses this “bleed air” from the compressor to energize the distorted flow in a designated orientation. However, this high temperature compressed air will introduce a thermal distortion which could have negative impacts on the engine.

2.3 Total Temperature Distortion

Research regarding the effects of thermal distortions on turbine engines has mainly been focused on performance and operability concerns of the engine. There is a lack of research investigating the rotor vibratory response and HCF due to thermal distortion. The papers reviewed in the following sections reveal information about the performance issues, boundary conditions upstream of the compression system, and aeromechanical- response due to thermal distortion.

2.3.1 Performance and Operability

Rudey et al. (1970) investigated the effects of inlet temperature distortion on turbofan performance. The temperature distortion generator was a four-sector hydrogen burner placed upstream of the fan at the engine inlet bellmouth. Fuel lines were fed to five circumferential and two radial pipes with holes drilled to create various distortion patterns. The temperature distortion was produced by activating the burners in a specific quadrant of the flow path to ignite the fuel flow pattern. The distortion intensity and pattern was varied by increasing the fuel flow to the burners. The inlet and engine was heavily instrumented to measure fan inlet flow variables. Upstream of the fan, total pressure and total temperature were measured with radial emersion rakes. These variables were also measured at the fan discharge, compressor inlet and compressor exit to observe the propagation of the distorted flow. Results from the analysis indicate that introducing a spatial total temperature distortion has a negative effect on engine operability. Stall margin is reduced both by circumferential and radial thermal distortion patterns. The effect of ramping a thermal distortion (time-dependent distortion) is to affect operability by reducing the stall margin. A small drop in total pressure due to the total temperature distortion is also evident.

In a similar analysis, Braithwaite et al. (1973) investigated the effect of 180^o total pressure distortion, 180^o total temperature distortion, and combined total pressure and total temperature distortion on performance and operability of a J85-GE-13 turbojet

engine. A rake of total temperature, total pressure, and static pressure probes measured the flow variables immediately upstream of the engine. The experimental results reveal that under the influence of a thermal distortion, the total pressure and static pressure were nearly constant at the inlet. In addition, this research indicates that spatial thermal distortions can cause a loss of stall margin in the compressor.

The combined total pressure and total temperature distortion experiments indicate that overlapping the circumferential extent of the two distortions results in a further attenuation of the stability limit. In other words, if total pressure and total temperature distortion are more nearly in phase, there is an increased detrimental effect on the operability of the compressor. There was no information regarding the vibratory effects of there distortions presented in this research.

Walter and Shaw (1979) investigated the effects of circumferential total pressure and total temperature distortion patterns on compression system response. Total pressure (P_o), total temperature (T_o), and combined P_o and T_o distortions were applied to an analytical model which utilized parallel compressor theory to evaluate compressor performance behavior under an applied distortion pattern. Various circumferential extents were investigated to evaluate the robustness of the code. The computational results were compared to actual rig test data and results indicate that the analytical model developed accurately predicts engine performance parameters. Such models are helpful in the design and evaluation of future designs to predict stability assessment. The experimental and computational analyses indicated that all distortion cases investigated tended to lower the stability line, hence limiting the operability of the engine.

Braithwaite and Soeder (1979) examined combined pressure and temperature distortion on a turbofan engine. The purpose of this experiment was to gather data to validate a computational model presented in Walter and Shaw (1979). Three distortion cases were implemented in the analysis: total pressure, total temperature, and combined total pressure and temperature. Total pressure distortions were generated with a 50% blockage screen approximately one duct diameter upstream of the fan. Total temperature

distortion was generated with a 4 quadrant hydrogen burner approximately 6 duct diameters upstream of the fan. Highly instrumented measurement stations were placed immediately downstream of the burners and upstream of the fan inlet. The results shows that the total temperature distortion profile did not vary as it propagated through the inlet. The static pressure and corrected mass flow were uniform at the burner exit and fan inlet (Figure 2-4).

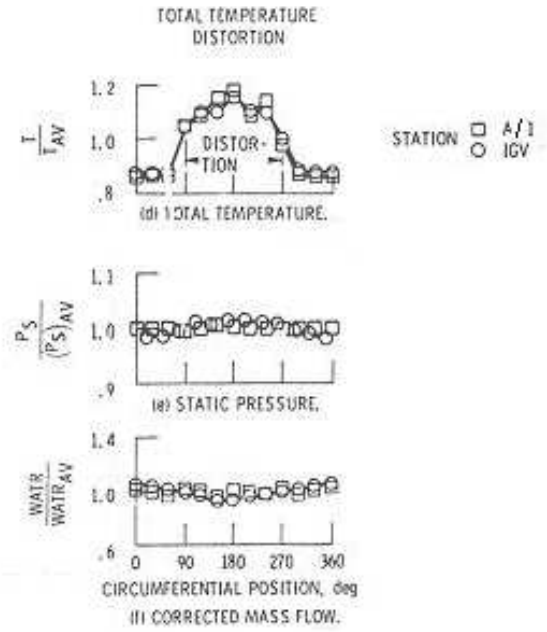

Figure 2-4: Circumferential flow field measurements from a 180^{o} total temperature distortion [Braithwaite et al., 1979]

(Reprinted by permission of the American Institute of Aeronautics and Astronautics, Inc.)

Fewer investigations related to the effects of thermal distortions on the performance and operability of a compressor have been conducted than for total pressure distortion. The material presented above covers some of the available literature on the performance and operability effects on a compression system due to thermal distortions.

Historically, engine companies have not investigated thermal distortions extensively due to expensive testing and the lack of government or industry guidelines (SAE, 1991). This document addresses the need to generate a set of guidelines to implement temperature distortion in gas turbine engine testing for the investigation of

effects on the compression system's performance and operability. Experiments presented in the SAE (1991) reference show that inlet temperature distortions can have an adverse effect on engine operability. Specifically, steady-state and transient spatial temperature distortions, which have been shown to lower the surge line of the compression system, limit the operating range of the engine. By limiting the operating range, the engine may suffer performance degradation since desired compressor pressure ratios may not be attained.

A time-varying thermal distortion, or thermal ramp, has an effect on engine operability as well. The application of a temperature ramp has an effect of raising the operating line of the engine closer to the stability limit. Individually, spatial distortions and temperature ramps reduce compressor stall margin. The combination of these two events may result in an additive effect, where stall margin can be drastically reduced (Figure 2-5).

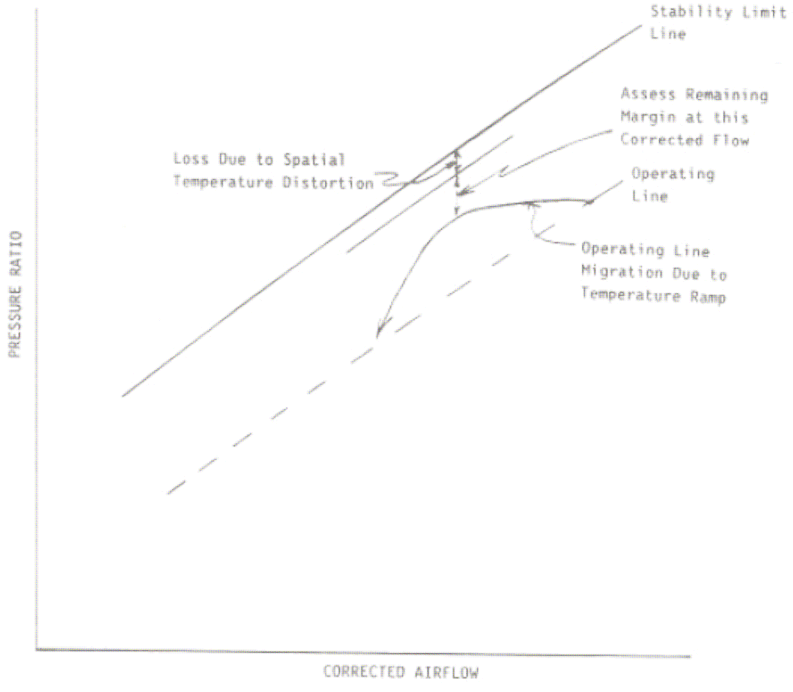

Figure 2-5: Compressor performance map of thermal distortion effects [SAE, 1991]

(Reprinted with permission from SAE ARD50015 © 1991 SAE International)

The referenced SAE document identifies means of avoiding inlet temperature distortions. One example of this deals with the design of an aircraft. Placing weapons near inlet of aircraft or where the weapon exhaust may enter the engine should be avoided if possible. Though the design of aircraft along with the armament they carry may attempt to avoid inducing inlet temperature distortions, temperature distortions are unavoidable for the entire flight envelop for many aircraft. Active flow control, used in total pressure recovery applications in the aircraft engine and the inlet duct, may introduce a thermal distortion to the flow. Aircraft applications that incorporate V/STOL or thrust reversers have the potential for hot gas reingestion. When in close proximity to the ground, impinging flow can be redirected back into the engine inlet.

Accommodating inlet temperature distortion is also discussed in SAE (1991). For example, in situations where the operator knows that a temperature distortion may be present (missile firing, for example), the operator may take a temporary tradeoff in operability to counteract the drop in stall margin due to the potential inlet total temperature distortion.

This document identifies the importance of investigating thermal distortions, proposing testing techniques and necessary instrumentation, and presenting a universal methodology which both government and industry can follow to evaluate the thermal distortion effects on gas turbine compression systems. No information regarding vibratory effects due to thermal distortions presented in this work.

There are a variety of methods to create thermal distortions. Heated jet flow is an example of a technique used to create thermal distortion that has been used in thermal distortion testing. DiPietro (1993) designed and evaluated a thermal distortion generator to be used in turbomachinery research. A four-quadrant burner design in an annulus was used to generate total temperature distortions in a straight duct. Results from this analysis indicated that total temperature distortions persist for many duct diameters downstream. At nearly eight diameters after the thermal distortion, the total temperature profile, though a bit diffused, has not changed significantly.

For his dissertation, DiPietro (1997) investigated thermal distortions, and focused on the effects of thermal transients on stall in a multistage compressor. It was determined that when under the influence of a rotating stall, a rotor has the potential to recover to a stable operating condition through the introduction of a thermal transient. This result is beneficial to the engine only when the compressor is stalled. Previous experiments had shown that spatial, transient, and "temperature-ramp" (dT/dt) thermal distortions tended to lower the pre-stall stability limit of a compressor operating in a stable condition.

A recent advancement in inlet technology introduces another possibility for the generation of total temperature distortion. Active flow control by air injection is a technique used in gas turbine engines whereby air flow in one part of the engine (normally the compressor) is extracted from the flow path such that the air can be injected in another area, to change flow characteristics at the desired station. "S-duct" inlets could incorporate this injection approach to deal with total pressure distortion due to flow separation as shown in Figure 1-1. Flow non-uniformity is caused by the turning, resulting in a total pressure distortion and flow vortex generation. To combat this problem, inlet designers can "bleed" (or extract) air from the compression system (on the order of 1-2% of mass flow) and inject it into the inlet. The location and orientation of the injectors has the potential to reduce the presence of total pressure loss, total pressure distortion and vortical structures. However, by introducing this high temperature and high-pressure air into the inlet, a thermal temperature distortion may be introduced. Air is heated as it passes through the compressor, and therefore, when reintroduced to the inlet air stream, a total temperature profile may be generated. Only a few investigations have focused on thermal distortions caused by flow injection or active flow control. The need to further understand this problem is addressed in this thesis by means of a modeled computational flow injection scheme incorporated with two duct geometries (straight and serpentine).

2.3.2 Aeromechanical Effects

There have been few investigations into the aeromechanical response of blades due to thermal distortion. Kenyon et al. (2004) computationally investigated the effects of a 3/rev total temperature distortion on transonic fan blades of modern design. Two independent CFD studies were investigated with distinct differences assumed in boundary conditions. The first study examined a total temperature distortion profile coupled with a constant total pressure profile boundary condition. The second study used the same total temperature boundary condition, and incorporated a radially varying, circumferentially constant axial velocity profile. Figure 2-6 shows the two specific boundary conditions used in this analysis.

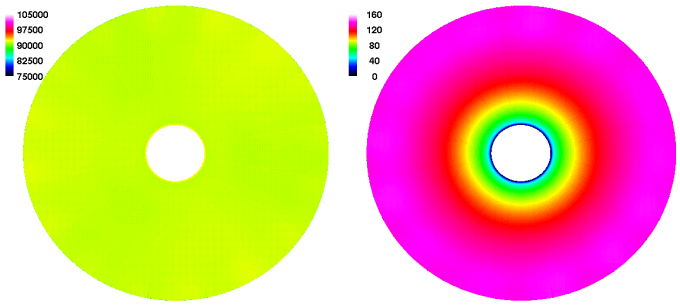

Figure 2-6: Uniform Total Temperature (a) and Constant Circumferential Axial Velocity (b) Boundary Condition used in Kenyon et al. (2004)

Three extents of trough-to-peak total temperature distortions (5 R, 20 R, and 25 R) were investigated for each of the studies. The purpose of this study was to deduce the extent of the distortion that would cause unsteady blade forces similar to those in the Wallace et al. (2004) computations. It was determined that both of these boundary conditions resulted in significant blade surface pressure variation for total temperature fluctuations of 25 R, yet the drivers of the unsteady forces were different. The constant circumferential velocity boundary condition study saw more significant on-blade shock movement. Alternatively, the variable blade loading of the constant total pressure boundary condition study was predominantly due to variation in flow incidence angle. The latter study resulted in higher blade loading fluctuation. Both studies revealed

significant levels of unsteady blade loading. Figure 2-7 presents plots of pressure coefficient at 85% span versus normalized axial chord for the (a) Wallace et al. (2004) analysis, where a total pressure distortion of 1 psia induced high unsteady blade loading, and (b) the 25 R extent total temperature distortion computations examined by Kenyon et al. (2004).

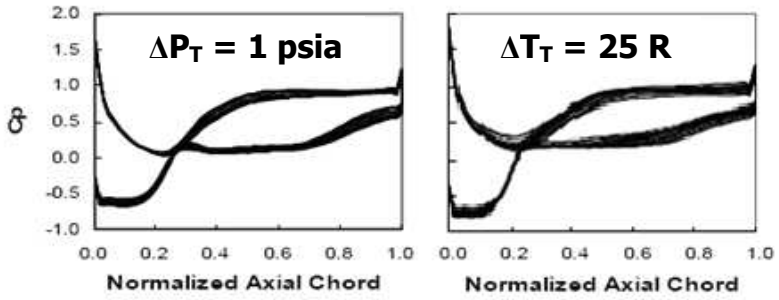

(a) (b)

Figure 2-7: Comparison of Pressure Coefficient for (a) Po and (b) To Blade Loading [Kenyon, 2004]

These plots show that the variations in pressure coefficient produced by the two types of distortion are comparable to one another, indicating that total temperature distortion has the potential to drive high unsteady blade loading. If the boundary conditions imposed in the Kenyon et al. analysis are accurate, this investigation, though purely computational, highlights that thermal distortions can potentially induce detrimental HCF-related blade vibration. Yet, the assumptions of the boundary conditions raise questions about the accuracy of the predictions. Therefore, a validation of the assumed boundary conditions is needed.

The present research addresses the above concerns through providing predictions of flow property variations at the compressor face in response to simulated thermal distortions, as well as providing new and independent results.

2.4 Literature Review Summary

The literature documented reveals important information about inlet distortions. In particular, it has been shown that total temperature distortions have a negative effect on performance and operability of the compressor and engine. Furthermore, the analysis performed by Kenyon et al. (2004) indicates that thermal distortions may have the potential to drive severe vibrations in fan and compressor blades, which can result in blade high cycle fatigue. On a whole, there is a lack of information regarding aeromechanical effects due to thermal distortion.

Various thermal distortion generation techniques have been identified in this literature review. Burners are predominately used to induce thermal distortion. There has been a limited amount of research on using heated air jets for thermal distortion creation. This research is valuable since inlet flow duct research incorporates air jet injection technology such as active flow control.

The literature revealed a lack of documentation on thermal distortion testing on compression systems. Braithwaite et al. (1973) indicated that in the event of a thermal distortion in the inlet, both static pressure and total pressure at the exit (the compressor face) should be constant. Unfortunately, there is a lack of circumferential and radial resolution in Braithwaite et al. papers. These boundary conditions were implemented in Kenyon et al. (2004) as an assumption for the computational analysis. Braithwaite et al. (1979) presented flow field measurements from a thermal distortion experiment. Results show circumferential measurements of a distorted total temperature profile, a constant static pressure profile, but do not present any total pressure measurements.

The literature review reveals that a better understanding of the thermally distorted flow profiles at the AIP or compressor inlet is necessary. The following chapter, Analytical Method, describes the computational approaches undertaken to obtain the boundary conditions at the fan inlet plane under the influence of a thermal distortion.

Two thermal distortion generation techniques are introduced and the methodology by which they were investigated is presented.

3 Analytical Method

The methodology used in this research to computationally analyze a thermally distorted flow in a duct and obtain boundary conditions at the AIP is presented in this chapter. The steps involved in choosing a thermal distortion generator are identified, along with the numerical methods applied to solve the problems. Two specific thermal distortion generators were evaluated in this report, and will be discussed in detail in the latter sections of this chapter.

3.1 Preliminary Evaluation of Thermal Distortion Modeling

Two analytical techniques were used to investigate the flow entering a compressor affected by thermal distortion. The first distortion generation modeling technique is the introduction of an idealized volumetric thermal source to distort the flow field. The advantage this technique is that it isolates the effects of adding thermal energy to a flow field without modeling a physical obstruction in the flow path which distorts the total pressure of the flow.

The second technique is the modeling of a physical realizable method that would introduce thermal distortions. As mentioned in the literature review, active flow control techniques can introduce thermal distortions as a consequence of their injection into the air flowpath. Active flow control is a process where high pressure and high temperature air is extracted from the compressor and is injected at various locations and orientations in the inlet flow on a control schedule. Small jets are used to energize the flow by locally increasing the total pressure in the flow. This application is beneficial for recovering total pressure but consequently introduces a thermal distortion.

A modeling technique to capture the effects of a thermal distortion on the flow field at the AIP was necessary for accurate boundary condition identification. Initially, a preliminary one-dimensional (1-D) analysis was implemented to gain insight into the impact on thermal distortion effects on AIP boundary conditions. The 1-D approach

indicated a variation in flow variables due to a thermal event. The one-dimensional approach does not suffice for detailed modeling of a thermal distortion and obtaining flow variables at the AIP due to the lack of circumferential and radial resolution. A three-dimensional computational modeling approach with a higher level of fidelity was needed to model these thermal effects.

Computational fluid dynamics (CFD) is a multi-dimensional fluid-flow modeling tool that uses a form of the Navier-Stokes equations to solve problems in a discretized environment. The Navier-Stokes equations are theoretically based equations governing fluid motion. CFD solves the Navier-Stokes equations through a meshed domain. By creating a representative geometry of the desired model, appropriately meshing the geometry, applying accurate boundary conditions to the problem, and designating specific initial conditions, one has the ability to understand the flow physics of the problem through the solution of Navier-Stokes equations. The accuracy of the solution is dependent on a variety of parameters including discretization resolution, turbulence modeling, boundary conditions, and basic assumptions (Newtonian fluid, steady-state, etc.).

This technique was applied to investigate the inlet thermal distortion problem. Thermally distorted flow through a duct was evaluated with CFD for both distortion-modeling techniques. The details of these modeling techniques associated with each CFD analysis will be discussed in Sections 3.3 and 3.4. A brief description of the meshing tool used to develop an appropriate discretized grid for the ducts is discussed in the following section.

3.2 Modeling and Numerical Methods

This research employed FLUENT 6.2, a commercial CFD code, to evaluate flow interaction with a thermal distortion in the inlet. Geometric rendering and meshing was implemented in GAMBIT 2.2.

3.2.1 Model Geometry Creation and Meshing

Duct geometries were three-dimensionally modeled in GAMBIT to represent full scale inlet ducts used in many aircraft inlet configurations. The ducts were partitioned to aid in the meshing process, giving more control over the mesh organization. The geometry and mesh for both ducts is discussed in Sections 3.3 and 3.4.

The partitioned volumes in the duct geometries were meshed with volume elements as shown in Figure 3-1. Elements are made up of nodes, edges, and faces, all of which are respectively connected together to form volume elements. In this investigation, two volume elements were used in each model's representation: a 5 node tetrahedron and an 8 node hexahedron element[1].

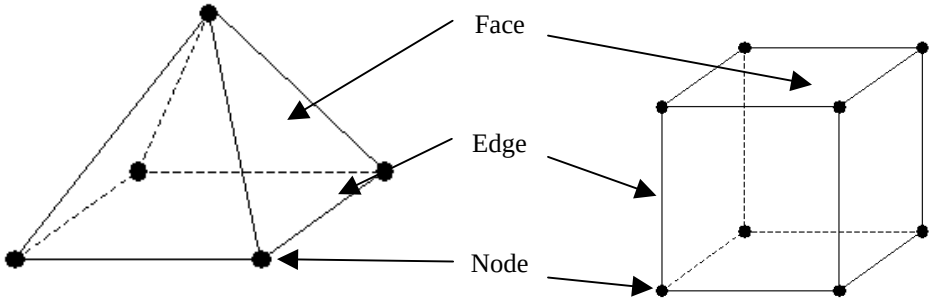

(a) 5 node Tetrahedron (b) 8 node Hexahedron

Figure 3-1: Volume elements used to mesh geometries

[1] All meshing in GAMBIT used two schemes to generate the entire volume meshes: the Cooper scheme (which employs hexahedral elements) and the Tgrid scheme (which uses tetrahedral elements).

There are specific advantages and disadvantages associated with the use of both of these elements. The hexahedron element is very useful in organized meshes. This element is more accurate than the tetrahedral element (Ferziger, 2002) and also number fewer than the tetrahedral for a specific node count. Because of this, the solution to a problem meshed with hexahedral elements can potentially be obtained faster than one meshed with tetrahedral elements. The disadvantage of the hexahedral element is that with complex geometries, meshing cannot be automated easily. It would take the user/modeler a long period of time to discretize volumes for a complex model using hexahedral elements that would interface well with other partitioned and meshed volumes. This is the major advantage of using the tetrahedral element. Meshing with the tetrahedral element can be automated easier, making this element more versatile. The downside of the tetrahedral element is a relative reduced accuracy of the element and the larger number of elements. The addition of more elements (higher resolution) to a mesh can increase solution accuracy, yet the time involved in the calculation increases. In the present modeling of the duct geometries, the general rule of thumb was to use hexahedral elements in the partitioned volumes where there was a high level of control over the volume meshing. In more complex areas where control over the mesh was difficult, tetrahedral meshing was employed.

An important aspect in meshing the model in CFD is creating a fine mesh in areas where high gradients occur in the flow. For instance, one of the most necessary areas for a fine grid is in a boundary layer region, since the velocity field changes drastically. Depending on the Reynolds number of the flow, the boundary layer resolution requirement can vary. Therefore, adaptation of the boundary layer grid may be necessary to adequate resolve the flow gradients. Inaccurate boundary layer resolution can result in misleading information referenced to adjacent free-stream flow and consequently may induce computational instability, convergence issues, and erroneous CFD solutions. Another source of solution inaccuracy is in transitioning between two different element types. Shifting between hexahedral and tetrahedral elements has the potential to cause solution inaccuracy. Grid adaptation where transition locations are found will yield a

more accurate solution. Regions where relatively lower flow gradients occur can be modeled with coarser meshes.

3.2.2 CFD Background

Fluid motion is described by the Navier-Stokes equations, which are temporal, and spatial-based equations governing the momentum transfer of the fluid. These equations are derived from the momentum equation. An empirically-based turbulence model is required for solution of turbulent flow problems. It is essential to stress that solutions to these equations are approximations of the working fluid's motion. Other governing equations that must be satisfied include the continuity of mass and conservation of energy of the fluid. The state of the fluid is determined by the ideal gas law in the compressible flow problem.

In this analysis, we are using the Navier-Stokes equations to model a turbulent, compressible flow in a duct. The model selected for both thermal distortion cases was the Reynolds-averaged version of the Navier-Stokes (RANS) equations, with a standard k-ε turbulence model. The governing equations used in the RANS computations and selected turbulence model are presented in the remainder of this section (FLUENT, 2005)

The Reynolds-averaged Navier Stokes equations assume that at an instant of time, the actual flow variable at a point in space can be represented by the sum of the time-averaged and fluctuating components, as shown in Equation 3-1. This is depicted in Figure 3-2, for a steady process.

$$\phi_i = \bar{\phi}_i + \phi_i' \qquad \textbf{3-1}$$

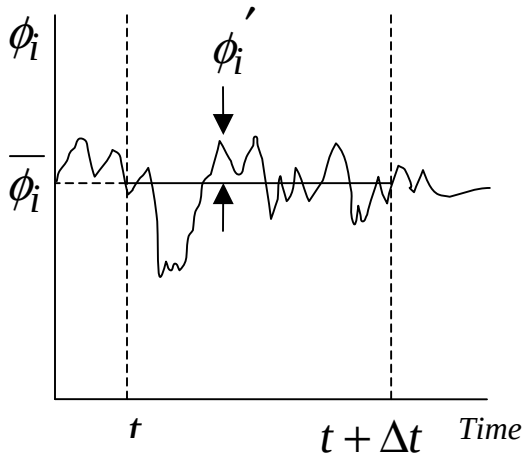

Figure 3-2: Mean and Fluctuating Components for a Steady Analysis [adapted from Blazek, 2001]

The time-averaged component can be defined in Equation 3-2 as the integral of the flow variable over a time internal, Δt, divided by change in time. Over a sufficient time period, the mean of the fluctuating component, $\overline{\phi_i'}$, in an otherwise steady-state flow, equates to zero (3-3).

$$\overline{\phi_i} = \frac{1}{\Delta t} \int_t^{t+\Delta t} \phi_i \, dt \qquad \textbf{3-2}$$

$$\overline{\phi_i'} = \frac{1}{\Delta t} \int_t^{t+\Delta t} \phi_i' \, dt = 0 \qquad \textbf{3-3}$$

Applying Equation 3-1, the sum of the mean and the fluctuating components of the velocity equals the total velocity (3-4). The velocity component is substituted in the conservation equations (Equations 3-5 and 3-6).

$$u_i = \overline{u}_i + u_i' \qquad \textbf{3-4}$$

The conservation equations of mass (3-5) and momentum (3-6) are presented below. In these analyses, the flow is steady (no time-varying flow gradients), and therefore we can ignore the time-varying partial derivatives ($\frac{\partial \phi}{\partial t}$).

$$\frac{\partial \rho}{\partial t} + \frac{\partial}{\partial x_i}(\rho u_i) = 0 \qquad \textbf{3-5}$$

$$\frac{\partial}{\partial t}(\rho u_i) + \frac{\partial}{\partial x_j}(\rho u_i u_j) = -\frac{\partial p}{\partial x_i} + \frac{\partial}{\partial x_j}\left[\mu\left(\frac{\partial u_i}{\partial x_j} + \frac{\partial u_j}{\partial x_i} - \frac{2}{3}\delta_{ij}\frac{\partial u_l}{\partial x_l}\right)\right] + \frac{\partial}{\partial x_j}(-\rho\overline{u_i' u_j'}) \qquad \textbf{3-6}$$

The momentum equation accounts for momentum flux through the system, forces acting upon the fluid, and stresses arising from viscosity and turbulence. The latter term is called the Reynolds stress, which accounts for momentum change due to varying turbulence levels in the flow. To "close," or solve the RANS equations, an assumption must be made about the Reynolds stresses. A common assumption is to employ the Boussinesq hypothesis as shown in 3-7.

$$-\rho\overline{u_i' u_j'} = \mu_t\left(\frac{\partial u_i}{\partial x_j} + \frac{\partial u_j}{\partial x_i}\right) - \frac{2}{3}\left(\rho K + \mu_t \frac{\partial u_i}{\partial x_i}\right)\delta_{ij} \qquad \textbf{3-7}$$

This equation expresses a linear relationship between the turbulent viscosity and the partial derivatives of the fluid velocity. The turbulent viscosity is defined in Equation 3-8 below, which incorporates the fluid density, a dimensionless constant, C_μ, and the turbulence kinetic energy, K, and turbulence dissipation, ε.

$$\mu_t = \rho C_\mu \frac{K^2}{\varepsilon} \qquad \textbf{3-8}$$

The energy equation is shown in Equation 3-9. This equation accounts for energy transfer throughout the system, thermal conductivity, energy change induced from viscous stresses and any thermal sources applied to the system. The thermal conductivity k_{eff} is a function of the thermal conductivity of the fluid and conductivity due to turbulence of the flow. Similarly, the stress tensor $(\tau_{ij})_{eff}$ is an "effective" term because the viscosity in this term is a function of both the flow viscosity and the effective flow viscosity due to turbulence.

$$\frac{\partial}{\partial t}(\rho E) + \frac{\partial}{\partial x_i}(u_i(\rho E + p)) = \frac{\partial}{\partial x_j}\left(k_{eff}\frac{\partial T}{\partial x_j} + u_i(\tau_{ij})_{eff} \right) + S_h \qquad \textbf{3-9}$$

There are numerous turbulence models available to model a suite of different flow conditions. Turbulence models are estimates of fluid dynamic behavior and are empirically determined. Because of the vast array of fluid dynamic applications, certain models are developed for specific applications. The turbulence model selected for the analyses was a standard $k-\varepsilon$ model. The versatility and robustness of this model for handling a wide variety of flow physics made this model an attractive choice. Equations 3-10 and 3-11 are the $k-\varepsilon$ transport equations used to solve for the turbulent kinetic energy and turbulence dissipation. Both equations account for turbulence variation due to velocity gradients (G_K), buoyancy (G_b), and compressible flow effects (Y_M) and any user defined sources of turbulence creation or dissipation (S_K and S_ε, respectively).

$$\frac{\partial}{\partial t}(\rho K) + \frac{\partial}{\partial x_i}(\rho K u_i) =$$

$$\frac{\partial}{\partial x_j}\left[\left(\mu + \frac{\mu_t}{\sigma_K} \right)\frac{\partial K}{\partial x_j} \right] + G_K + G_b - \rho\varepsilon - Y_M + S_K \qquad \textbf{3-10}$$

$$\frac{\partial}{\partial t}(\rho\varepsilon)+\frac{\partial}{\partial x_i}(\rho\varepsilon u_i)=$$

$$\frac{\partial}{\partial x_j}\left[\left(\mu+\frac{\mu_t}{\sigma_\varepsilon}\right)\frac{\partial\varepsilon}{\partial x_j}\right]+C_{1\varepsilon}\frac{\varepsilon}{K}(G_K+C_{3\varepsilon}G_b)-C_{2\varepsilon}\rho\frac{\varepsilon^2}{K}+S_\varepsilon \quad \textbf{3-11}$$

There are numerous dimensionless constants present in the $k-\varepsilon$ equations. The following parameters used in the present CFD analyses are listed below. They were determined empirically through experiments involving shear flows and wall bounded flows for air and water (FLUENT, 2005).

$$C_{1\varepsilon}=1.44,\ C_{2\varepsilon}=1.92,\ C_\mu=0.09,\ \sigma_K=1.0,\ \sigma_\varepsilon=1.3$$

These equations calculate the solution to the thermal distortion problems that were investigated. More information regarding the variables can be found in the nomenclature section in the beginning of the report, as well as additional equations presented in Appendix B. With the model generated and meshed, and the governing equations and turbulence model selected, boundary conditions can be applied to the problem.

3.2.3 Application of Boundary Conditions

An important aspect in solving numerical problems is the application of boundary conditions. From a rudimentary perspective, these boundary conditions serve as the known information about the flow at a surface (inlet, wall, and exit). The governing equations of the flow and selected turbulence model calculate the flow variation in the volume and determine other flow variables at the boundaries.

Once the model is rendered and meshed, the application of boundary conditions is required. In the present research, the flow in the inlet duct is considered to be compressible and turbulent. Application of true boundary conditions is a crucial step in approaching a solution of high fidelity. In the inlet duct, there are three main boundaries:

the inlet, a wall boundary and an exit. Information presented on the FLUENT website (www.fluentusers.com) reveals descriptions of proper boundary conditions for a compressible and turbulent flow. Possible boundary conditions which are appropriate for the CFD analyses are presented in Table 3-1, below.

Table 3-1: Suitable FLUENT Boundary Conditions for Compressible Flow

Boundary	Boundary Condition	Boundary Condition Description
Inlet	Mass Flow Inlet	Ability to apply the mass flow rate through a surface (Input: Mass Flow Rate, Total Temperature)
	Pressure Inlet	Ability to control the total pressure at a surface (Input: Total Pressure, Total Temperature)
Wall	Wall	Region between Fluid and Solid Medium
Outlet	Pressure Outlet	Ability to designate the static pressure at a exit/outlet (Input: Static Gauge Pressure)

The medium used in the analyses was air. No combustion products were modeled in the flow. In this case, the ideal gas law is obeyed. Specific boundary condition information for each of the investigated models will be discussed in Sections 3.3 and 3.4.

3.2.4 Meshing and CFD Summary

Each of the investigated models was meshed, boundary conditions were applied, and governing equations were solved. The following sections review the specific details associated with the modeling parameters for the thermal source CFD investigation and the flow injection CFD analysis.

3.3 3-D CFD Thermal Source Distortion Investigation

The initial interest in the thermal distortion investigation was to examine the amount of thermal distortion, along with any other subsequent flow distortion, that could be generated by the thermal sources. The potential was realized that this investigation could be compared the computational investigation by Kenyon et al. (2004). The thermal source investigation was then implemented to match the total temperature profile used in the Kenyon analysis (Figure 3-3). Total pressure, velocity, and static pressure boundary conditions could then be compared between both studies.

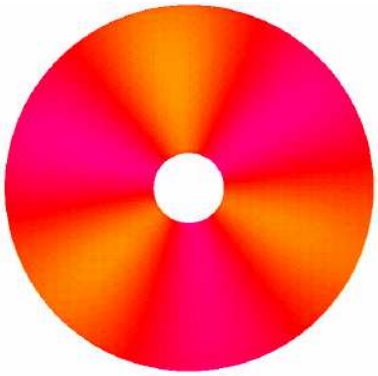

Figure 3-3: 3/rev, 25 R total temperature distortion profile [Kenyon et al., 2004]

One important conclusion from the Kenyon (2004) analysis was that computations revealed that total temperature distortions of 25 R have the potential to cause blade surface pressure variation similar in magnitude to a 1 psia pressure variation of the same pattern (Wallace et al., 2003). The CFD results were dependent on the boundary conditions applied at the AIP. There was a concern that at the AIP, two different boundary conditions could be applied; one of constant total pressure and one of constant circumferential velocity. It was determined that a thorough investigation of the boundary conditions was essential to validate the results of these boundary conditions. Therefore, a CFD model was developed to simulate flow passing through a thermal distortion (an idealized energy source in the flow) to examine the effects on the resulting exit flow field. By moving the CFD inlet far upstream where known boundary conditions

could be applied, the exit boundary conditions for the current analysis could be compared to the inlet boundary conditions implemented in the Kenyon et al. analysis at the AIP.

Initially, a geometric model was constructed in which a thermal distortion generator was implemented. The model followed the design of an AFRL Compressor Research Facility Experimental Research (CRFER) compressor that was configured to measure blade response to total pressure distortion produced by upstream-mounted screens. The design was the same CRFER compressor used in Manwaring et al. (1997) and Wallace et al. (2003). A schematic of the CRFER compressor is shown in Figure 2-1. The CFD model was constructed to represent the duct upstream of the compressor with an incorporated thermal source approximately at the location of the distortion screen.

The approach was to utilize GAMBIT and FLUENT to create and run a CFD model of the upstream duct of the CRFER. The geometry and meshed model is shown in Figure 3-4. The geometry was partitioned into three main axial sections: the inlet, the thermal distortion region, and the exit. Within the thermal distortion region, six circumferential volumes were created. Three volumes were created 90 degrees apart from one another, with a 30 degree circumferential extent. The remaining three volumes were placed directly adjacent to these volumes. A volumetric thermal source was applied to the three, 30^{o} sectors, to generate the thermal distortion. The thermal source distortion model heats the flow passing through the heated regions, which increases the total temperature of the flow, yet does not introduce any total pressure distortion due to a physical obstruction in the flow or any combustion products to the flow. Volumes were created upstream and downstream of the thermal distortion region to complete the geometry.

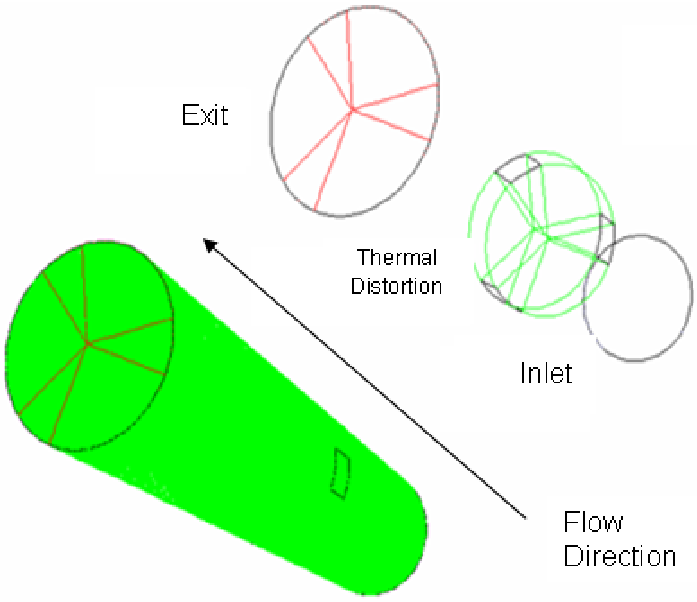

Figure 3-4: Meshed Cylindrical Duct Volume

Although the problem was modeled after the upstream CRFER duct, there are some distinct differences that should be noted. Upstream of the distortion, the inlet to the system was mapped to be 1.5 m long. This is more than two diameters upstream of the distortion, ensuring a developed flow passing through the thermal event. The width of the thermal distortion was set to be 0.2 m. The length from the thermal distortion exit to the exit to the computational domain was set to 1.73 m, which is approximately the distance from the distortion screen to the input to the computational domain and fan inlet (Kenyon et al., 2004). The fan inlet in the Kenyon et al. analysis is coined the AIP. This distance provides a similar mixing length to that used in the pressure distortion experiment.

The volumes were meshed adequately, with fine mesh regions around the walls to capture boundary layers and around the thermal distortion to track flow field gradients caused by the source term. Boundary conditions for the analysis are shown in Table 3-2.

Table 3-2: Boundary Conditions for Thermal Source CFD Analysis

Boundary	Boundary Condition	Value
Inlet	Mass flow, Total temperature	$\dot{m} = 45.9$ kg/s , T_T = 300 K
Wall	Wall	No Flux, Adiabatic
Outlet/Exit	Static pressure	P_{back} = -15 kPa (gauge)

The flow was analyzed with a uniform mass flow and total temperature at the inlet to the domain. The mass flow corresponded to the mass flow rate used in the Kenyon, et al. computations. The back pressure was approximated from inlet boundary conditions from the same analysis. This value was assumed constant, which is highlighted in previous experimental results presented by Braithwaite et al. (1973) and Braithwaite and Soeder (1979). Their research showed that in the event of a thermal distortion in a straight cylindrical duct, the static pressure downstream of the event rapidly becomes nearly uniform.

The energy (or, thermal) source was implemented in the CFD analysis by creating a User-Defined Function (UDF) in FLUENT. The UDF code implemented in the analysis can be found in Appendix C. FLUENT allows the user to import code to couple with the solver to suit modeling needs. In this case, a volumetric energy source of q''' = 8.5 MW/m^3 was applied to the three volumes of 30 degree extent. The value of the user-defined energy source is applied to the energy equation, Equation 3-9, in the variable S_h. This value was iteratively determined based on the need to obtain the desired exit total temperature extent of 25 R.

The computations were run on a 3 GHz Pentium 4 computer with 1 GB of RAM. Approximate computational times were on the order of 3-4 hours for a heavily meshed grid. The analysis was carried out with a segregated, 2nd order implicit, steady solver routine. A standard $k-\varepsilon$ turbulence model was applied and the default FLUENT turbulence parameters were used (FLUENT, 2005).

The solution was obtained by applying the specified boundary conditions to the problem and running the FLUENT solver governed by the flow momentum and continuity, turbulence, and energy equations. Convergence to the solution was obtained when specific residual values were achieved. These residual values were the default values used in FLUENT, being 10^{-6} for the energy equation and 10^{-3} for the continuity, momentum, and turbulence equations. The results of this analysis can be found in Section 4.2, where detailed plots of flow variables are presented.

3.4 3-D CFD Flow Injection Distortion Investigation

The previous approach was a theoretical method of applying an energy source to a flow path to obtain a desired total temperature distortion. This analysis though successful in developing total temperature distortions, did not represent a thermal distortion in a physically-realizable situation. Hence, another method to implement thermal distortions was desired to evaluate the total temperature boundary condition at the AIP.

In advanced inlets for military aircraft, inlet ducts similar to "s-ducts" are becoming more commonplace. The turning of the duct causes a local separation in the flow, which creates a low total pressure region in the flow. To combat this problem, flow injection can be used. Air which is extracted from the latter stages in the compressor can be routed to the inlet and injected at specific locations, orientations, and schedules. The benefit of placing the flow injector at the low total pressure region is a local increase in total pressure at the injector location and downstream regions of the flow. Injecting the high pressure inlet air reenergizes the flow, aiding in the overall total pressure recovery. A consequence of the injection, however, is that the injected air may introduce a thermal distortion to the flow field. The temperature rise over a single high performance compressor stage can reach approximately 80 R (Saravanamuttoo et al, 2001). Depending on the "bleed" location of the compressed air, the temperature of the injected air from the compressor may be substantially higher than the inlet core temperature. This tradeoff is a new issue which inlet designers and engine companies must investigate.

Injection of high pressure and high temperature air into aircraft engine inlets is certainly a feasible situation that may result in temperature distortion. It is desired to investigate this possibility in representative configurations found in the aircraft industry. Therefore, both straight and curved serpentine ducts are investigated to determine the magnitude and extent of the thermal distortion that could be present. The following sections introduce the methods in which the straight and serpentine "s-duct" analyses were implemented.

3.4.1 Flow Injector Design and Modeling

The dimensions, orientation, and operating conditions of injectors for flow control in engines can vary based on design and intended operation for the aircraft. An injector design representative of realistic active flow control applications was implemented (Rabe, P.C.). No attempt was made to optimize the configuration for inlet flow control. Table 3-3 provides the selected design.

Table 3-3: Flow Injector Parameters

Parameter	Value
Individual Injector Diameter	0.466 in (0.01184 m)
Injection Angle	45^o
Number of Injectors	9
Total Injection Flow Rate	2% of core flow
Injection T_o	+ 100 R from core flow
Duct circumference coverage	60^o

This information about the flow injectors will be used in all analyses presented herein. Note that the injection angle is relative to the tangent of the intersection of the flow injector and the wall. A visualization of these parameters is presented for the straight duct in Figure 3-5 and serpentine duct in Figure 3-7.

3.4.2 Straight Duct Investigation

The straight duct with flow injection was modeled with a different diameter than the previously discussed thermal source case in Section 3.3. A diameter of 18 inches (45.7 cm) was used to correspond with a current fan test at the Compressor Research Facility (WPAFB, OH). This straight duct flow injection analysis will serve for comparison and calibration of the thermal source modeling investigation. A view of the duct design can be seen in Figure 3-5, as well as a meshed 3-D rendered image of the duct.

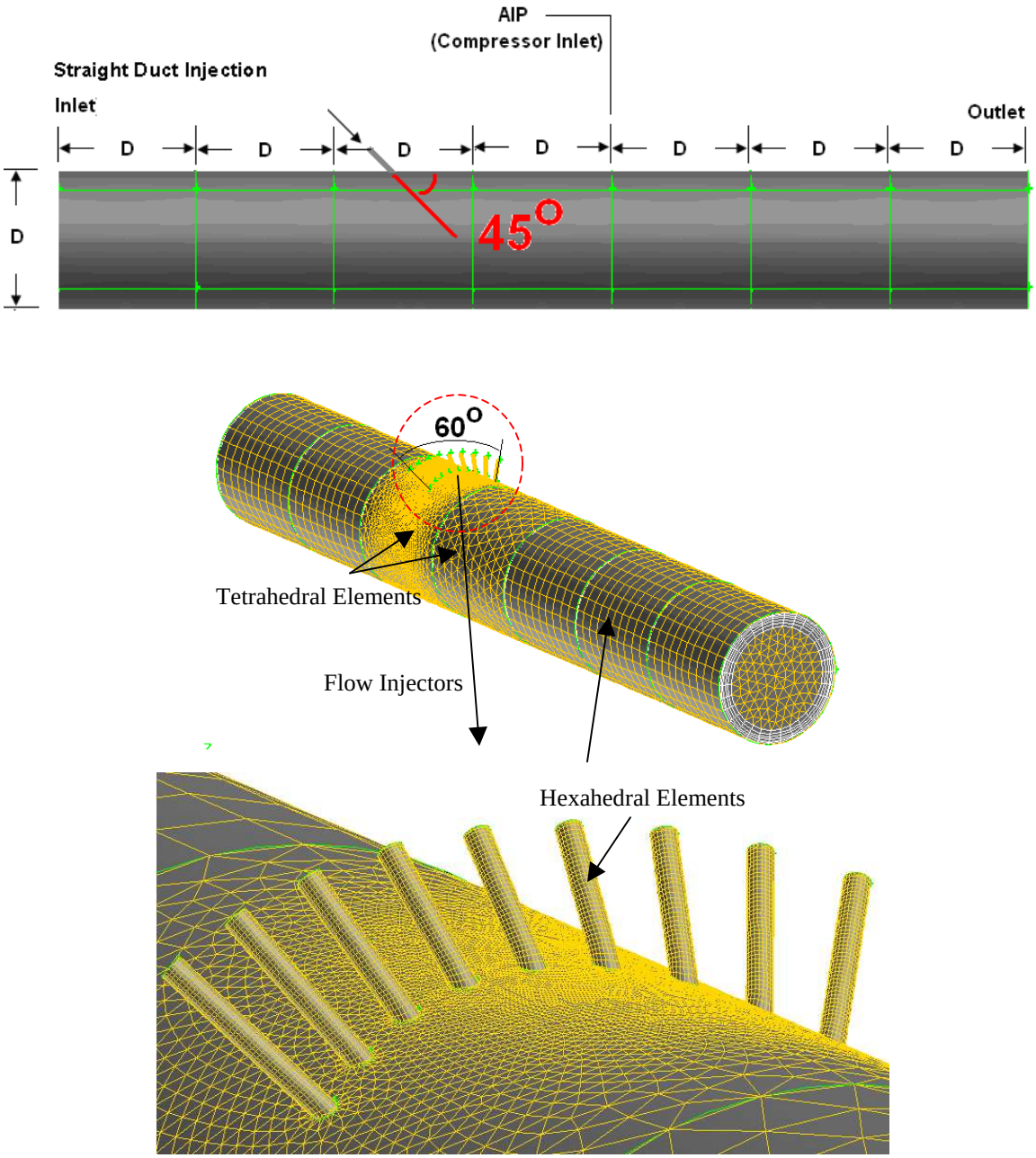

Figure 3-5: Straight Duct w/ Flow injection

The injectors are angled at 45° relative to the wall tangent and flow direction. All injectors are directed toward the centerline of the duct. Due to the relative location of the flow injector to the AIP, the AIP location could not be assumed to be the exit to the computational domain. An unknown static pressure profile was assumed to be present at

the AIP. However, three duct diameters were added to the end of the AIP such that a uniform static pressure profile could be assumed when the flow reached the outlet of the duct.

The core duct was partitioned into three volumes: the upstream inlet section, the flow injection region and the downstream region. This approach was implemented to provide more control over the meshing of the geometry. The upstream and downstream sections were meshed with sufficient boundary layer resolution to capture flow gradients near the duct wall region.

The duct geometry required high resolution meshes in specific locations. Due to the large aspect ratio from the large duct and small injector diameters, the injectors had to be finely meshed to capture adequate flow gradients. Boundary layers along the injector wall also required high resolution. The injector volumes as well were meshed with hexahedral elements. The region where the injectors intersect the main duct is an area of high gradient. This area will see large changes in temperature, flow direction, total pressure, and turbulence intensity. Therefore, this transition region was heavily meshed to capture the flow gradients. Tetrahedral elements were meshed in this region to link all adjacent volume meshes.

The boundary conditions applied to the model of the straight duct with flow injection are presented in Table 3-4. Two investigations for straight duct analysis are highlighted. The first analysis injects flow at the same temperature as the core flow, while the second analysis injects heated air (+ 100 R), both at 2% of the core flow. These two analyses provide the effects of thermal distortion to the flow field.

Table 3-4: Straight Duct with Injection Boundary Conditions

Boundary	Boundary Condition	Boundary Condition Description	
Core Inlet	Mass Flow Inlet	$\dot{m}_{core} = 22.68$ kg/s	$T_T = 288$ K
Injectors	Mass Flow Inlet	$\dot{m}_{core} = 0.0504$ kg/s	$T_T = 288$ K
			$T_T = 343$ K
Wall	Wall	No Flux, Adiabatic	
Outlet	Pressure Outlet	$P_{back} = 90$ kPa	

3.4.3 Serpentine Duct Investigation

The creation of the serpentine duct model was based on the Boeing 727 aft engine inlet design highlighted in the literature review (Figure 2-2). The inlet studied incorporates two 90^o bends with a constant circular cross-section. The bends are more severe than that of the 727 inlet, which may cause more flow energy loss. Figure 3-6 depicts the initial and the finalized duct geometry that was investigated in this analysis.

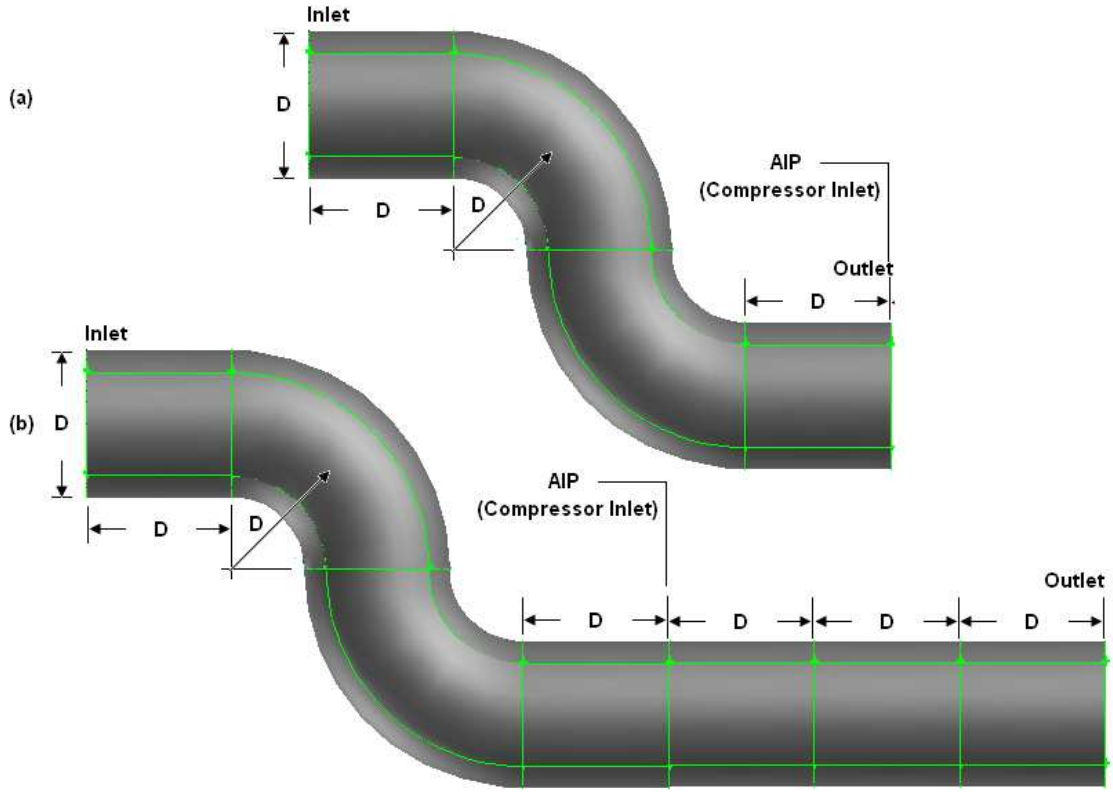

Figure 3-6: Initial (a) and Final (b) Serpentine Duct Geometry

The initial duct geometry (a) was based on a "short radius" design which means that the radius of curvature of the turns is equal to the diameter of the duct (D). The inlet consists of a straight duct of length 1D leading to the two 90^o bends. The AIP is located another 1D downstream of the second turn. This duct is quite representative of stealth aircraft inlets. Yet, knowledge of the exit boundary condition upstream of the compressor could not be conclusive. In other words, there was not enough confidence to define a pressure profile at that exit plane one duct diameter after the turn. To assume that the downstream boundary condition had minimal impact on the AIP, the downstream duct was extended three duct diameters past the AIP, similar to the straight duct model. It was assumed that the cross-sectional pressure profile four duct diameters beyond the turn is uniform. Yet, the actual plane we are interested in is the AIP, which is one diameter after the turning section. This extended serpentine duct is the geometry covered in this analysis.

The grid applied to the serpentine duct can be seen in Figure 3-7. Hexahedral elements were used in the straight duct portions, the first 90^o bend, and the flow injectors. Boundary layers were applied to all of these volumes. The second 90^o bend consisted of tetrahedral elements in three partitioned volumes. The middle of these three volumes served as the interface between the injector volumes and the core duct. The two adjacent volumes served as the transition between the interface mesh and the hexahedral meshes. This partitioning of the duct volume was implemented to have more control over the meshing and to aid the meshing process.

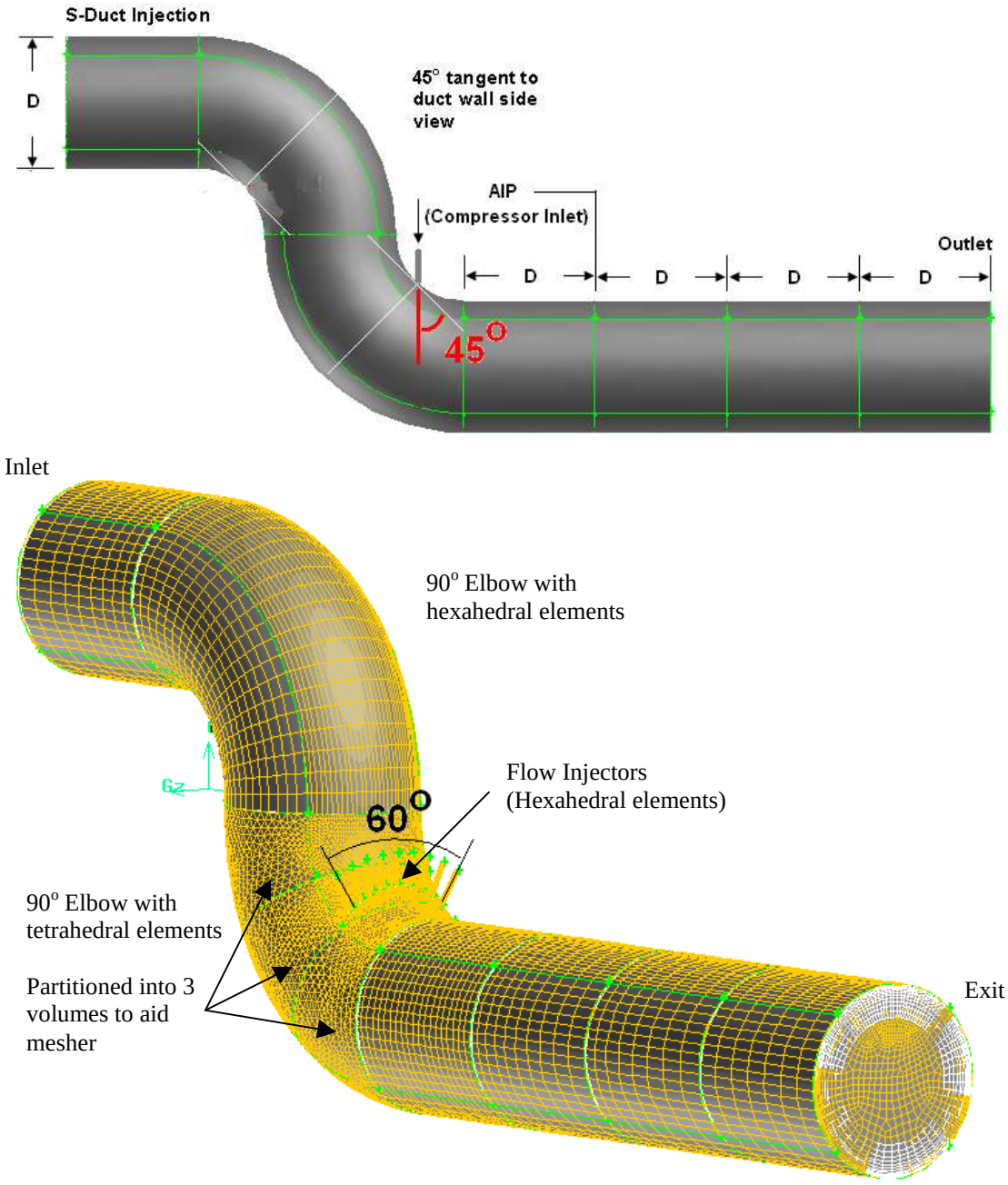

Figure 3-7: Serpentine duct mesh

Table 3-5 presents the investigated cases and boundary conditions applied to the s-duct. Three specific analyses are highlighted. The first identifies the flow's natural interaction with the duct. Hence, the aerodynamic and energy losses are solely due to the

duct curvature. This case served as a baseline of comparison for the remaining cases. The second investigation evaluates the effects of injecting the jets at the same temperature as the flow. We would expect no total temperature distortion, yet the velocity profile may be affected. Finally, flow injection at a higher total temperature (+ 100 R = + 55 K) is investigated. The active flow control jets were placed on the inner radius side of the second 90^o turn. This is depicted in Figure 3-8, above. One can anticipate that the placement of the jets, along with a suite of design variables, will affect the flow profiles at the AIP. This injection location was selected because there is a large region of total pressure loss on this inside turn that active flow control could improve. Injecting high total pressure flow at this location would reenergize the flow. Placing the jets relatively close to the AIP would serve as a possible "worse-case" scenario for flow injection, where the total temperature of the injected flow has less time to diffuse in the duct.

Table 3-5: Serpentine Duct with Injection Boundary Conditions

Boundary	**Boundary Condition**	**Boundary Condition Description**	
Core Inlet	Mass Flow Inlet	$\dot{m}_{core}$ = 22.68 kg/s	T_o = 288 K
Injectors	Mass Flow Inlet	$\dot{m}_{inj}$ = 0 kg/s	N/A
		$\dot{m}_{inj}$ = 0.0504 kg/s	T_o = 288 K
			T_o = 343 K
Wall	Wall	No Flux, Adiabatic	
Outlet	Pressure Outlet	P_{back} = 90 kPa	

4 Results and Discussion

The results for the two thermal distortion investigations are presented herein. Individual discussions of the results are found in Sections, 4.1 and 4.2. Section 4.3 compares the two analyses qualitatively and quantitatively.

To compare the thermal distortion analyses to one another, a distortion index was created. Equation 4-1 displays the percent distortion as a function of the difference between the maximum flow variable, $\theta_{\max}$, and the minimum flow variable, $\theta_{\min}$, normalized by the mass-weighted average, $\theta_{m.w.avg.}$.

$$\%\,Distortion = \frac{\theta_{\max} - \theta_{\min}}{\theta_{m.w.avg.}} \qquad \textbf{4-1}$$

4.1 3-D CFD Thermal Source Distortion Investigation Results

Obtaining a 25 R extent total temperature profile at the AIP was an iterative process. It required modifying the energy input into the system to result in the desired total temperature variation. A volumetric heat source value of q''' = 8.5 MW/m^3 resulted in the desired exit total temperature extent for the heated 30 degree heating volumes. The back pressure was assumed to be approximately -15 kPa (gauge). Figure 4-1 displays the exit total temperature profile calculated through the thermal source CFD analysis.

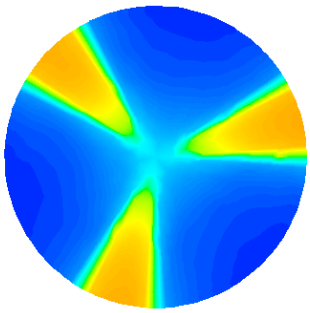

Figure 4-1: Exit total temperature (K) profile from the Thermal Source CFD analysis

This profile matched the Kenyon et al total temperature boundary condition of 25 R, 3/rev distortion. There are slight radial and circumferential variations in the total temperature profiles, but both total temperature profiles correlate well to one another. Therefore, the static pressure, total pressure, and velocity boundary conditions can be compared to one another as well.

Results of the flow field static pressure, total pressure, total temperature, Mach number and velocity for the straight duct thermal source case are presented in Figure 4-2 through Figure 4-6. For each flow variable, four plots are presented to convey the flow behavior. The axial flow plot (a) displays a specific flow variable sampled at each interior node in the mesh along the axial length. The inlet to the duct is located at zero axial distance and the exit to the duct (AIP) is located at 3.43 m. The thermal distortion is located from 1.5 m to 1.7 m. The three remaining plots (b, c, and d) are color contour plots of the flow domain: an isometric contour plot, an AIP contour plot, and a duct cross-section plot displaying flow entering and exiting the thermal source (respectively). Scales for the contour plots are presented with each plot to designate the magnitude of the variable in question.

The inlet static pressure was calculated to be -14.35 kPa (gage) and Mach number equated to 0.335 for the specified mass flow rate and duct geometry. Both of these values varied a small amount radially and circumferentially. As the flow passes through the thermal distortion, the flow variables change sharply. The static pressure (Figure 4-2) continually drops from inlet to exit. The flow passing through the heated volumes has a larger pressure drop than the flow passing through the non-heated volumes. At the AIP, displayed in Figure 4-2 (c), the static pressure was nearly a constant -15 kPa (gauge) over the cross-section of the flow, which was the designated exit boundary condition.

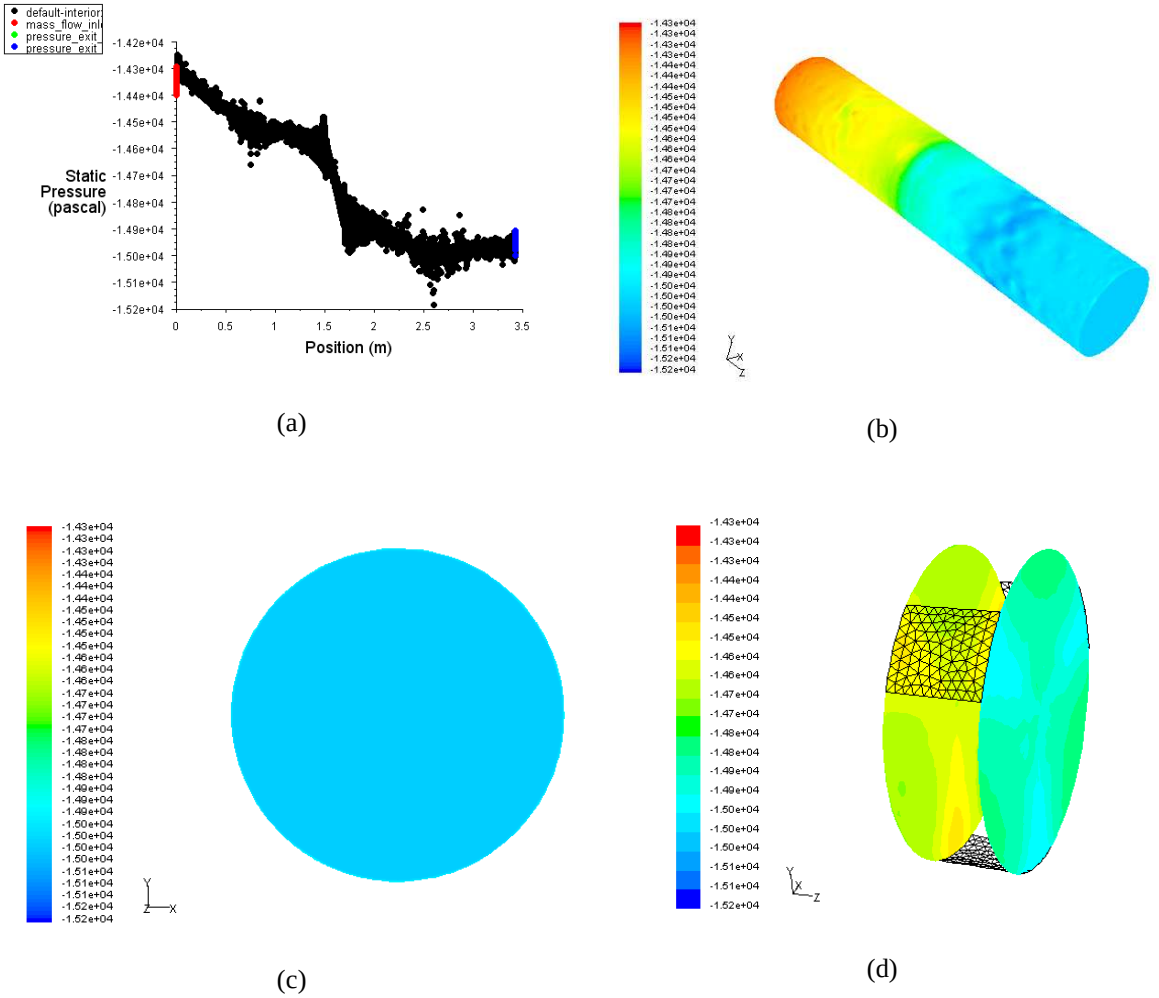

Figure 4-2: Axial (a), 3-D-contour plot (b), exit contour plot (c) and thermal distortion inlet/exit contour plot (d) for static pressure (Pa, gauge)

The thermal distortion imposes a small total pressure distortion on the flow (Figure 4-3). The flow passing through the heated volumes raises the total pressure while flow passing through the non-heated section drops. There is a low total pressure region created in the center of the duct when flow passes through the distortion. The 3/rev content can clearly be seen, yet the energy input in the flow does not cause a significant total pressure variation since it varies only ± 0.75 kPa at the AIP. These results are intriguing because of the fact that in conventional distortion testing, the main driver for total pressure loss is energy loss in the forms of physical obstruction in the flow

producing irreversibilities. In this analysis, total pressure loss is predicted, yet there are no physical flow obstructions interacting with the flow.

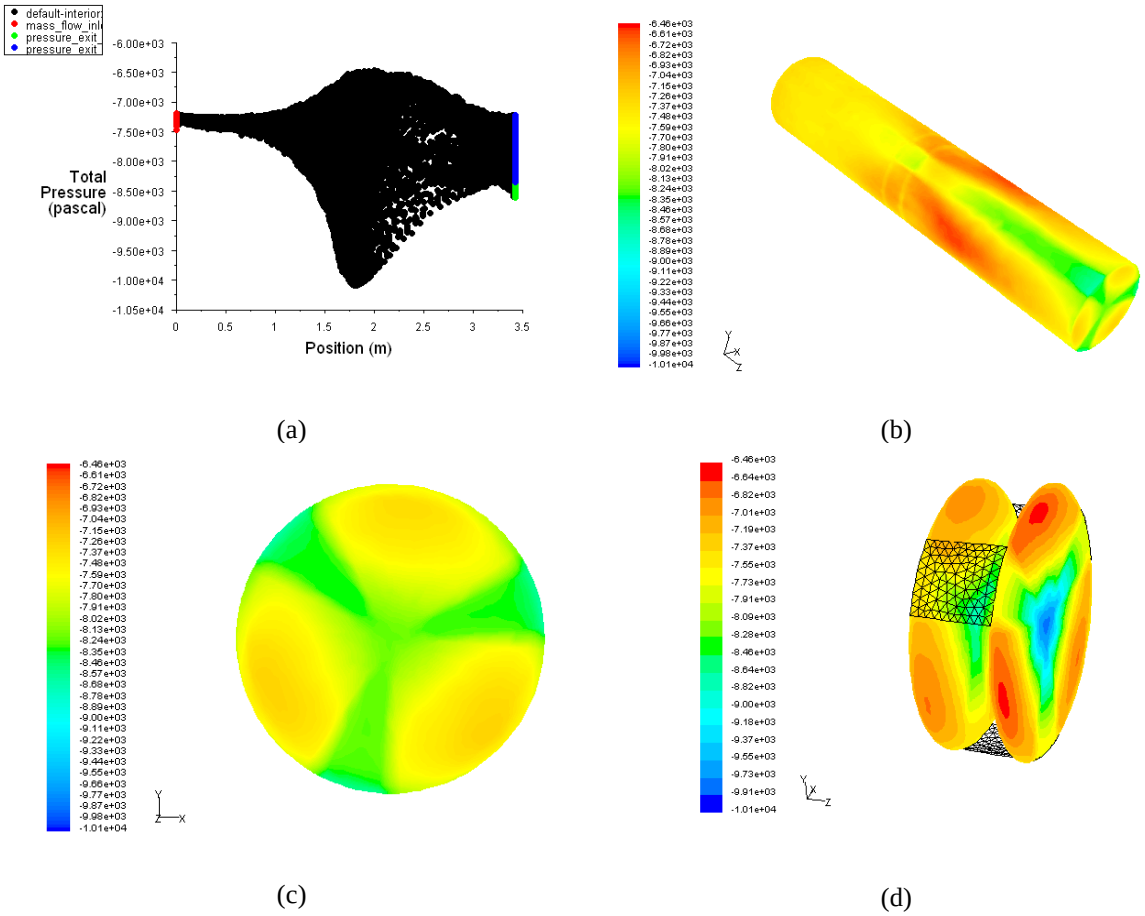

Figure 4-3: Axial (a), 3-D-contour plot (b), exit contour plot (c) and thermal distortion inlet/exit contour plot (d) for Total Pressure (Pa, gauge)

The total temperature is noticeably distorted by the modeled thermal source. The total temperature is increased through the heated section and remains nearly constant when passing though the non-heated section. The maximum total temperature is seen near the centerline of the duct (Figure 4-4). The AIP total temperature profile has a minimum and maximum temperature of 300 K through 314.1 K, respectively. This corresponds to a 4.49% total temperature distortion.

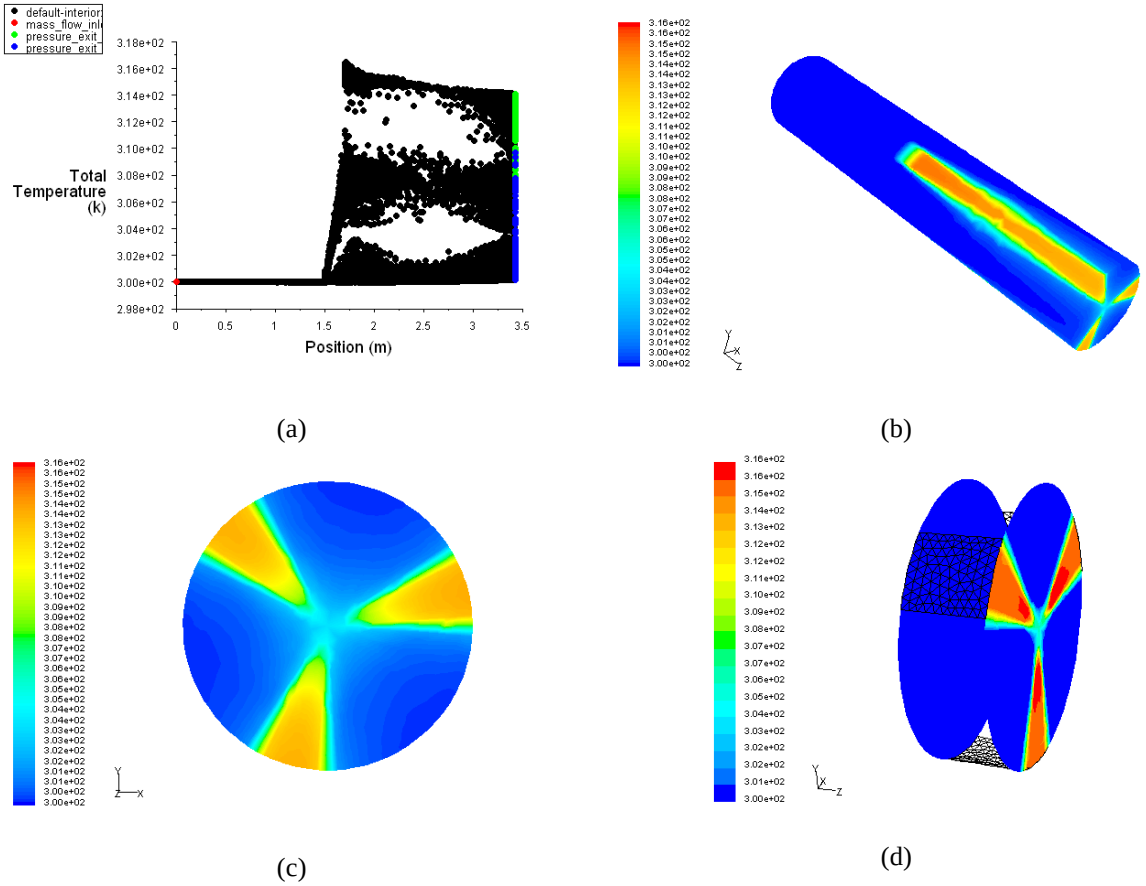

Figure 4-4: Axial (a), 3-D-contour plot (b), exit contour plot (c) and thermal distortion inlet/exit contour plot (d) for Total Temperature (K)

The thermal distortion has an interesting effect on the local Mach number. In both the heated and non-heated sections, the Mach number is increased, yet more so in the non-heated section (Figure 4-5). At smaller radii, the Mach number is decreased, creating a low Mach number flow section in the center of the duct. Exit Mach numbers varying from approximately 0.32 to 0.35 circumferentially, as seen from the heated and non-heated sections, which yields a 9.5% distortion in Mach number.

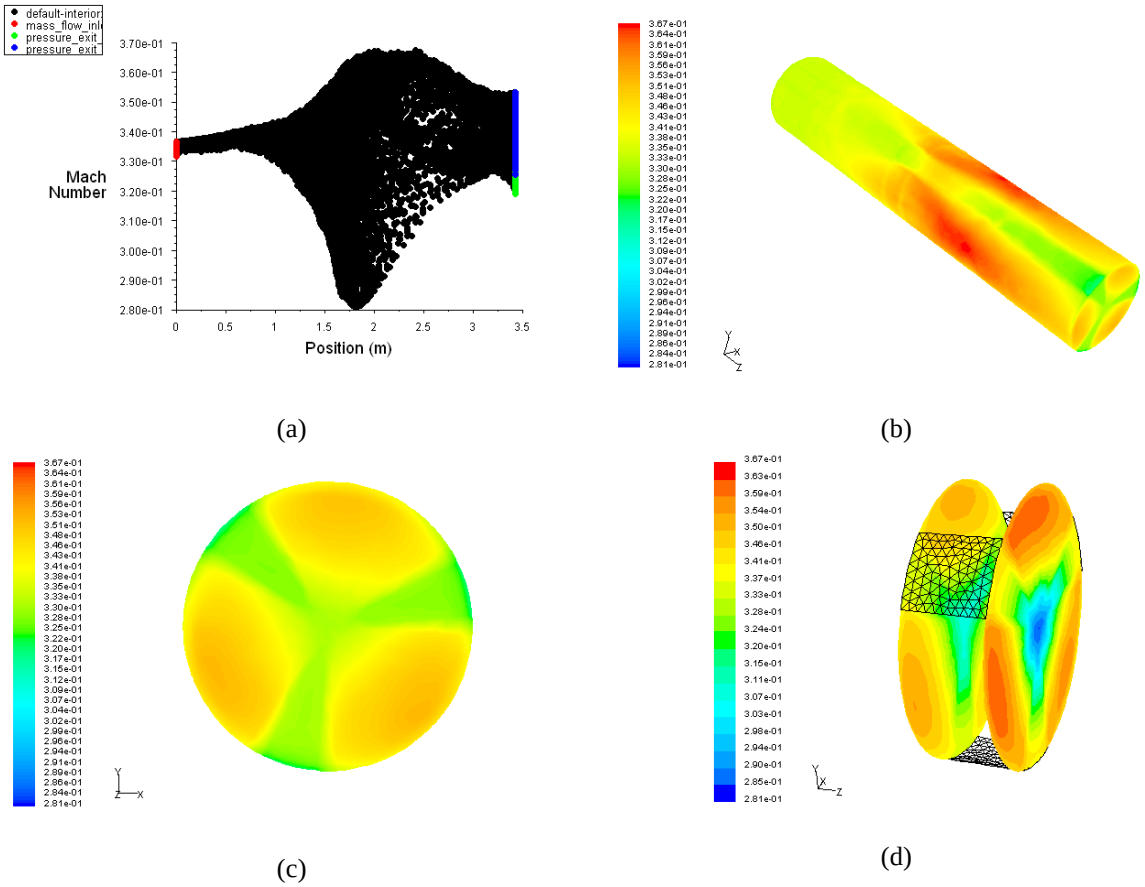

Figure 4-5: Axial (a), 3-D-contour plot (b), exit contour plot (c) and thermal distortion inlet/exit contour plot (d) for Mach number

The velocity distributions are shown in Figure 4-6. The radial velocity at the exit is less than 1.5 m/s, and therefore does not dominate the velocity magnitude of the flow. The major contributor to the flow velocity is axial flow. At the inlet to the system, the flow velocity is a near constant 115 m/s. The thermal distortion has the effect of increasing the flow velocity near the outer radius more than at the inner radius. The velocity normal to the exit plane ranges from 113 m/s to 123 m/s. There is a noticeable 3/rev pattern, indicating a circumferential velocity change. The velocity profile at the AIP varies 7.33%.

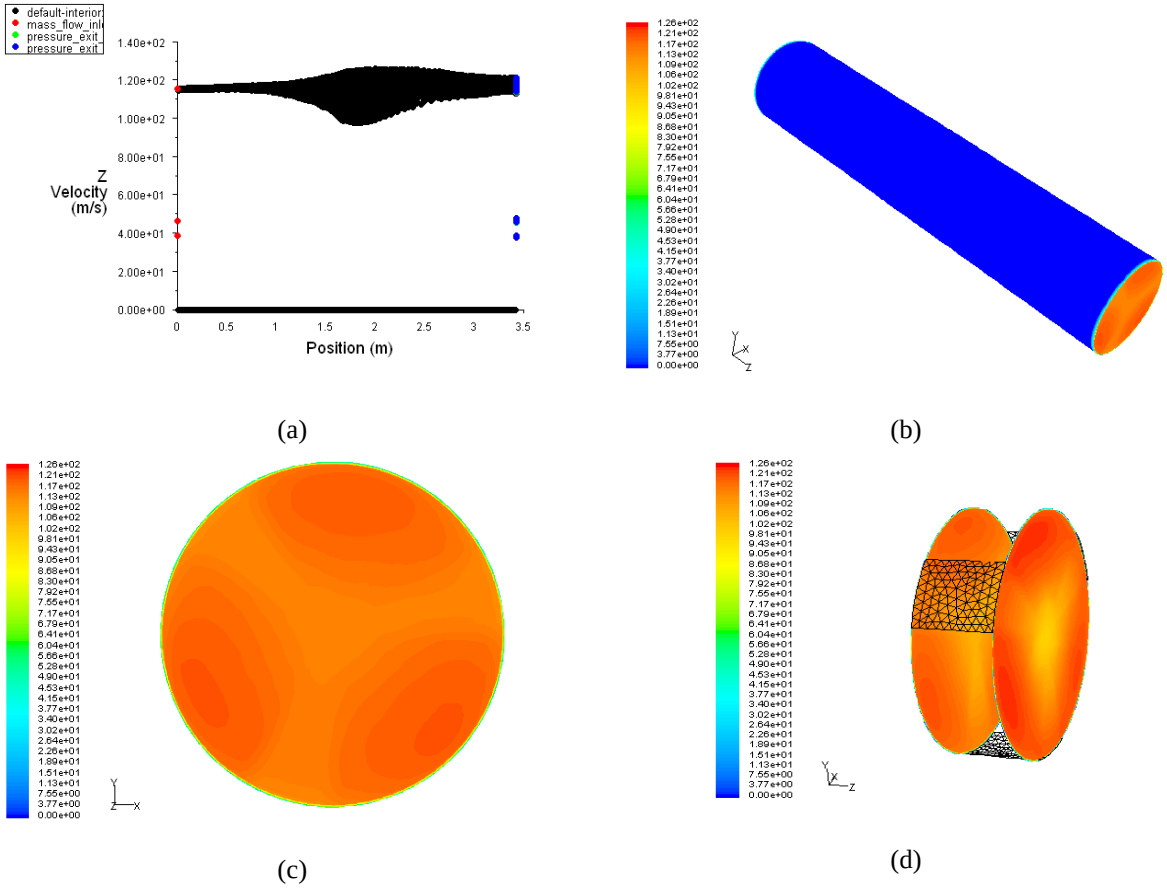

Figure 4-6: Axial (a), 3-D-contour plot (b), exit contour plot (c) and thermal distortion inlet/exit contour plot (d) for axial (z) velocity (m/s)

From the thermal source investigation, total temperature patterns were found that produced the desired 25 R varying total temperature boundary condition. The related flow variables (P_T, M, and V) varied due to the thermal source. At the exit profile (AIP), the total pressure varied by approximately 1.5%. This small total pressure distortion indicates that the uniform total pressure boundary condition used in the Kenyon et al. analysis may be appropriate for this level of thermal distortion. However, for larger distortions, the following analysis shows that the assumption of constant total pressure at the AIP is not accurate.

The velocity and Mach number distortions are largely affected by the thermal distortion, varying by 7.33% and 9.55%, respectively, at the AIP. Hence, a constant circumferential velocity boundary condition may not be proper boundary condition at the AIP due to a thermally distorted flow. The following section presents the results from the flow injection analysis.

4.2 3-D CFD Flow Injection Distortion Investigation Results

Results for the straight duct and serpentine duct investigations are presented in Section 4.2.1 and 4.2.2. The straight duct investigation involves a "cold" and "hot" injection (+ 0 R and + 100 R), relative to the core flow temperature. This approach is presented in the serpentine duct analysis, along with a case without flow injection.

In reporting the data for the flow injection analyses, two contour plots will be presented for the total temperature, total pressure, static pressure, Mach number, and velocity. The first plot is a centerline contour plot of the duct (a). This plot represents a symmetrical, centerline cut of the duct when looking from the side view. The second plot presents the AIP flow variable contour (b).

4.2.1 Straight Duct with Flow Injection

An analysis with a straight duct with no injection was not investigated due to the triviality of the solution. Since there are no drivers of flow profile distortion other than the small boundary layer region, this analysis was not performed.

Cold Flow Injection, Straight Duct

The intent of the first straight duct injection analysis was to model the injection of control fluid at the same total temperature as the core flow. Intuitively, there should not be a noticeable total temperature distortion cause by the injectors. Figure 4-7 supports this statement. The total temperature contour plots indicate no significant variation in total temperature (0.125% T_T distortion). The small variation in total temperature can be attributed to turbulence generated by the flow injection.

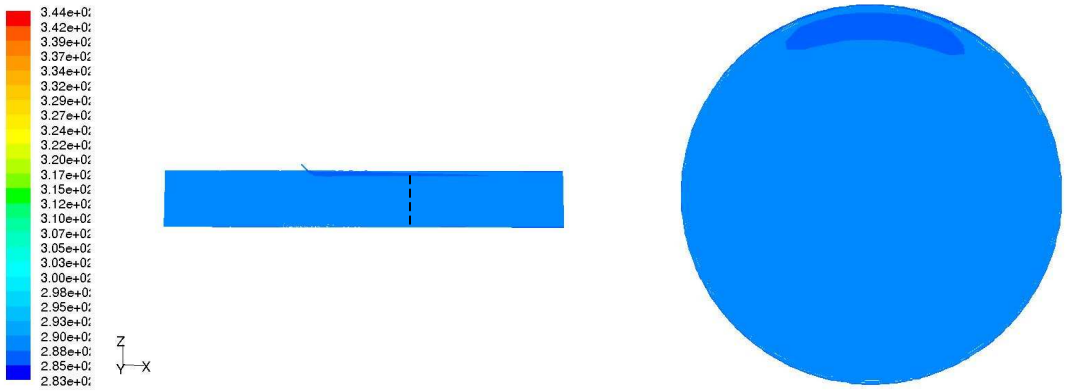

(a) Centerline Side View (b) AIP Cross-section

Figure 4-7: Total temperature (K) contours (straight duct, cold injection)

High total pressure flow is injected into the flow creating a distorted total pressure profile region that persists through the system. The AIP shows a 60^{o} region near about 70% span where total pressure is high, resulting in an 8.535% distortion, shown below.

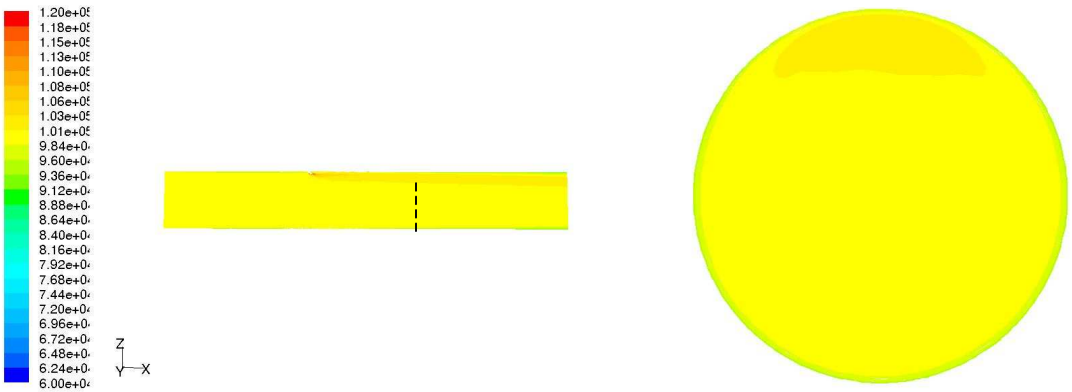

(a) Centerline Side View (b) AIP Cross-section

Figure 4-8: Total pressure (Pa) contours (straight duct, cold injection)

The static pressure in the system is nearly constant throughout the core flow path at 90 kPa (Figure 4-9). The jets have high pressure fluid in them but reach the core flow pressure through a throat shock structure. At the AIP, a negligible static pressure distortion is present (0.345 % distortion).

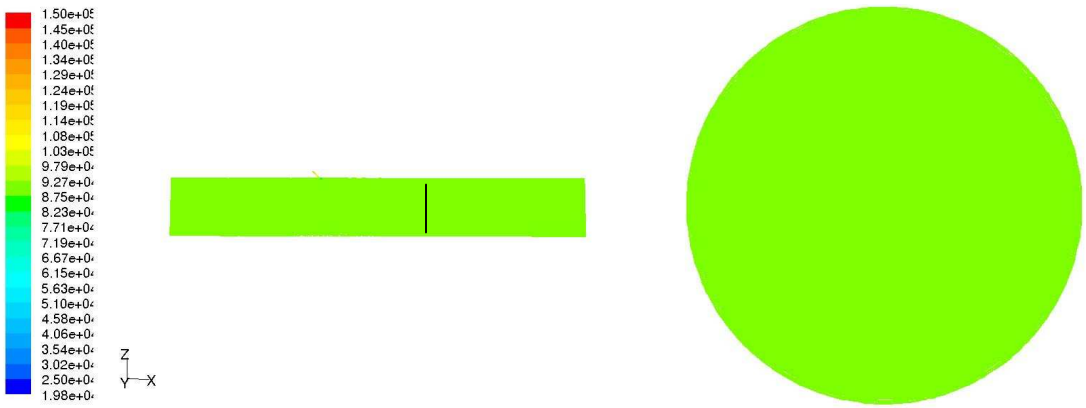

(a) Centerline Side View (b) AIP Cross-section

Figure 4-9: Static pressure (Pa) contours (straight duct, cold injection)

The Mach number profile is distorted by the injected flow (Figure 4-10). There is a large pocket of higher Mach number at the top of the duct. The amount of distortion caused by the injection is about 52%, which is the dominant distortion at the AIP.

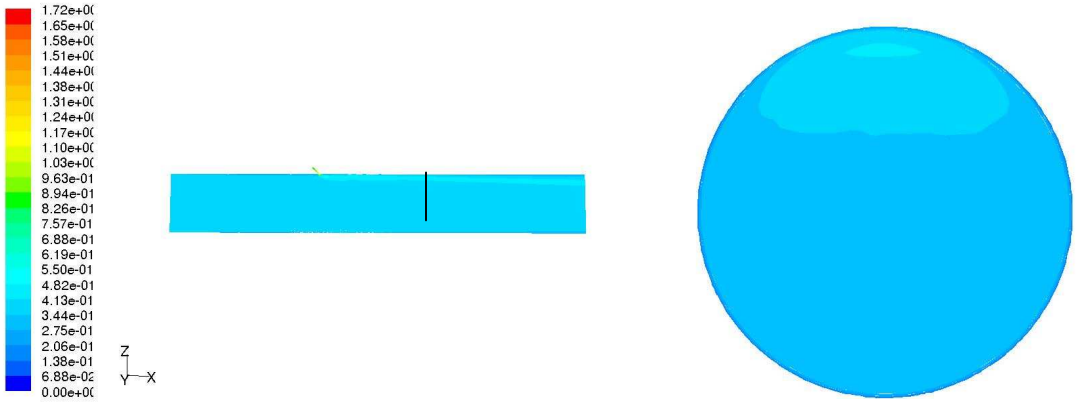

(a) Centerline Side View (b) AIP Cross-section

Figure 4-10: Mach number contours (straight duct, cold injection)

There is a small region of velocity magnitude distortion at the top of the duct (Figure 4-11). Also noticeable is a ring of low velocity on the outer circumference of the duct. This distortion was attributed to a numerical issue with the CFD code. In the center duct region, where the injectors and adjacent duct volumes interfaced, tetrahedral mesh elements were used in the analysis. Elsewhere, hexahedral elements were used to mesh the flow domain. The transition from the hexahedral elements to the tetrahedral elements seemed to create a false turbulent region, which added some error to the

calculation. More elements were added along the wall to better capture the flow transition, yet similar results were produced. With additional elements added in the boundary layer region, the numerically generated turbulence region issue might be resolved. This turbulent region only seems to affect the outer radius of the duct that is not in the flow injection region of the AIP. It can be assumed that the predictions for the top portion of the duct are accurate, while the remainder of the outer circumference will contribute to some error in the problem. The cold injection caused a 51% variation in velocity magnitude at the AIP.

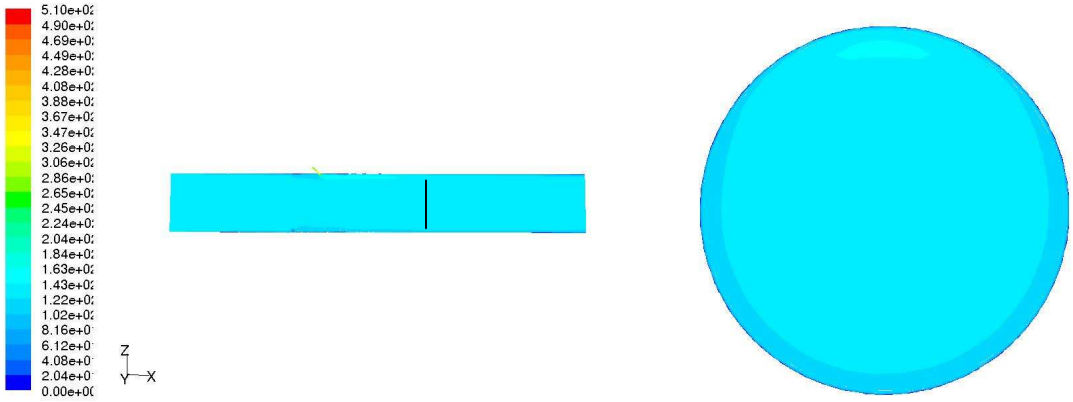

(a) Centerline Side View (b) AIP Cross-section

Figure 4-11: Velocity magnitude (m/s) contours (straight duct, cold injection)

The Mach number and velocity magnitude AIP profiles are substantially distorted due to the flow injection. The AIP profiles presented do not convey sufficient contours to discuss this distortion in detail. Appendix A presents tabulated data of the maximum, minimum, average, and distortion index for each flow variable.

Hot Flow Injection, Straight Duct

The hot injected air covers greater than 90 degrees of the duct circumference by the time the flow reaches the AIP as seen in Figure 4-12. The injected flow covers a 20% radial incursion. A total temperature distortion of 4.56% was developed at the AIP. After the flow injection location, the total temperature magnitude and extent does not vary excessively. Since the duct is straight, there are no geometric effects that cause the flow to mix. A curved duct with hot flow injection would induce more diffusion of total

temperature due to geometric effects. Therefore, the straight duct would sustain a higher total temperature distortion.

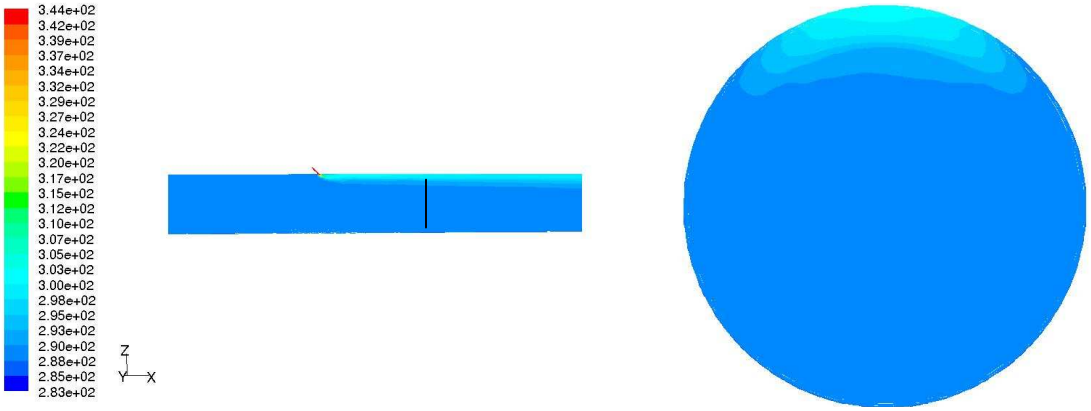

(a) Centerline Side View (b) AIP Cross-section

Figure 4-12: Total temperature (K) contours (straight duct, hot injection)

The total pressure contours in the heated flow injection case are quite similar to those from the cold injection (Figure 4-13). There are no substantial differences in the "cold" and "hot" total pressure profiles. At the AIP, the total pressure distortion covers approximately a 70-degree circumferential extent and a radial incursion of 40%. The total pressure distortion at the AIP was approximately 7.8%. The results presented in the "cold" injection case indicate that injecting flow at different temperatures with a constant mass flow does not change the total pressure profile substantially in the straight duct.

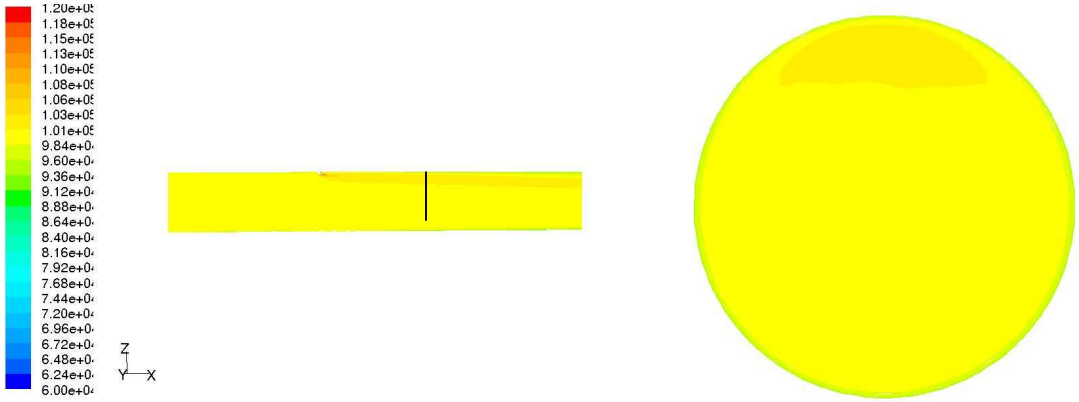

(a) Centerline Side View (b) AIP Cross-section

Figure 4-13: Total pressure (Pa) contours (straight duct, hot injection)

As expected, the static pressure contours are constant throughout the duct (Figure 4-14). In the flow injection region, there is a very small amount of static pressure distortion, but the distortion attenuates quite quickly. A static pressure distortion of 0.323% is experienced at the AIP, which is comparable to the "cold" injection case.

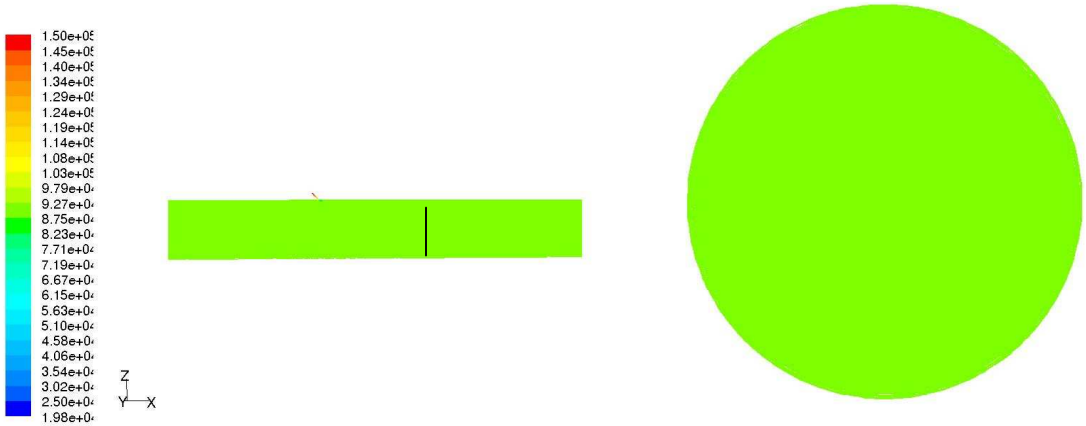

(a) Centerline Side View (b) AIP Cross-section

Figure 4-14: Static pressure (Pa) contours (straight duct, hot injection)

There is a small distortion in Mach number cause by the flow injection (Figure 4-15). The distortion generated from the hot injection results in a 48.6% Mach number variation at the AIP. This value is slightly lower than the cold injection case.

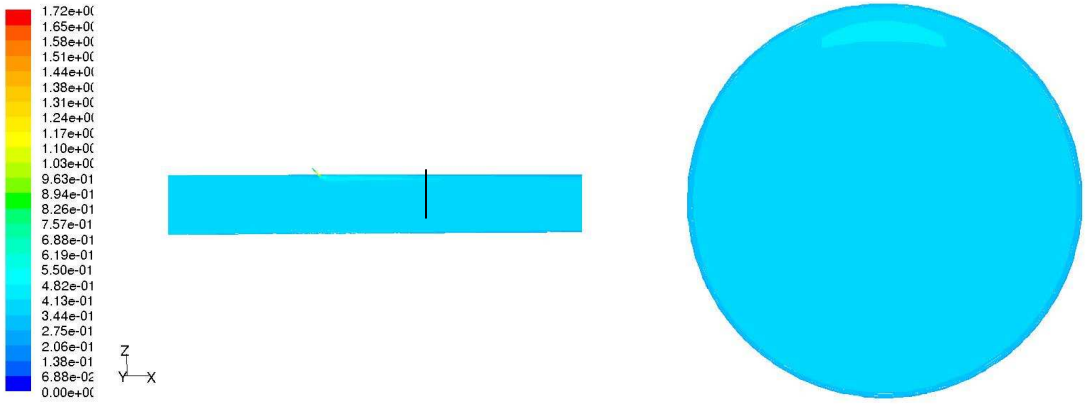

(a) Centerline Side View (b) AIP Cross-section

Figure 4-15: Mach number contours (straight duct, hot injection)

The flow injection induces a velocity distortion in addition to the introduction of the total pressure and temperature (Figure 4-16). The injectors create 49.6% velocity magnitude distortion at the AIP. This higher velocity region is not as visually evident as the large low velocity region around the majority of the outer wall region. This flow distortion, similar to the results of the cold injection analysis, was attributed to the transition between the meshed volumes with different element types. A comparison of the hot and cold flow injection cases for the straight duct is presented in Appendix A.

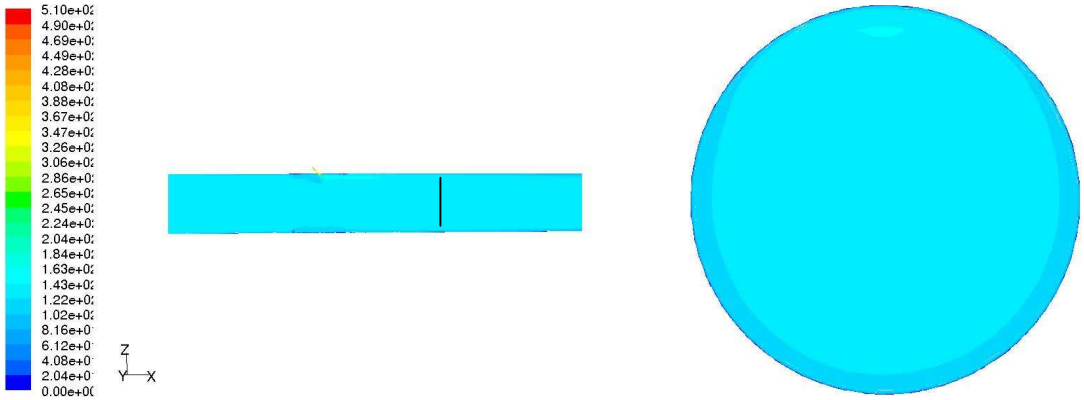

(a) Centerline Side View (b) AIP Cross-section

Figure 4-16: Velocity magnitude (m/s) contours (straight duct, hot injection)

4.2.2 Serpentine Duct

The knowledge of boundary conditions in CFD is vital for realistic fluid dynamic modeling. As mentioned in the previous chapter, an extended serpentine duct was analyzed to investigate the flow conditions associated with temperature distortion at the AIP. A straight duct of length equal to three duct diameters was added after the AIP since the static pressure could not be assumed uniform at the AIP. As for the previously described cases, a uniform static pressure profile was assumed to be uniform at the exit to the domain.

Presented below is a qualitative comparison between the initial ("short") duct design and the ("extended") final design. Figure 4-17 displays color contour plots of total and static pressure for both ducts along the duct centerline cross-section. Both ducts had the same boundary conditions applied to the inlet and exit. There was no flow injection implemented in these computational runs.

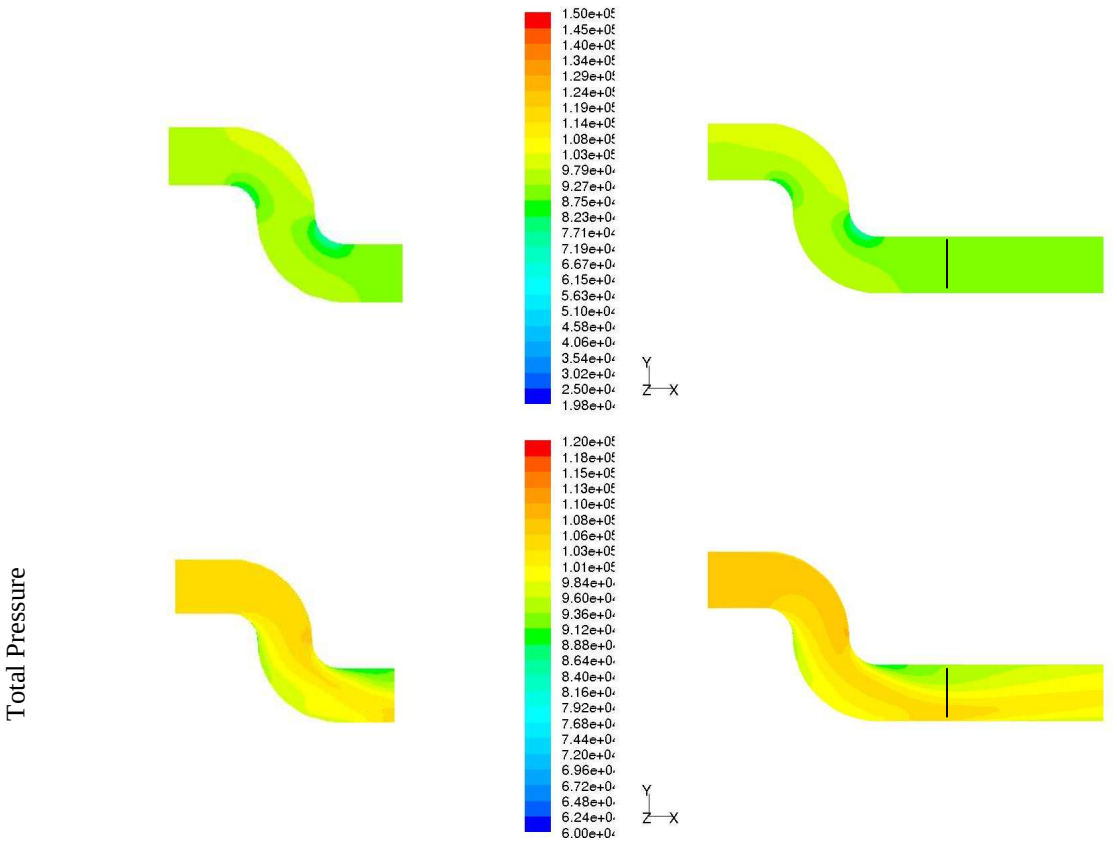

(a) Short Duct (b) Extended Duct

Figure 4-17: Total (Pa) and Static Pressure (Pa) Contour Plots for the (a) Short S-Duct and (b) Extended S-Duct

In both cases, static pressure seems to be nearly constant at the AIP (indicated by the dashed line in extended duct) at approximately 90 kPa. Yet, there are some clear differences between the two solutions. Some evident differences are that the pressure contours in the two analyses are shifted in certain locations, especially in the turning region, and the extended duct case solves for a higher total pressure at the inlet of the system than the short duct case. Other flow variable profiles indicate consistent differences between the two cases. The inclusion of the injectors in the duct adds another level of uncertainty to the static pressure profile AIP. Therefore, the extended duct geometry was chosen to analyze the serpentine duct flow injection problem, rather than the short duct.

The extended S-duct with no flow injection served as a baseline of comparison for the flow injection cases. With serpentine duct geometry adequately meshed and boundary and initial conditions applied, the CFD code was iterated to solve for a steady solution to each problem. The results for the no injection case are presented below.

No Injection, Serpentine Duct

Figure 4-18 show the total temperature side centerline profile and AIP plane. As expected, there is no large change in total temperature because there is no thermal driver present. There is a very small change in total temperature distortion due to separated and turbulent flow regions. The AIP results show that there is no major total temperature distortion content (only a 0.681% distortion in total temperature).

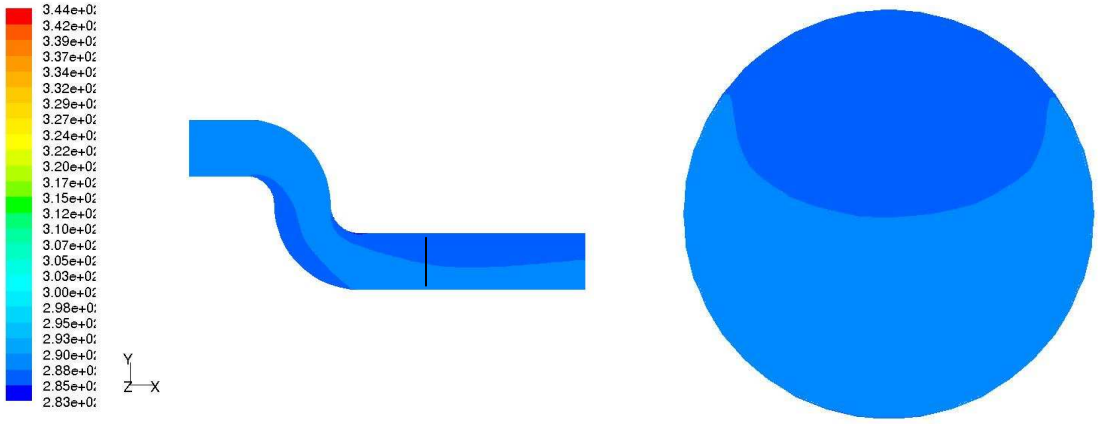

(a) Centerline Side View (b) AIP Cross-section

Figure 4-18: Total temperature (K) contours (serpentine duct, no injection)

Examining the total pressure profiles, there are evident total pressure losses encountered in the first and second turns of the S-Duct (Figure 4-19). The total pressure drops at the inner radius turns in the duct, with a more severe drop located at the second turn. The AIP shows a low pressure region at the top of the duct that covers approximately 60 degrees of the duct circumference. A higher total pressure region can be seen at the lower portion of the duct. The incorporation of a flow injector in the duct, which was placed on the inner radius of the second turn (see following sections), will energize the flow such that the total pressure at the top of the duct will be higher. A total pressure distortion of 12.47% is present at the AIP.

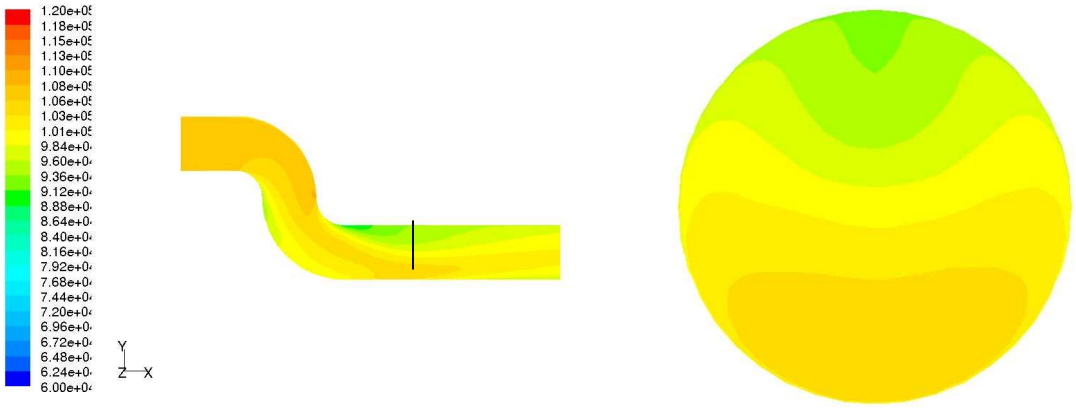

(a) Centerline Side View (b) AIP Cross-section

Figure 4-19: Total Pressure (Pa) contours (serpentine duct, no injection)

The static pressure in the duct drops in the turning regions, but recovers very quickly. The AIP pressure profile is quite uniform (Figure 4-20). The pressure at this plane varies less than 1.17% from the average pressure of 90.8 kPa.

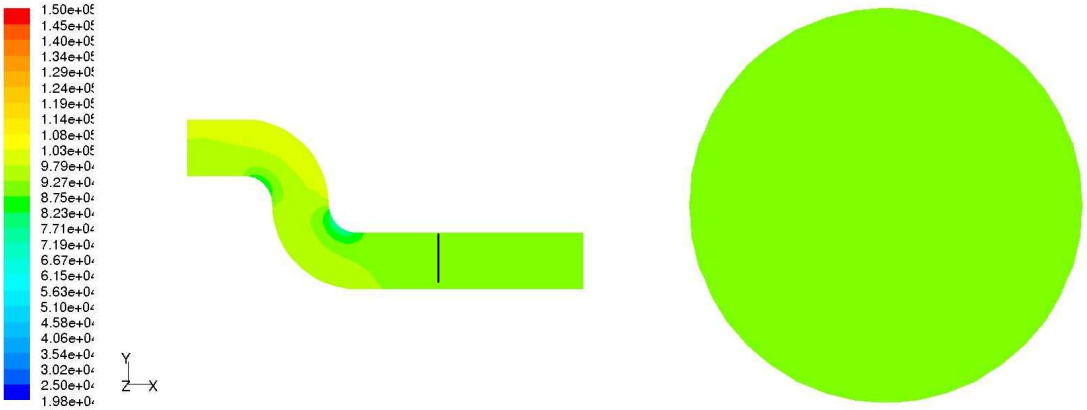

(a) Centerline Side View (b) AIP Cross-section

Figure 4-20: Static Pressure (Pa) contours (serpentine duct, no injection)

The Mach number contour plots can be seen in Figure 4-21. The large blue region on the outside radius of the second turn indicates a separated flow region caused by the first 90^{o} bend. The flow reattaches after the second turn to the lower wall. Following the two 90^{o} bends, the flow continues to have a lower Mach number at the top of the duct. The AIP contour plot clearly shows a low Mach number region extending about 120 degrees of the duct circumference, and the lowest Mach number region (dark

blue) covers a radial incursion of approximately 30%. The Mach number distortion at the AIP was 79.4%.

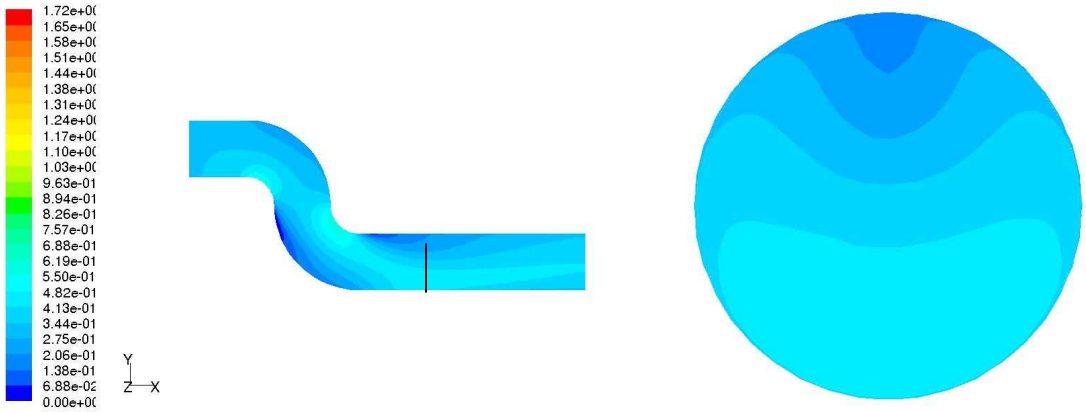

(a) Centerline Side View (b) AIP Cross-section

Figure 4-21: Mach number contours (serpentine duct, no injection)

Similarly, the velocity magnitude in the duct shows the same separated flow region caused by the severe first turn (Figure 4-22). This is consistent for all of the serpentine cases, assumed solely due to the duct geometry. The velocity magnitude plot presents a low velocity region in the duct. This is most likely due to the secondary flow vortices that are generated from the second downstream turn. Similar to the Mach number distortion, the velocity magnitude distortion at the AIP location has a large distortion of 78.5%.

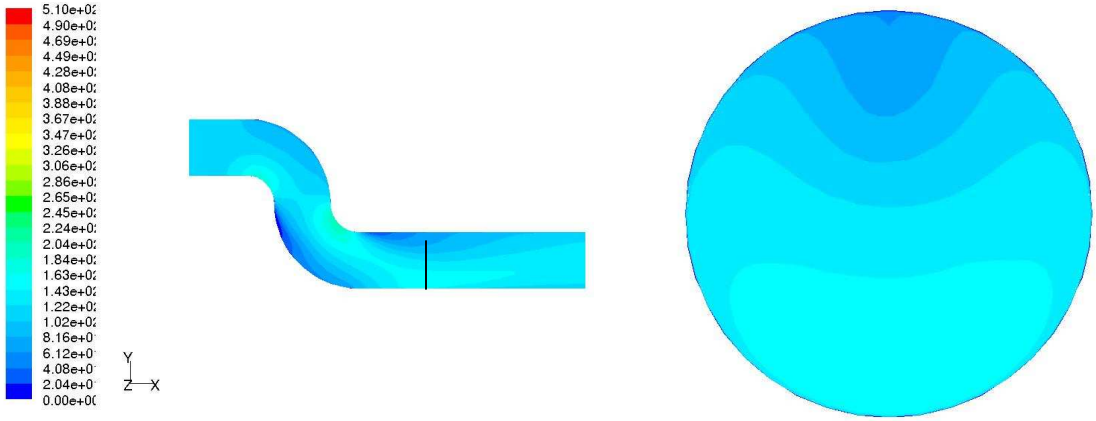

(a) Centerline Side View (b) AIP Cross-section

Figure 4-22: Velocity Magnitude (m/s) contours (serpentine duct, no injection)

Cold Injection, Serpentine Duct

Flow injected at the same total temperature as the core flow would produce no significant total temperature variation in the flow. This is evident in Figure 4-23. There is a slightly lower total temperature region in the turning region and high turbulence regions, as noted in the no-injection case (0.408% distortion).

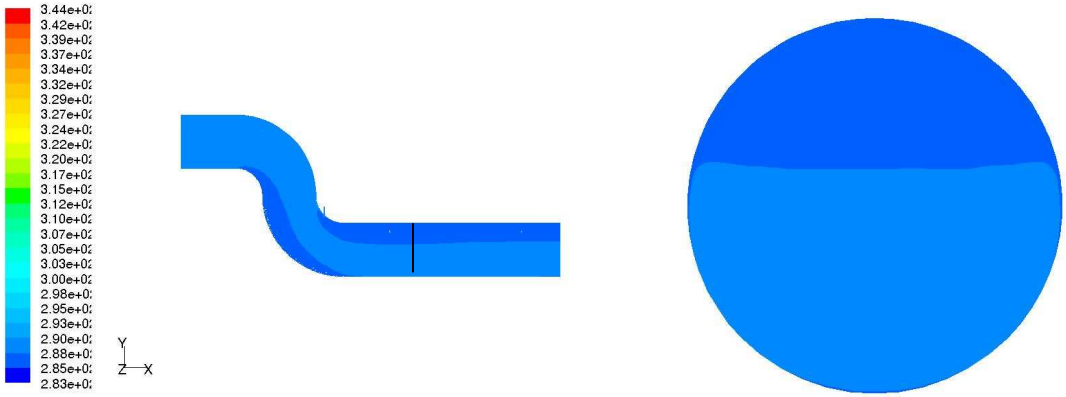

(a) Centerline Side View (b) AIP Cross-section

Figure 4-23: Total temperature (K) contours (serpentine duct, cold injection)

The total pressure contours with cold flow injection are much more vivid in the serpentine duct. A low total pressure region can be seen at the top of the duct (Figure 4-24). This region is much smaller than the serpentine duct with no flow injection case because the injected flow enters the core flow at a higher total pressure, which helps to reduce the total pressure distortion at the AIP from 12.4% (no injection) to 9.2%.

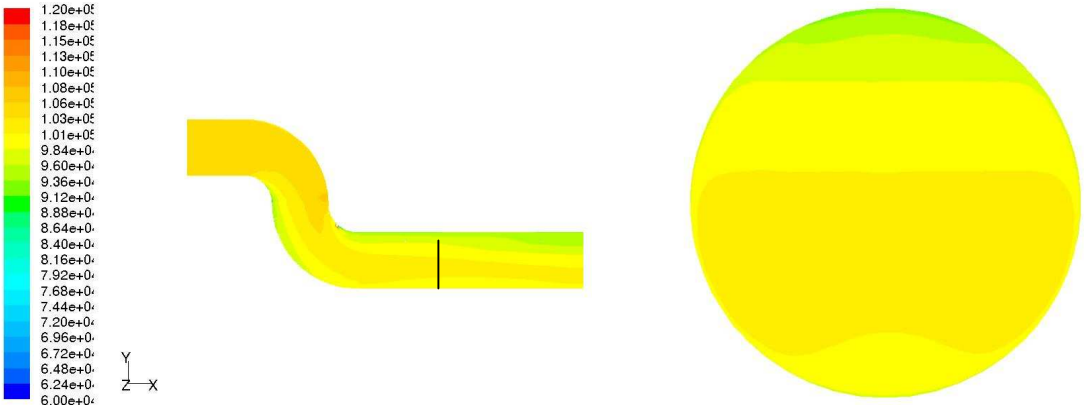

(a) Centerline Side View (b) AIP Cross-section

Figure 4-24: Total pressure (Pa) contours (serpentine duct, cold injection)

The static pressure profile at the AIP is uniform (Figure 4-25) with a negligible distortion of 0.396 %. This result indicates that static pressure recovers faster than the other flow variables downstream of the injectors. The addition of the injected flow reduced the static pressure distortion to 0.774 % at the AIP from the no injection case of 1.17 % static pressure distortion.

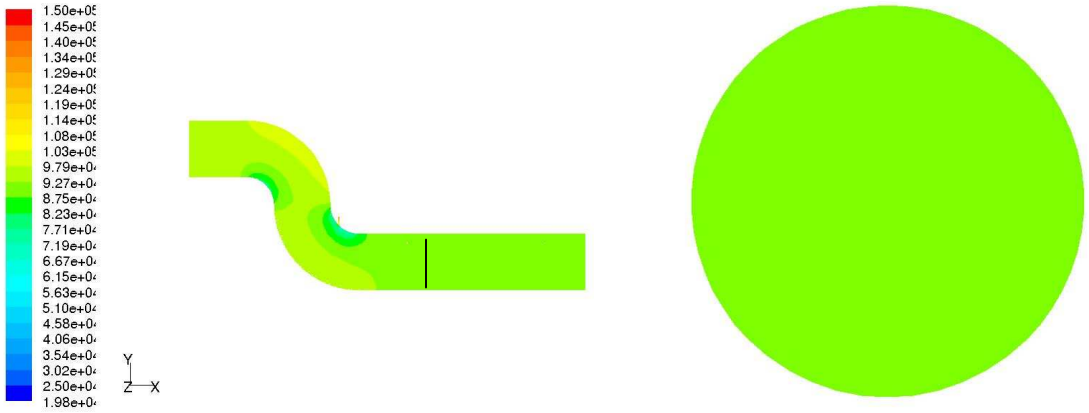

(a) Centerline Side View (b) AIP Cross-section

Figure 4-25: Static pressure (Pa) contours (serpentine duct, cold injection)

The Mach number contours (Figure 4-26) are quite different from the no injection case. The addition of the high total pressure flow benefits the Mach number distribution at the AIP, albeit with a 64% distortion is present. The low Mach number region is constrained to the top of the duct, making the majority of the profile much more uniform than with no injection.

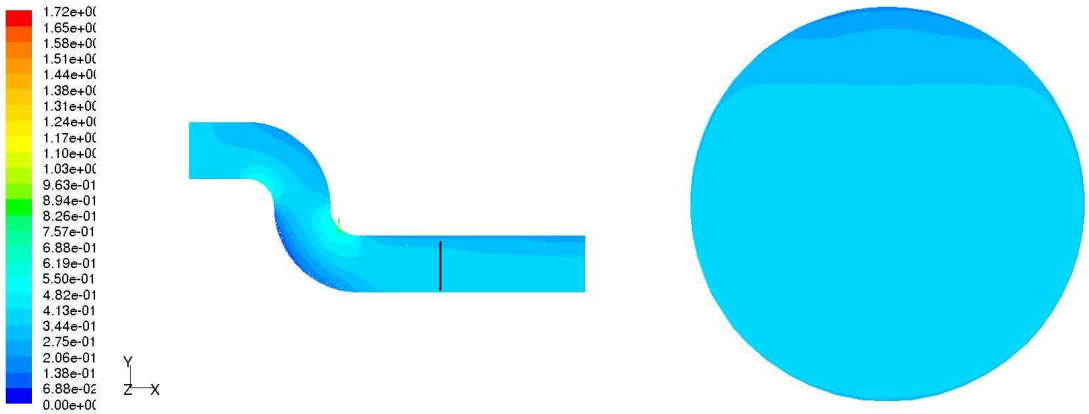

(a) Centerline Side View (b) AIP Cross-section

Figure 4-26: Mach number contours (serpentine duct, cold injection)

The velocity magnitude shows similar characteristics as the Mach number variation. The low velocity region is held to the top of the duct and does not protrude excessively radially into the duct (Figure 4-27). A main difference with the no-injection case is the lack of secondary flow evidence in the velocity profile. The orientation of the jets (which covered approximately a 60^o circumference at the top of the duct) seems to have attenuated the effects of the duct turning-induced vortices. Again, this is also seen in the total pressure and Mach number AIP profiles. The velocity distortion at the AIP is 63.4 % in this case.

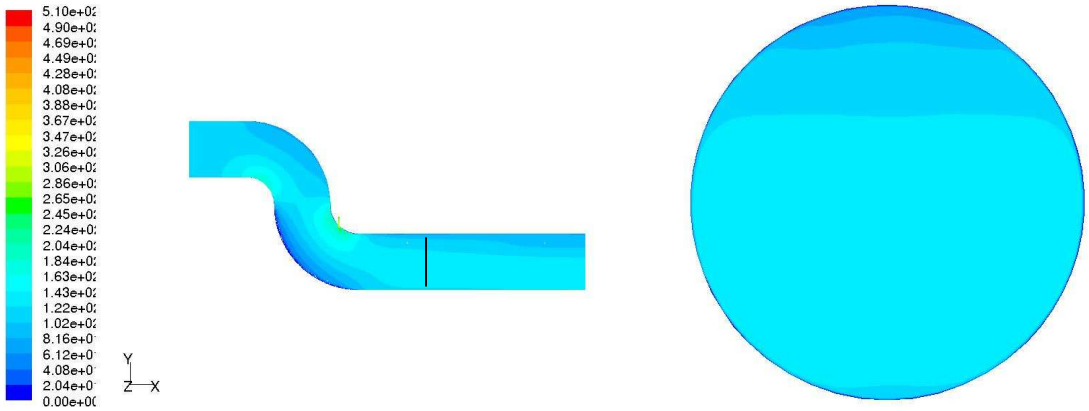

(a) Centerline Side View (b) AIP Cross-section

Figure 4-27: Velocity magnitude (m/s) contours (serpentine duct, cold injection)

Hot Injection, Serpentine Duct

Flow injected at a temperature of 100 R (~55 K) above the core temperature creates a substantial temperature distortion. The light blue color indicates a high total temperature region held to the top of the duct, as seen in Figure 4-28. Since only 2% of the core mass flow is being injected, the hot flow diffuses to a temperature of 302 K, which is approximately 14 K (25 R) above the core temperature. The AIP contour plot indicates that the hot injected flow covers approximately 60 degrees of the duct circumference and has a radial incursion of approximately 15% in the duct. The thermal distortion, though diffusing, persists to the exit of the computational domain. The AIP total temperature distortion equates to 4.09%, which is lower than the total temperature distortion present at the AIP of the straight duct, hot flow injection case. Enhanced flow mixing due to the serpentine duct geometry is the factor which induces less total temperature distortion (due to more temperature diffusion).

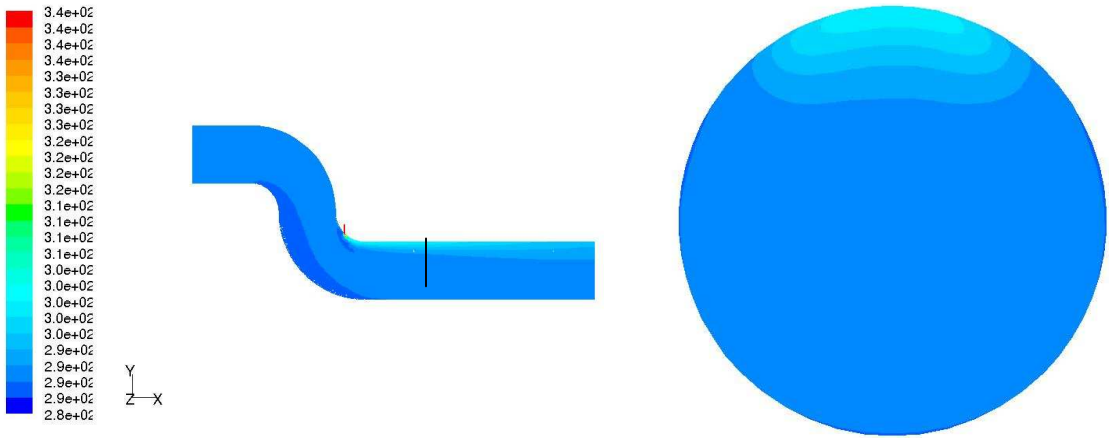

(a) Centerline Side View (b) AIP Cross-section

Figure 4-28: Total temperature (K) contours (serpentine duct, hot injection)

The injection of high total pressure flow (at nearly twice the inlet P_T) into the duct was beneficial for the total pressure profile at the AIP (Figure 4-29). The injection "reenergizes" the flow at the top of the duct, reducing the low total pressure region found in Figure 4-19 (no injection, serpentine duct total pressure profile). Similar to the cold injection case, the AIP profile has a larger high total pressure region than the no injection case. This profile interacting with a compressor has the potential to attenuate unsteady

blade loading, as compared to the no injection case. The total pressure distortion of 9.6% is slightly higher than for the cold injection case.

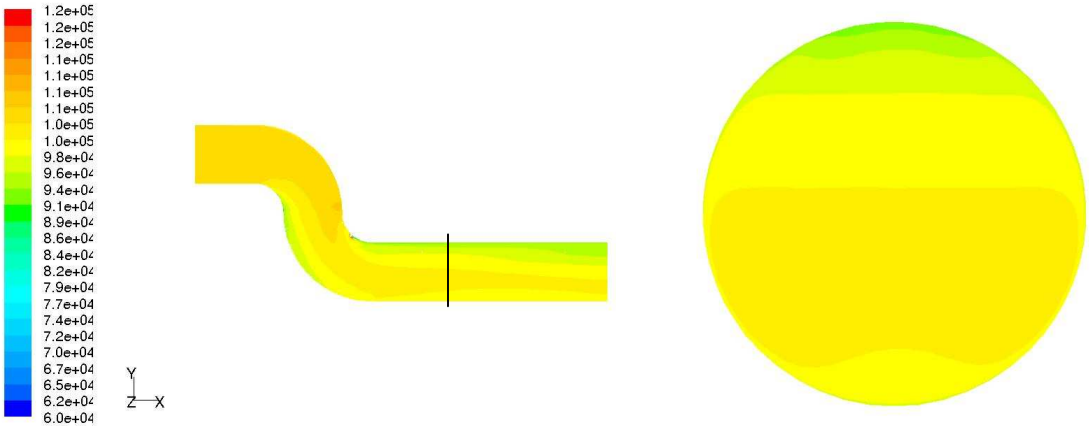

(a) Centerline Side View (b) AIP Cross-section

Figure 4-29: Total pressure (Pa) contours (serpentine duct, hot injection)

The static pressure contours are shown in Figure 4-30. Static pressure in the injector is higher than that of the core flow. When entering the core flow, the injected flow pressure drops dramatically due to a shocks and diffusion at the injector exit (or throat). The AIP static pressure profile is uniform, as expected, with a 0.389% distortion.

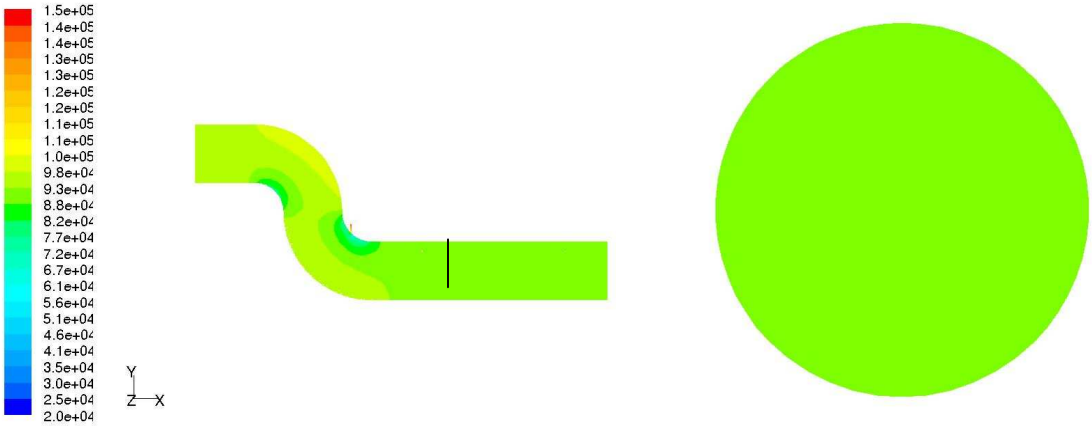

(a) Centerline Side View (b) AIP Cross-section

Figure 4-30: Static pressure (Pa) contours (serpentine duct, hot injection)

The Mach number at the injector exit appears to be sonic, or choked (M = 1). The separated flow regions evident in the no-injection case are still present in this hot injection case. Yet, due to the injection of the high total pressure, the low Mach number region is confined to a smaller area at the top of the duct in the AIP (Figure 4-31). The Mach number distortion in hot injection case (68.2%) is somewhat larger than for cold flow injection case (64%).

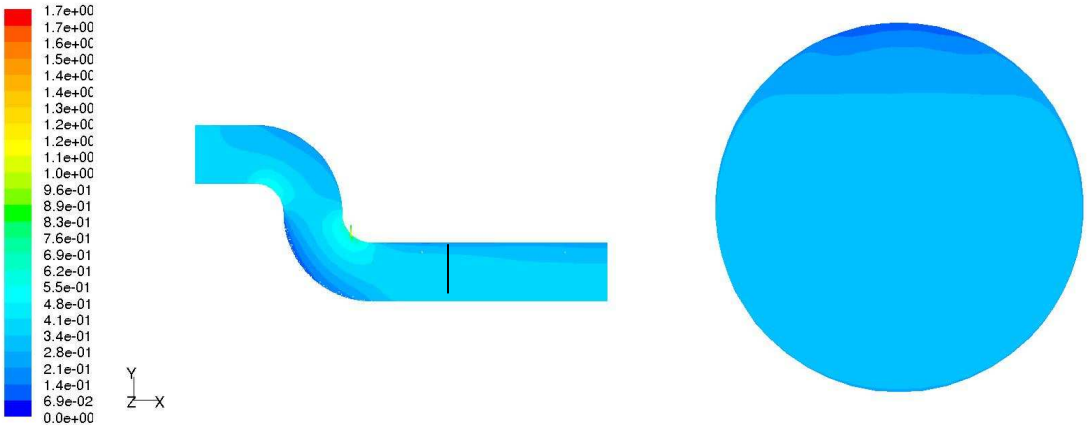

(a) Centerline Side View (b) AIP Cross-section

Figure 4-31: Mach number contours (serpentine duct, hot injection)

The velocity magnitude of the flow looks quite similar to that of the no-injection case. Figure 4-32 displays the velocity magnitude contour plots for the hot flow injection case. The main difference between the two analyses can be seen in the AIP contour plot. There is a lower velocity region at the top of the duct than for the no-injection case. This is due to the fact that the injected flow introduces turbulence to the flow, which reduces the flow velocity. The distortion of velocity at the AIP is approximately 66.7%.

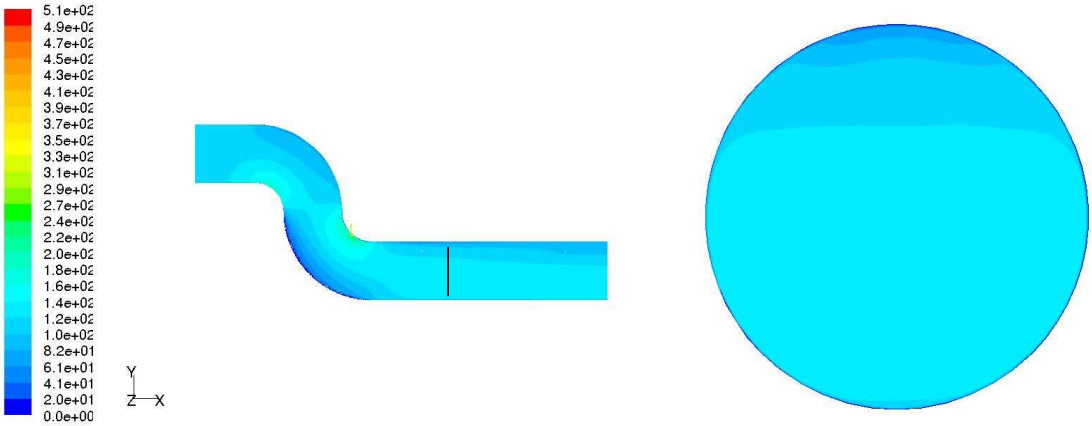

(a) Centerline Side View (b) AIP Cross-section

Figure 4-32: Velocity magnitude (m/s) contours (serpentine duct, hot injection)

4.3 AIP Distortion Comparison

A distortion magnitude was used to compare the thermal source and flow injection AIP distortion levels analyses to one another. This equation (4-1) is presented in Section 4.2. The chart below indicates the amount of distortion at the AIP for each evaluated case and relevant variable (Figure 4-33). Note that the index does not represent the distorted amount of coverage area or maximum and minimum magnitude values. This maximum, minimum, and average variable information is tabulated in Appendix A.

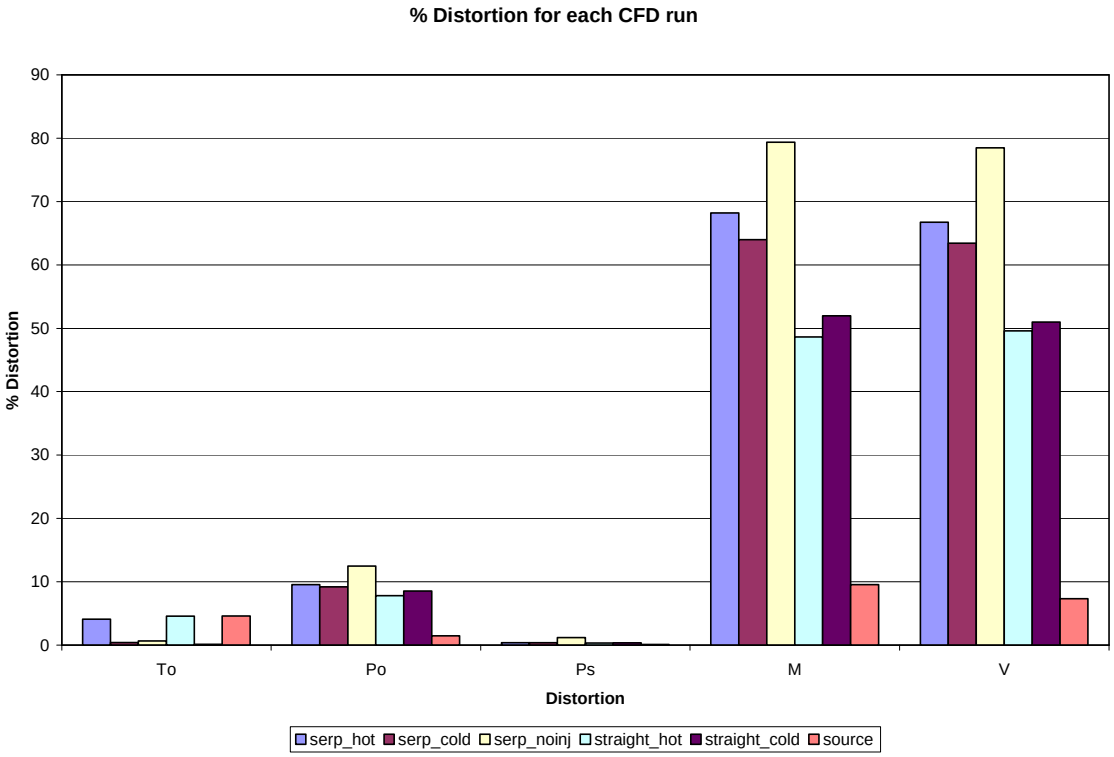

Figure 4-33: Distortion Comparison at AIP

This information was gathered from the AIP contour plots presented in the previous results sections. Shown are the distortion levels for each of the six CFD runs, grouped in flow variables (T_T, P_T, P_s, Mach number, and velocity magnitude).

The straight duct, 3/rev thermal source investigation generated a total temperature distortion of 4.58%. This value is similar in magnitude to the straight and serpentine duct, hot flow injection cases (4.09% and 4.56%, respectively). The static pressure

distortion generated from the thermal source is negligible. The total pressure, Mach number, and velocity magnitude distortions are quite different from the flow injection analyses. The distortions generated from the thermal source are nominally $1/5^{th}$ the respective flow variable amount as the flow injection cases.

The straight duct with hot flow injection can effectively produce a thermal distortion. The flow introduced from the injector at a temperature 100 R higher than the core flow resulted in a 4.09% thermal distortion at the AIP. With the same temperature flow injection (ΔT_T = 0 R), no variation in total pressure distortion was experienced. Static pressure at the AIP was not affected by the introduction of the hot or cold flow. The total pressure, Mach number, and velocity magnitude distortions were slightly lower for the hot flow injection analysis.

The serpentine duct investigation yielded intriguing results as well. With no flow injection present, no total temperature distortion was noticeable, yet total pressure distortion and large Mach number and velocity magnitude distortions were seen. The geometry of the duct, clearly, can cause adverse effects on the performance of an inlet.

The addition of the flow injectors at the downstream location was quite beneficial, whereby the total pressure distortion profile was attenuated. Injecting the same temperature air as the core flow temperature significantly dropped the total pressure, Mach number, and velocity distortion levels. Unlike the straight duct hot injection case, the serpentine duct with hot injection, though aiding in reducing the total pressure distortion levels from the serpentine duct, no injection case, did not decrease the distortion level as much as the cold injection.

The flow injection with thermal distortion not only applied thermal energy to the core flow, but momentum energy as well. High total pressure and velocity air was injected which affected the core flow and the AIP profile. To isolate the effects of the total temperature distortion at the AIP, isentropic calculations were implemented.

4.4 Isentropic calculations

The effects due to the total temperature distortion are evaluated using the isentropic flow equation (4-2)[2]. By evaluating the flow profile at the AIP of the hot and cold flow cases for a flow injection analysis, an assumed amount of total pressure distortion will yield the Mach number and velocity variation. The static pressure at the AIP was assumed constant in these calculations. The Mach number is determined by equation 4-2.

$$\frac{P_o}{P} = \left(\frac{T_o}{T}\right)^{\frac{\gamma}{\gamma-1}} = \left(1 + \frac{\gamma-1}{2} M^2\right)^{\frac{\gamma}{\gamma-1}} \qquad \textbf{4-2}$$

The velocity is determined from the definition of the Mach number (for a perfect gas), as shown in equation 4-3.

$$M = \frac{V}{\sqrt{\gamma RT}} \qquad \textbf{4-3}$$

The isentropic calculations of distortion at the AIP are presented in Table 4-1. The total pressure distortion was on the order of 10% for the flow injection CFD analyses. Therefore, high and low total pressure values were selected that resulted in a 10% distortion. A uniform static pressure at the AIP was assumed as well. According to the isentropic analysis, for the cold injection case, the Mach number and velocity vary on the order of 60%. The isentropic analysis with a 4.6% thermal distortion (hot injection case) at the AIP results in a slightly higher amount of velocity distortion. The Mach number does not change for this case because the total pressure and static pressure are the same as the cold injection isentropic analysis.

[2] This equation is derived from the Second Law of Thermodynamics, assuming that there is no change in Entropy.

Table 4-1: Isentropic calculations of Mach number and Velocity

	Variables	High	Low	% Dis = (High - Low)/High
Cold Injection (Δ To = 0 R = 0 K)	Po (Pa)	101900	91700	10.010
	P (Pa)	90000	90000	0.000
	To (K)	288	288	0.000
	M	0.424956	0.163719	61.474
	V (m/s)	142.0173	55.5444	60.889
	Variables	**High**	**Low**	**% Dis = (High - Low)/High**
Hot Injection (Δ To = 25 R = 14 K)	Po	101900	91700	10.010
	P	90000	90000	0.000
	To (K)	302	288	4.636
	M	0.424956	0.163719	61.474
	V	145.4281	55.5444	61.806

In comparison to the results of the flow injection CFD analyses, the results of the isentropic calculations qualitatively match in that Mach number and velocity distortion dominates the distortion at the AIP. By holding the total temperature distortion constant (cold injection case), the Mach number and velocity distortion is shown to be predominately affected by the presence of a total pressure distortion. The addition of a thermal distortion (hot injection case) produces a higher amount of velocity distortion at the AIP. These isentropic calculation results are consistent with the serpentine duct injection analyses. However, the isentropic calculation results differ from the straight duct flow injection analysis results, where more velocity distortion is produced by injecting cold flow rather than hot flow.

Qualitatively, the results presented from the isentropic calculations indicate that the majority of the Mach number and velocity distortions are generated by the high variation in total pressure. The Mach number and velocity are quite comparable to one another in distortion magnitude. This is because the velocity is linearly proportional to the Mach number, as presented in Equation 4-3.

5 Conclusions

The boundary conditions generated at the AIP due to thermal distortion entering an aircraft compression system were investigated. Two means of generating thermal distortions were implemented using a three-dimensional CFD program. A thermal source and a flow injection method were modeled in straight inlet ducts. The flow injection method was also modeled in a serpentine duct. Both methods produced significant total temperature variation at the AIP and also influenced other flow variable patterns due to the thermal distortion.

The thermal source analysis implemented a volumetric thermal heating source to create the desired total temperature distortion. This CFD modeling approach was useful in modeling the effects of only due to thermal distortion and without physical obstruction (which creates total pressure loss) in the flow path. Exit profiles of total temperature, total pressure, Mach number and velocity have been identified. Static pressure was constrained constant at the exit profile, corresponding to the results presented in the Braithwaite, et al. (1973) paper. A total temperature magnitude extent of 25 R corresponds with the extent evaluated by Kenyon, et al., with slight variations in circumferential and radial variables in the AIP profile. The AIP total pressure profile has an approximate peak-to-peak total pressure variation of ±0.75 kPa. The AIP total pressure profile has magnitudes within 2% of its maximum extent, while the velocity profile has magnitudes within 8% of its respective extent.

A flow injection investigation was implemented to serve as a practical approach to introducing thermal distortions to the flow such that boundary conditions at the AIP could be obtained. A straight duct was computationally modeled with a set of flow injectors in a representative flow control configuration in the inlet of aircraft engines. In addition, a serpentine duct was analyzed to evaluate the boundary conditions at the AIP due to geometric effects and flow injection at a specified location.

In the straight duct analysis, injecting hot air introduced less total pressure, Mach number, and velocity distortion to the flow than the cold air injection. However, in the serpentine duct case, the injection of cold air was more beneficial in lowering distortion level for the total pressure, Mach number, and velocity than the hot air injection. Both the straight and serpentine flow injection models indicate that generating a thermal distortion through flow injection varies the velocity magnitude and Mach number far more than the total pressure and temperature. As highlighted in Appendix A, the flow injection velocity and Mach number distortion values are more than five-times that of any other flow variable. For the hot injection cases, the total temperature distortion is on the order of 4%. Velocity and Mach number distortion for the injection cases is on the order of 50%-65%, while total pressure distortion is on the order of 10%. These results have similar trends to that of the pure thermal source investigation. Due to a thermal distortion, the thermal source case creates more velocity distortion (8%) than the total pressure distortion (2%). A similar total temperature distortion is experienced as well. The main driver for the velocity and Mach number distortion, however, is the total pressure distortion, not the variation in total temperature.

Injection of high total pressure air in the serpentine duct proved affective at reducing distortion levels at the AIP. Injecting at different locations in the duct may further improve the pressure recovery and flow uniformity at the AIP. Based on duct geometry, a number of flow injector locations and orientations can be investigated. The optimization of these injectors would be beneficial to the aerodynamic design engineer.

Qualitatively, the results from the two modeling approaches indicate that the AIP profile is more likely to have a constant total pressure profile rather than a uniform velocity profile. The percentage of velocity distortion is ranges from 5 to 11 times greater than the total pressure distortion for each CFD case investigated. These data give confidence to the fact that total temperature distortions create higher levels of velocity and Mach number distortion than total pressure distortion.

The thermal heating approach is not a practical method of creating thermal distortions in aircraft inlets. Therefore, questions as to the legitimacy of the "real-world" application of the study arise. The distorted flow profiles created by the thermal distortion may occur due to ingestion of hot gas hydrogen burners, for example, yet a volumetric heat source in an operational aircraft's inlet is not feasible thermal distortion generation technique.

The flow injection model seems to be a far more robust modeling method than the thermal source. Seeing that the thermal source is a mathematical idealization rather than a feasible occurrence in an aircraft engine inlet, the confidence in the modeling a thermal distortion with a flow injection methodology is stronger. Flow injection can be implemented experimentally, as well. The two thermal distortion generation techniques inherently have different effects on the flow. The thermal source analysis affects the thermal energy in the flow. The flow injection method not only affects the thermal energy, but the momentum energy as well.

The distortion magnitudes vary between all cases studied. Both the thermal source and flow injection analyses indicate that under the influence of a thermal distortion, total pressure distortion is much less than the velocity distortion in all cases. An important conclusion is that boundary conditions at the AIP can be assumed to have a constant pressure profile. Due to the high dependency on total pressure, the Mach number and velocity profile should be calculated from the total pressure, not assumed. The thermal source analysis indicates that assuming a uniform total pressure profile for small thermal distortions can be an appropriate assumption for the AIP boundary condition.

The uniform total pressure boundary condition used in the Kenyon, et al. analysis was appropriate for a thermal distortion analogous to a thermal source distortion. This instills confidence to the results in the Kenyon, et al. analysis, which indicates that thermal distortions can induce high unsteady blade loading. The constant circumferential velocity boundary conditions in the Kenyon analysis do not correlate well with the results in the thermal source investigation. Velocity boundary conditions should be avoided when dealing with thermal distortion investigations.

The addition of flow injectors in the serpentine duct was beneficial in reducing the total pressure distortion. The distortion in some case reduces on the order of 30%. This value may be further reduced with optimization of the flow injectors. The total pressure distortion at the AIP due to the flow injection method indicates a higher level of distortion that the thermal source case. Depending on the orientation of the injectors, an estimation of the total pressure profile may be appropriate. However, a computational analysis involving an inlet incorporated with a fan model would hold more fidelity than assuming AIP boundary conditions.

6 Recommendations

The following list identifies the recommendations for future studies involving thermal distortion generation and application.

1. The two distortion generation techniques used in this analysis provided insight regarding the flow profiles (and generalized boundary conditions) experienced by a compression system. As stated in the conclusion, the thermal source method is not a practical means of creating thermal distortions in aircraft engine operation. Though mathematically sound, future work involving computational thermal distortion analysis should focus on flow injection and other means of thermal distortion that may be used in practice and experimentation (burners, for instance).

2. Since thermal distortions are probable events in aircraft engine inlets, thermal distortion experimentation is a critical aspect to the design of the inlet/engine system. Total pressure distortions have been extensively investigated in the past and have shown to have a negative impact on performance, operability, and aeromechanics. However, effects of thermal distortions on a compression system have not been investigated as much. Previous research found in the literature reveals that thermal distortion has a negative performance and operability effects on a compressor, yet there is little information on aeromechanical effects of inlet thermal distortion on compressor blades. More attention should be paid to the aerodynamic and vibratory effects of thermal distortion on a compressor.

3. The effects of a thermal distortion on a flow field and on a fan/compressor rotor of modern design should be experimentally measured. Both straight and curved inlets should be evaluated. The tests must adequately capture essential flow field variables, such as static pressure, total pressure, velocity, Mach number, and total temperature. Instrumentation on the rotor should capture on blade surface pressures as well as stress measurements. An understanding of the vibratory

response of the rotor under the influence of a thermally-distorted profile should be investigated.

4. An investigation should be carried out similar to the study implemented by Kenyon et al. (2004). Boundary conditions of constant static pressure, varying total pressure, and varying velocity should be applied as the inlet boundary condition to the model. This will provide a better computational understanding to the effects of a thermal distortion on unsteady blade loading.

5. In the analyses presented in this report, no fan or compressor was modeled downstream of the AIP. The interaction with the fan flow will affect the upstream calculations at the AIP location. It is suggested that the entire inlet and fan assembly be analyzed together such that a further understanding of compression system inlet boundary conditions and response.

6. An interesting and worthwhile analysis that should be implemented in future distortion response testing is to evaluate the unsteady aerodynamic and aeromechanical effects of flow variables in phase and out of phase with one another. For example, combined high total temperature and high total pressure applied to the same spatial area may have a larger performance drop and vibratory response rather than having the flow variables out of phase. The phase relationships of total temperature, total pressure, Mach number, and velocity should be investigated.

7. The straight and serpentine flow injection models incorporated three additional duct lengths after the AIP, such that an exit static pressure profile could be assumed. It would be worthwhile to investigate whether the flow profile at the AIP changes if even more duct lengths are added to the exit of the computational domain.

8. Meshing the interface between the core duct and the injectors gives little control to the user. The mesher uses tetrahedral elements and automates the meshing process. One means of simplifying the injection model (with respect to meshing the geometries) is to use “non-conformal meshing.” This method gives the user the ability to mesh the core duct and injectors completely independent of one another. The interface of the injector and the core wall interpolates the transfer of fluid variables. The advantage of this is that it reduces the effort involved in the meshing process. The downside is that it may result in a less accurate analysis. With an adequate mesh though, this method should work affectively.

References

Amundson, M. H., and Holm, R. G., "Distortion Test Capabilities for Future Fighter Aircraft Engines," 25th AIAA/ASME/SAE/ASEE Joint Propulsion Conference, Monterey, CA, July 10-12, 1989, AIAA-89-2956.

Bauermeister, W. K., Roseburg, C. M., and Ip, H. W., "727 Airplane Engine Inlet Development," AIAA 4th Propulsion Joint Specialist Conference, June 10-14, 1968, Cleveland, OH, AIAA 68-595.

Blazek, J., Computational Fluid Dynamics: Principles and Applications, 1st Edition, Elsevier, 2001.

Braithewaite, W.M., Graber Jr., E.J., and Mehalic, C.M., "The Effect of Inlet Temperature and Pressure distortion on Turbojet Performance," AIAA/SAE 9th Propulsion Conference, Las Vegas, NV, November 5-7, 1973.

Braithwaite, W. M., and Soeder, R. H., "Combined Pressure and Temperature Distortion Effects on Internal Flow of a Turbofan Engine," 15th AIAA/SAE/ASME Joint Propulsion Conference, 18-20 June, 1979, Las Vegas, NV (79-1309).

Bullock, R. O., Design and Development of Aircraft Propulsion Systems, Aircraft Propulsion Systems Technology and Design, edited by G. C. Oates, AIAA Education Series, Washington, D.C., 1989, pp. 59-61.

Danforth, C. E., "Distortion-Induced Vibration in Fan and Compressor Blading," J. Aircraft, Vol. 14, No. 4, Pg. 216-225.

DiPietro Jr., A. L., Design and Experimental Evaluation of a Dynamics Thermal Distortion Generator for Turbomachinery Research. Masters Thesis in Aerospace

Engineering, Virginia Polytechnic Institute and State University, Blacksburg, VA, April, 1993.

DiPietro Jr., A. L., Effects of Temperature Transients on the Stall and Stall Recovery Aerodynamics of a Multi-stage Axial Flow Compressor (A New Technique for Active Recovery from Rotating Stall. Doctor of Philosophy in Mechanical Engineering, Virginia Polytechnic Institute and State University, Blacksburg, VA., February, 1997.

EL-Aini, Y., deLaneurine, R., Stoner, A., and Capece, V., "High Cycle Fatigue of Turbomachinery Components – Industry Perspective," AIAA 1997.

Ferziger, J. H., and Perić, M., Computational Methods for Fluid Dynamics, 3rd Edition, Springer-Verlag, 2002.

FLUENT 6.2 User's Guide: http://www.fluentusers.com/fluent/doc/doc_f.htm, January 2005.

Fulghum, D. A., and Barrie, D. "The Future of Stealth," Aviation Week and Space Technology, April 4, 2005, Vol. 162, No. 14, pp. 24-25.

GAMBIT 2.2 Documentation: http://www.FLUENTusers.com/gambit/doc/doc_f.htm, July 2004.

Hamed, A. and Numbers, K., "Inlet Distortion Considerations for High Cycle Fatigue in Gas Turbine Engines," 33rd AIAA/ASME/SAE/ASEE Joint Propulsion Conference & Exhibit, July 6-9, 1997, Seattle, WA, AIAA 97-3364.

Hill, P., and Peterson, C., Mechanics and Thermodynamics of Propulsion. Second Edition, 1992, Addison-Wesley Publishing Company, Inc.

Kenyon, J. A., Rabe, D. C., and Hah, C., "Inlet Temperature Distortion Effects on Unsteady Blade Loading in a Transonic," 9th National Turbine Engine High Cycle Fatigue (HCF) Conference, 16-19 March, 2004, Pinehurst, NC.

Kenyon, J. A., Rabe, D. C., and Fleeter, S., "Aerodynamic Effects on Blade Vibratory Stress Variations," Journal of Propulsion and Power, Vol. 15, No. 5, September-October 1999, Pg. 675-680.

Kimzey, W.F. "An Analysis of the Influence of Some External Disturbances on the Aerodynamic Stability of Turbine Engine Axial Flow Fans and Compressors." AEDC TR-77-80, August 1977.

Manwaring, S. R., Rabe, D. C., Lorence, C. B., and Wadia, A. R., "Inlet Distortion Generated Forced Response of a Low-Aspect-Ratio Transonic Fan," Journal of Turbomachinery, October 1997, Vol. 119, Pg. 665-676.

Manwaring, S. R., and Fleeter, S., "Forcing Function Effects on Rotor Periodic Aerodynamic Response," Presented at the Gas Turbine and Aeroengine Congress and Exhibition, Jun 11-14, 1990, Brussels, Belgium, 90-GT-109.

Rabe, D., Bolcs, A., and Russler, P., "Influence of Inlet Distortion on Transonic Compressor Blade Loading," 31st AIAA/ASME/SAE/ASEE Joint Propulsion Conference and Exhibit, July 10-12, 1995, San Diego, CA, AIAA 95-2461.

Rudey, R.A. and Antl, R.J., "The Effect of Inlet Temperature Distortion on the Performance of a Turbo-Fan Engine Compressor System," AIAA 6th Propulsion Joint Specialist Conference, San Diego, California, June 15-19, 1970, AIAA-70-625.

SAE Aerospace Resource Document (ARD50015), "A Current Assessment of the Inlet/Engine Temperature Distortion Problem." Copyright 1991, Society of Automotive Engineers, Inc., 400 Commonwealth Drive, Warrendale, PA 15096-0001. Issued 1991-01-22.

Saravanamuttoo, H., Rogers, G., and Cohen, H., Gas Turbine Theory, 5th Edition, Prentice Hall, 1991, pg. 211.

Seddon, J.J., and Goldsmith, E.L., Intake Aerodynamics, AIAA Education Series, 2nd Edition, 1999, pg. 84.

Society of Automotive Engineers Aerospace Information Report, AIR 1419, "Inlet Total-Pressure-Distortion Considerations for Gas Turbine Engines," Society of Automotive Engineers, Warrendale, PA, May 1983.

Society of Automotive Engineers Aerospace Recommended Practice, ARP 1420, "Gas Turbine Engine Inlet Flow Distortion Guidelines," March 1978.

Stanitz, J.D., W.M. Osborn, and J. Mizisin, "An Experimental Investigation of Secondary Flow in an Accelerating, Rectangular Elbow," NACA TN-3015, October 1953.

Suder, K. L., Thorp, S. A., Strazisar, A. J., Bright, M. B., and Hathaway, M. D., "Compressor Stability Enhancement Using Discrete Tip Injection," ASME Turbo Expo 2000, May 8-11, 2000, Munich, Germany, 2000-GT-0650.

Wallace, R. M., King, P. S., Kenyon, J. A., and O'Brien, W. F., "Modal Response of a Transonic Fan Blade to Periodic Inlet Pressure Distortion," 9th National Turbine Engine High Cycle Fatigue (HCF) Conference, 16-19 March, 2004, Pinehurst, NC.

Walter, W. A., and Shaw, M., "Predicted F100 Engine response to Circumferential Pressure and Temperature Distortion," 15th AIAA/SAE/ASME Joint Propulsion Conference, June 18-20, 1979, Las Vegas, Nevada, 79-1310.

Appendix A: Tabulated Distortion Index Data

Table A-1: CFD Distortion Results at the AIP

CFD Run	Flow Variable	Value				
		Max	Min	MW-Ave	(Max-Min)/MW-Ave	% Distortion
Thermal Source	To	314.098	300.162	303.734	0.046	4.588
	Po	94105.843	92739.956	93579.109	0.015	1.460
	Ps	86392.720	86317.914	86325.000	0.001	0.087
	M	0.353	0.321	0.341	0.096	9.553
	V	121.208	112.691	116.204	0.073	7.329
Serpentine Duct - Hot Injection	To	299.478	287.656	289.043	0.041	4.090
	Po	101589.040	92003.961	100289.680	0.096	9.557
	Ps	91016.539	90657.148	90852.789	0.004	0.396
	M	0.402	0.145	0.377	0.682	68.201
	V	134.586	50.088	126.600	0.667	66.745
Serpentine Duct - Cold Injection	To	288.325	287.150	287.963	0.004	0.408
	Po	101610.690	92389.859	100308.040	0.092	9.193
	Ps	91101.547	90748.062	90938.203	0.004	0.389
	M	0.401	0.160	0.376	0.640	63.993
	V	134.161	54.278	125.935	0.634	63.431
CFD Run	Flow Variable	Value				
		max	min	mw-ave	(max-min)/mw-ave	% Distortion
Serpentine Duct - No Injection	To	288.470	286.510	288.000	0.007	0.681
	Po	104882.500	92304.844	100854.900	0.125	12.471
	Ps	91363.992	90300.477	90701.000	0.012	1.173
	M	0.452	0.146	0.386	0.794	79.357
	V	150.883	49.374	129.299	0.785	78.507
Straight Duct - Hot Injection	To	300.981	287.791	289.086	0.046	4.563
	Po	101930.140	94150.609	99895.172	0.078	7.788
	Ps	90744.266	90451.781	90512.945	0.003	0.323
	M	0.416	0.233	0.378	0.486	48.632
	V	141.616	78.690	126.830	0.496	49.615
Straight Duct - Cold Injection	To	288.034	287.673	287.976	0.001	0.125
	Po	102647.160	94128.125	99813.094	0.085	8.535
	Ps	90712.398	90400.539	90459.000	0.003	0.345
	M	0.430	0.234	0.377	0.520	51.958
	V	143.436	78.979	126.426	0.510	50.984

Appendix B: Additional Equations

The following equations are associated with the governing RANS equations (FLUENT, 2005). They are intended to provide additional detail of the energy sources contributing to the solutions to the CFD analyses.

$$(\tau_{ij})_{eff} = \mu_{eff}\left(\frac{\partial u_i}{\partial x_j}+\frac{\partial u_j}{\partial x_i}\right)-\frac{2}{3}\mu_{eff}\,\delta_{ij}\,\frac{\partial u_i}{\partial x_i} \qquad \textbf{B-1}$$

τ_{ij} is the viscous stress tensor. In equation B-1, $(\tau_{ij})_{eff}$ is of the same form of τ_{ij}, but scaled by the effective viscosity, μ_{eff}, rather than merely the dynamic viscosity, μ. μ_{eff} is a function of the dynamic viscosity and the turbulent viscosity, μ_t, which account for shearing stresses that originate from contact between fluid particles and solids (or, walls) and the viscosity generated from turbulent mixing (respectively).

$$k_{eff} = k+\frac{c_p\mu_t}{\mathrm{Pr}_t} \qquad \textbf{B-2}$$

k_{eff} is the summation of the laminar thermal conductivity and the turbulent conductivity of the fluid (B-2). Hence, the presence of turbulence increases heat transfer.

$$E = h-\frac{p}{\rho}+\frac{u^2}{2} \qquad \textbf{B-3}$$

The total energy, E, accounts for the total enthalpy and kinetic energy in a system (B-3).

$$h = \int_{T_{ref}}^{T} c_p\,dT \qquad \textbf{B-4}$$

Enthalpy, h, is a measure of the internal energy in the system (B-4). Since the working fluid is air, there is only one c_p value. In combustion problems, the calculation is more involved since combustion products and probably dissociated chemicals are present.

$$G_K = -\rho\overline{u_i' u_j'}\frac{\partial u_j}{\partial x_i} \qquad \textbf{B-5}$$

G_K, as seen in equation B-5, is present in the $K-\varepsilon$ turbulence model equations. It evaluates the flows potential to produce turbulence.

$$G_b = \beta g_i \frac{\mu_t}{\mathrm{Pr}_t}\frac{\partial T}{\partial x_i} \qquad \textbf{B-6}$$

G_b adds turbulence to the flow based on the effects of buoyancy (B-6). In our analysis, no gravity (g_i) is accounted for. Therefore, $G_b = 0$.

$$Y_M = 2\rho\varepsilon M_t^2 \qquad \textbf{B-7}$$

Y_M is included in the $K-\varepsilon$ turbulence model to include compressibility effects (B-7). This equation is a function of the flow density, turbulence dissipation, and the turbulent Mach number, defined below (B-8).

$$M_t = \sqrt{\frac{K}{\gamma RT}} \qquad \textbf{B-8}$$

Appendix C: FLUENT UDF

```
/************************************************/
/* mod_source.c                                 */
/* modified from www.fluent.com                 */
/* The author does not take credit for the modification */
/* of this code.                                */
/*                                              */
/* Info: defines the volumetric heating in the system */
/************************************************/

#include "udf.h"

DEFINE_SOURCE (mod_source, c, t, dS, eqn)
{
  real x[ND_ND], y, z, theta, source;
  begin_c_loop(c,t)
  {
    source = 8500000;
    dS[eqn] = 0;
  }
  end_c_loop (c,t)
  return source;
}
```

Vita

Kevin Michael Eisemann was born in Takoma Park, MD on July 13, 1981, to William and Christine Eisemann. He is the younger sibling of a hell-raising, yet loving brother, Brian. Kevin resided in Silver Spring, MD with his family until graduating high school in the spring of 1999. He enrolled into the engineering program at Virginia Tech, and eventually became interested in mechanical engineering. Kevin graduated from Virginia Tech in the spring of 2003 with his Bachelor's of Science in mechanical engineering. He immediately pursued graduate school at Virginia Tech and was privileged to work under his advisor, Dr. Walter O'Brien. As a graduate student, Kevin focused on learning material related to gas turbine engines. His research, which investigated the boundary conditions entering a gas turbine compression system with inlet thermal distortion, is presented in this thesis. Kevin successfully defended his thesis on June 16, 2005. Following this momentous day, Kevin celebrated by vacationing in Europe with his buddy Nate and taking a road trip across the US his good friend Suellen.

During his collegiate career, Kevin participated in numerous internships. He worked in the Washington, D.C. area as an engineering intern at the Army Research Laboratory (ARL) in summer of 2000 and an engineering intern at the Naval Research Laboratory (NRL) in the summers of 2001 and 2002. Kevin was awarded the University Turbine Systems Research (UTSR) Industrial Fellowship from the South Carolina Institute for Energy Studies (SCIES) to work at Pratt & Whitney, East Hartford, CT in the summer of 2003. He also participated in the Student Career Experience Program (SCEP) at Wright-Patterson AFB, OH in the spring and summer of 2005.

Kevin completed his Master of Science in Mechanical Engineering degree in the spring of 2007. Kevin is currently working in Cincinnati, OH with GE – Aviation. He is employed as an Aeromechanical Design Engineer and is enjoying the finer things in life.

Pura Vida